Drone-derived SfM Photogrammetry and Digital Rock Mass Mapping of Rock Slopes

Larissa Elisabeth Darvell

Thesis submitted for the degree of
Master in Geohazards and Geomechanics
60 credits

Department of Geosciences
Faculty of Mathematics and Natural Sciences

UNIVERSITY OF OSLO

Nov 2021

Drone-derived SfM Photogrammetry and Digital Rock Mass Mapping of Rock Slopes

Digital Rock Mass Mapping of Rock Slopes and Taluses - with regards to stability, SMR and rockfall frequency

http://www.duo.uio.no/

Print production: Reprosentralen, University of Oslo

Abstract

Rockfalls occur frequently in Norway and pose a risk to people and infrastructure. To determine suitable mitigation measures that could prevent fatalities and damages, rockfall hazard needs to be assessed based on representative and reliable data. The aim of this thesis was to test if drone-derived SfM photogrammetry and digital mapping are methods that can facilitate, streamline, and improve the determination of relevant parameters for rockfall hazard assessment. The method was applied to five study areas located in different parts of Norway, each containing a natural rock slope susceptible to rockfalls. The objectives of this thesis were to establish a functional survey design for collecting data of sufficient quality, establish an efficient workflow for generating and validating georeferenced 3D models, and evaluate different tools for digital mapping of rock masses.

During fieldwork, datasets of overlapping images were collected with a drone-based consumer-grade camera and ground control point positions were recorded with GNSS receivers. Additional GCPs were extracted from orthophotos and digital elevation models. Photogrammetric processing of the collected datasets and generation of 3D models were performed using Agisoft Metashape. Cloud-to-cloud comparison was used to validate the model quality. The model quality was validated with cloud-to-cloud comparison, using high-resolution LiDAR models as reference. Digital mapping of discontinuities was performed on the validated 3D models, using Maptek PointStudio. Discontinuities were characterized by orientation, spacing, persistence, and roughness. Kinematic analyses were performed on the digitally mapped discontinuities and likely failure modes were determined. The established survey design and workflows were found to be functional, efficient, and capable of generating reliable data that accurately represents the study areas.

Acknowledgments

To work on this thesis has been quite the journey! While there has been both frustration and confusion, the work has above all challenged and inspired me.

I would like to thank my supervisors Vidar Kveldsvik, Anders Solheim, Ulrik Domaas and Mark Mulrooney for their support and invaluable feedback during my work with the thesis. Helge Christian Smebye at NGI provided guidance during the first RPAS survey and assistance during the data processing. Trond Eiken at the University of Oslo provided technical field support and performed post-processing of the raw GNSS-data.

I am grateful for the technical assistance provided by Jesper Darvell and the feedback on academic writing given by Heidi Darvell.

Håkan Staffansson, thank you for your unwavering love and support.

Glossary

C2C – Cloud-to-Cloud (comparison), name of function in CloudCompare software

DEM – Digital Elevation Model

DGNSS – Differential GNSS

Focal length – Distance between the optical center of a cameras lens and the sensor/film.

FS – Factor of Safety

GCP – Ground Control Point

GIS – Geographical Information System

GNSS – Global Navigation Satellite System

GSD – Ground Sample Distance

LiDAR – Light Detection And Ranging

m.a.s.l. – metres above sea level

PDOP – Position Dilution Of Precision

RMSE – Root Mean Square Error

RPA – Remotely Piloted Aircraft

RPAS – Remotely Piloted Aircraft System (including both the aircraft and the remote pilot station)

RTK – Real Time Kinematic

SfM – Structure from Motion

Contents

1 Introduction 1
  1.1 Background 1
  1.2 Motivation 2
  1.3 Aim and Objectives 3
2 Theoretical Framework 5
  2.1 Photogrammetry 5
    2.1.1 Photogrammetric Basics 5
    2.1.2 SfM Photogrammetry 7
    2.1.3 SfM in Rockfall Hazard Assessment 10
  2.2 Rock Slope Failure 12
    2.2.1 Classifications and Characteristics 12
    2.2.2 Triggering Factors 14
    2.2.3 Conditioning Factors 16
    2.2.4 Failure Modes 17
    2.2.5 Shear Strength 21
3 Study Areas 23
  3.1 Tunhovdfjorden 23
  3.2 Nomelandsfjellet 24
  3.3 Lærdal 25
  3.4 Straumvatnet 26
4 Methods 28
  4.1 Data Collection 28
    4.1.1 Fieldwork 28
    4.1.2 Ground Control Points 28
    4.1.3 GNSS Measurements 29
    4.1.4 RPAS Photo Collection 31
    4.1.5 GCPs from LiDAR DEMs 34
  4.2 Data Processing 34
    4.2.1 GCP Coordinates 35
    4.2.2 Photogrammetric Processing 35
  4.3 Model Validation 41

4.3.1 Georeferencing Accuracy 41
4.3.2 Systematic Errors 42
4.4 Analysis 43
4.4.1 Extraction of Discontinuities 43
4.4.2 Kinematic Analysis 45
4.4.3 Discontinuity Characterization 46
5 Results 50
5.1 Field Surveys 50
5.2 Photogrammetric Reconstructions 52
5.3 Digital Mapping of Discontinuities 57
5.3.1 Tunhovd 57
5.3.2 Valle 61
5.3.3 Lærdal 64
5.3.4 Ørnlia 67
5.3.5 Straumklumpen 70
5.4 Kinematic Analysis and Failure Modes 73
5.4.1 Tunhovd 73
5.4.2 Valle 78
5.4.3 Lærdal 83
5.4.4 Ørnlia 88
5.4.5 Straumklumpen 92
6 Discussion 96
6.1 Survey Design 96
6.2 Agisoft Metashape Workflow 99
6.3 Quality of Photogrammetric Reconstructions 102
6.4 Analysis Results 106
6.5 Applications in Rockfall Hazard Assessment 110
6.6 Limitations of the Study 112
7 Conclusions 114
References 116
Appendices 124

No table of figures entries found.

1 Introduction

1.1 Background

Landslides occur in all parts of the world and involves the movement of rock or soil down a slope. This thesis concerns rockfalls, which is a landslide type where rock blocks detach from a steep rock slope and moves rapidly downslope driven by gravity (Highland & Bobrowsky, 2008; Hungr et al., 2014). The dramatic Norwegian landscape contains an abundance of steep mountain sides and rock faces that were sculpted by the ice age glaciers. These rock slopes represent potential source areas for rockfalls, and a search in the Norwegian national landslide database reveals that out of 78 000 registered landslides 31 % were registered as rockfalls (NVE, 2021). While the database is incomplete and biased towards events that affected people or infrastructure, it still illustrates that landslides occur frequently and that rockfalls constitutes one of the most common landslide types in Norway.

Rockfalls become a hazard when people build their homes, or the society places infrastructure in the vicinity of rock slopes. Because rockfalls moves very fast and gains high energy, the consequences can be severe. During the 2000th century rockfalls were responsible for 63 fatalities in Norway (Høst, 2006), and every year rockfall damages result in substantial economic losses for individuals and the society. Since 1980, the government founded Norwegian Natural Perils Pool has paid 2.1 billion NOK in compensation for 13 855 landslide damage claims, and these statistics only include events that were not covered by private insurances (Finans Norge, 2021). The risks can be reduced by implementing mitigation measures, such as protective structures, anchoring or land use planning. But in order to apply suitable actions, the hazard first needs to be identified and quantified.

Rockfalls are often controlled by structural weaknesses within the bedrock. An important part of assessing the stability of a rock slope is therefore to accurately characterize the joint sets that are present and the blocks that could be formed by them. The traditional methods of obtaining this information have been to perform measurements in the field directly on rock outcrops, sometimes in combination with drill core sampling (Wyllie & Mah, 2004). In the last decades other methods for data collection have emerged, including laser scanning and photogrammetry. Both methods are used to generate digital 3D models of the surveyed area (Jaboyedoff et al., 2012; Westoby et al., 2012).

Laser scanning techniques and applications are well established today. In contrast, the rapid technological developments of new photogrammetry techniques and its applications within rockfall hazard assessment is still an active and expanding research area (Abellan et al., 2016; Andersson et al., 2019). This thesis seeks to apply the Structure-from-Motion (SfM) photogrammetry technique, which is described as a low-cost, user-friendly, and flexible method for producing high resolution topographic data (Smith et al., 2016; Westoby et al., 2012). But it is not only the data collection methods that have evolved. The extraction of information from generated 3D models through digital mapping is constantly improving (Greenwood, 2018; Menegoni et al., 2019; Vasuki et al., 2014).

1.2 Motivation

The extent of observed fatalities and damages caused by rockfalls suggests that some parts of the risk reduction process need to be improved. The whole process chain that leads up to the anchoring of an unstable block or the installation of a rockfall fence, it all starts with identifying and characterizing the hazard. It is crucial to collect representative, accurate and precise datasets as basis for deciding where to apply mitigation measures and what type of action that is most effective. An issue with traditional methods of collecting data is that it can be challenging or even impossible to gain physical access to the rock slope, which results in limited sampling and high uncertainty. The use of remote sensing tools enables both safe data collection in steep terrain and better sampling.

However, data collection with laser scanning is quite expensive. Aerial laser scanning is typically done from airplanes or helicopters covering larger areas. Such datasets are commonly of moderate resolution and steep areas often contain shadowed areas with no data. Terrestrial laser scanning produces high resolution data, but the usability is restricted by the need for suitable places to mount the scanner, which is not always found. In contrast, drone derived SfM photogrammetry presents as a low-cost, flexible, and more user-friendly method of collecting data. James et al. (2017) pointed out that there is little consistency in how researchers report their applied SfM workflows and uncertainty estimates. This is information that is critical both for reproducibility and for evaluating the quality of the results.

There have been few studies that apply digital rock mass mapping on 3D models generated by SfM photogrammetry. With the new advancements in digital mapping technologies, there is need for more studies that test the applications and explore different settings to find effective workflows.

1.3 Aim and Objectives

Rockfalls pose a threat to people and infrastructure, especially in a country with such high relief topography as Norway. In order to determine suitable mitigation measures that could prevent fatalities and damages, the rockfall hazard needs to be assessed based on representative and reliable data. The aim of this thesis is to test if drone-derived SfM photogrammetry and digital mapping are methods that can facilitate, streamline, and improve the determination of relevant parameters for rockfall hazard assessment. This will be done by applying the mentioned methods to a selection of five study areas located in Norway. Each study area contains a natural rock slope that has experienced recent rockfall activity and is susceptible to future rockfall events.

The objectives are:

1. Establish a functional survey design for collecting datasets of sufficient coverage and quality to serve as a basis for photogrammetric reconstructions and subsequent digital mapping, by using relatively simple and cost-effective tools, such as drone-based consumer-grade cameras and GNSS receivers.

2. Establish an efficient workflow for generating and validating georeferenced 3D models of sufficient quality to serve as a basis for digital mapping.

3. Evaluate different tools, settings, and applications for digital mapping of rock masses, to extract reliable and representative data that could serve as a basis for rockfall hazard assessments.

2 Theoretical Framework

2.1 Photogrammetry

2.1.1 Photogrammetric Basics

Photogrammetry is the science and technology of obtaining reliable geometric information about real-world objects and scenes from images (ISPRS, 2021; Marzolff et al., 2019; Kraus, 2007). Imagery can be collected from either ground-based, airborne or spaceborne platforms equipped with camera or electronic scanner (Marzolff et al., 2019). The geometric information that can be extracted includes point coordinates, distances, heights, orientations, areas, volumes, and 3D topography (Marzolff et al., 2019; Kraus, 2007). While photogrammetry is used in many different areas, one of the main applications is in the production of topographical maps. The maps are used for a large variety of purposes, e.g. surveying of movement and deformation processes, precision measurement in engineering, documentation of buildings, and forensic reconstructions (Kraus, 2007).

Photogrammetry is based on central projection, in which points in a scene are projected as rays of light through a point of convergence (projection centre) and onto an image plane (figure 2.1). Every image is made of a bundle of rays recorded at the same time, and the fundamental task in photogrammetry is to reconstruct their paths (Luhmann et al., 2019; Marzolff et al., 2019). The parameters of interior and exterior camera orientations are necessary for calculating the ray paths, both within and outside the camera. Interior orientation parameters define the focal length, the image principal point, and the lens distortion. The principle point is the intersection between the optical axis and the image plane. Focal length is the distance between the principle point and the projection centre. Exterior orientation parameters define the position and orientation of the camera (Marzolff et al., 2019). Position is given in horizontal and vertical coordinates, while orientation is given as three rotation angles (Luhmann et al., 2019).

At least two overlapping images, called stereopair, is required to produce a 3D representation of the scene. The intersection of corresponding rays from overlapping images allow the 3D position of each point to be calculated (Linder, 2016). Usually an entire block of overlapping images is collected and processed to produce a 3D point cloud (Marzolff et al., 2019). Georeferencing is achieved either by recording the camera position and orientation during image capture (direct georeferencing), or by including recordings of ground control points (GCPs) during processing (Westoby et al., 2012). Orientation is measured with an Inertial Measurement Unit (IMU) and position is measured with a Global Navigation Satellite System (GNSS), or alternatively using a total station for GCPs (Smith et al., 2016).

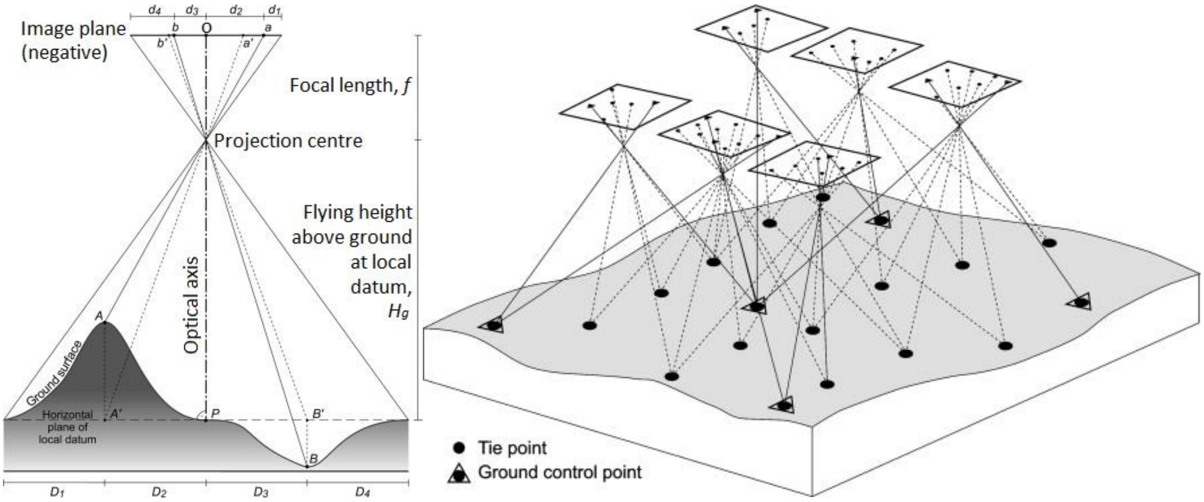

Figure 2.1 The figure to the left illustrates the ray paths between the ground surface (scene) and the image plane within a camera. The image principal point is marked with O. The figure to the right illustrates a block of overlapping images and the ray bundles connecting them to points on the ground surface. Points visible in several images are called tie points. The set of ground control points (GCPs) is used to georeference the 3D network of tie points. Figures are modified from Marzolff et al. (2019).

Photogrammetry as a phenomenon is over 150 years old and its development has been closely linked to that of photography and aviation. Originally analogue cameras were used, which record light on film photochemically. But due to technical advances, digital cameras using electrical sensors has become the standard during the last few decades (Kraus, 2004; Linder, 2016). The type of cameras used in traditional photogrammetry, called metric cameras, are considered to have known and constant interior orientation, thus reducing the need for camera calibration (Luhmann et al., 2019). In contrast, consumer grade cameras require calibration to minimize image distortions and to improve accuracy of the results. During calibration a best-fit mathematical model describing the camera geometry is applied (Linder, 2016).

2.1.2 SfM Photogrammetry

During the last two decades, Structure-from-Motion (SfM) has revolutionized photogrammetry with its flexible and low-cost approach for reconstructing complex topography (Anderson et al., 2019; Westoby et al., 2012). The technique combines photogrammetric principles with computer vision algorithms for feature detection and matching (Anderson et al., 2019; Smith et al., 2016). In contrast to traditional photogrammetry, SfM enables point cloud generation without prior knowledge of camera orientations or use of ground control points. This is achieved by applying bundle adjustment algorithms to solve camera parameters and surface point positions, simultaneously for multiple overlapping images. The result is a network that can be georeferenced by adding camera positions or GCPs. Multi-View Stereo (MVS) algorithms are then commonly used to increase model resolution by extensive point extraction (Smith et al., 2016; Westoby et al., 2012).

The SfM approach has made it possible to produce high resolution topographic data using images collected with consumer-grade cameras mounted on inexpensive, lightweight platforms, such as Remotely Piloted Aircraft Systems (RPAS) or drones (Westoby et al., 2012). SfM is able to reconstruct topography from irregular image configurations containing oblique and convergent imagery, thereby lowering the demands on survey design and implementation. The generation of topographic models is further facilitated by user-friendly software with largely automated processing. These factors effectively reduce the need for technical expertise and expensive surveying equipment, making photogrammetry accessible for a wide group of users, from geoscience professionals to amateur photographers (Luhmann et al., 2019; Smith et al., 2016; Westoby et al., 2012). However, due understanding and consideration of photogrammetric principles, error sources, and editing actions are essential for providing confidence in the results (James et al., 2017; Marzolff et al., 2019).

General Workflow

The general workflow applied by SfM software packages for reconstructing topography from a set of overlapping images as described by Smith et al. (2016) is outlined below:

1. **Feature detection.** Every image is searched for distinguishable features (key points). For every identified key point, a unique descriptor is generated and stored in a feature database. The descriptor is independent of variations in scale, viewing angle, and illumination. The described process is implemented by using SIFT or similar algorithms.

2. **Key point matching.** The descriptors are used to match key points across images. Matching points are called tie points.

3. **Key point filtering.** Erroneous tie points are identified and removed, using RANSAC or similar methods to test for outliers.

4. **SfM.** Bundle adjustment algorithms provides simultaneous estimation of tie point positions, interior and exterior camera orientations. The image metadata stored in the EXIF tag is used during initial camera calibration, and solutions are optimized through minimization of a cost function reflecting the measurement error. The output is camera parameter values and an unscaled sparse point cloud. If no camera positions are recorded in the EXIF, the combined network of images and tie points will be placed in a local coordinate system.

5. **Scaling and georeferencing.** Georeferenced in a global coordinate system can be achieved either by adding camera position coordinates or by identifying GCPs in individual images and adding their coordinates. The network is then scaled, translated, and rotated accordingly. A common approach is to use direct georeferencing with a low accuracy GNSS to get approximate camera positions as a starting point for bundle adjustment. Then adding GCPs to further improve the network accuracy.

6. **Refinement of parameter values.** Repeated bundle adjustments are performed for further optimization of the model. Both image observations and added georeferencing

information is considered. The influence of each measurement is determined by its accuracy estimate.

7. **MVS.** This step generates a dense point cloud. Using the estimated parameter values from the previous step as input, MVS algorithms can extract high concentrations of points from images.

Uncertainties and Error Sources

Accuracy is a measure of the difference between ‘true’ and estimated values, while precision is a measure of variability within a dataset (JCGM, 2012). Reconstructed SfM models should be validated against independent data representing the ‘true’ topography. Reference data can be derived from total station, GNSS, ground-based or airborne LiDAR (i.e. laser scanning). Accuracy of SfM data is commonly reported as Root Mean Square Error (RMSE), Mean Error (ME) or Mean Absolute Error (MAE), while standard deviation of error is used to describe precision. The level of georeferencing accuracy and precision possible to achieve in SfM surveys, is mainly controlled by survey range (i.e. target-camera distance). A shorter survey range allow higher model quality to be obtained. The relationship is linear, with an observed ratio of 1:639 between RMSE and range (Smith et al., 2016), and a ratio of 1:1000 between standard deviation and range (James & Robson, 2012). This indicates that a survey range of 50 m has the potential of obtaining 8 cm accuracy and 5 cm precision.

Many factors influence the actual obtained model accuracy and may cause lower over-all quality than the empirically derived ratios would dictate. Due to the complexity of the SfM method, it is incredibly challenging to quantify individual error sources. The main factors influencing the final model quality are how well GCPs are distributed within the survey area and their positioning accuracy (Smith et al., 2016). It is also important to adapt a processing workflow and settings that fit each specific project, in particular with regards to the relative weighting of GCPs and tie points within the bundle adjustment (James et al., 2017).

Systematically distributed error is often present to some degree in SfM data. These originate from image network geometry and incorrect camera calibration (James & Robson, 2014). Vertical, near-parallel images captured with a consumer-grade camera introduces radial distortions, causing a ‘dooming’ effect in the model. The radial distortions are difficult to remove with the camera self-calibration in SfM software but are mitigated by implementing a survey design containing oblique, convergent imagery and well-distributed GCPs (James & Robson, 2014; Smith et al., 2016). Image distortions caused by movement blur and a rolling shutter are possible to reduce during processing, if the camera motion was systematic (i.e. an automated flight plan was used) (Luhmann et al., 2019). The presence of remaining systematic error can be explored through model-to-model comparisons using a high accuracy dataset as reference (Smith et al., 2016).

2.1.3 SfM in Rockfall Hazard Assessment

SfM photogrammetry is still a young method, for which the performance, applications, and practices are being continually developed and explored (Abellan et al., 2016; Anderson et al., 2019). The SfM method is being increasingly adopted in geohazard risk management – from the initial hazard identification and subsequent risk analysis, to mitigation measures such as monitoring, and finally as a tool in disaster response (Gomez & Purdie, 2016; Rodriguez et al., 2020). A selection of published work using SfM for different tasks in rockfall hazard assessment is presented below.

Zekkos et al., (2018) provides an overview of geotechnical applications for UAV-enabled SfM and presents a selection of case studies. The methods usefulness as a tool for immediate post-disaster response is highlighted and accredited to fast and safe image collection with UAV in unstable or inaccessible terrain. Menegoni et al. (2020) analysed the performance of SfM models reconstructed from emergency surveys, performed shortly before and after a landslide event occurred. Despite not using GCPs, the predicted failure mechanism and rockfall volume proved to be essentially correct. The study indicates that simplified surveys can produce results with acceptable geometric accuracy for emergency hazard assessment.

Obanawa and Hayakawa (2018) performed repeated UAV surveys of a sea cliff in Japan and used the SfM method to reconstruct the scene at the different moments in time. The volumetric changes were measured, and the erosion rates calculated. Time periods of increased rockfall activity or erosion was compared to potential triggers, allowing identification of the main triggering factor. Rodriquez et al. (2020) performed a case study in Canada, using UAV-derived SfM photogrammetry. They applied a two-method validation in CloudCompare – using both C2C (see section 4.3.1) and M3C2. Multi-temporal point cloud comparisons allowed them to detect surface changes, while a SfM-generated DEM was used as input in both drainage analysis and rockfall trajectory modelling.

Warrick et al. (2017) applied SfM photogrammetry to sets of historical images documenting coastal cliffs. They were able to map the topography and quantify changes related to landslides, rockfalls, and erosion. The number of events was estimated, and their volumes were measured. Guerin et al. (2020) also reconstructed topographic models of rock slopes from historical images, using the SfM method. When comparing these models with models based on recent surveys, many previously unknown rockfalls were identified and measured. In addition, the volume-frequency relationship and mean erosion rate were estimated. The study managed to improve local rockfall inventory databases, and by extension allowing more accurate hazard assessments.

Digital mapping of rock masses with regards to rockfall hazard is a research area being continuously developed. While LiDAR has been used extensively for producing 3D models used in digital mapping, the use of SfM photogrammetry is less explored (Abellan et al., 2016). Both Vasuki et al. (2014) and Greenwood (2018) developed and tested methods for semi-automated digital mapping of discontinuity traces (linear features) in 3D models generated with UAV-derived SfM photogrammetry. Menegoni et al. (2019) compared manual and semi-automated digital mapping of discontinuity surfaces in SfM models. While the semi-automated methods could detect 10-30 times more discontinuities than manual analysis, they also identified planar surfaces which did not represent discontinuities. Menegoni et al.

concluded that semi-automatic detection of features can be performed quickly, but the necessary validation of results takes considerably longer. Another important observation was that automated detection of discontinuities oriented perpendicular to the slope did not perform well.

2.2 Rock Slope Failure

2.2.1 Classifications and Characteristics

Internationally the landslide classification introduced by Varnes (Varnes, 1978; Cruden & Varnes, 1996) and updated by Hungr et al. (2014) is widely used. The system classifies landslides according to type of material and movement. The main material categories are rock and soil, while the movement types consist of fall, topple, slide, spread, flow, and slope deformation. When a landslide event is complex and transitions from one type to another, it may be classified based on the dominant properties of the event (Hungr et al., 2014). This thesis will however focus on the landslide class of rockfalls ("steinsprang"), as described by the Norwegian classification system. Using this definition is deemed appropriate because the thesis is mainly intended for a Norwegian audience and for practical reasons should be compatible with Norwegian terminology.

The Norwegian system for landslide classification is based on material type, volume, and landslide dynamics. Failure in bedrock is divided into three classes; "steinsprang", "steinskred" and "fjellskred" (NVE, 2020). The former two are both commonly translated as rockfalls, regardless if the initial movement is falling, toppling or sliding (Devoli et al., 2011; NVE, 2020). "Steinsprang" consists of relatively small rock volumes up to hundreds or sometimes thousands of m^3 and are characterized by little or no interaction between moving blocks. The blocks move independently and loose energy as a result of interaction with the topography. "Steinskred" have rock volumes of up to 100 000 m^3, and it's common for fragments of the moving mass to interact and shatter (NVE, 2020). If the rock volume exceeds 100 000 m^3, the landslide belongs to the third class "fjellskred" which corresponds to the international term rock avalanche. A rock avalanche is characterized by the fragmented rock mass moving in a flow-like manner and often reaching extreme runout distances (NVE, 2020; Hungr et al., 2014).

Rockfalls occur in slopes containing rock outcrops or bedrock with a thin cover, and where the slope angle exceeds 45 degrees. They can also occur in more gently dipping slopes if there are structural elements present which enables this, e.g. slope-parallel exfoliation (NVE, 2020). One or several rock blocks detach in the source area and travel rapidly downslope by falling, bouncing, rolling, or sliding (NVE, 2020; Hungr et al., 2014). Rockfalls are driven by gravity and the moving blocks gain energy when they are airborne. Conversely, the loss of energy is due to impacts and friction during interactions. This is why high fall heights, steep slope angles and hard slope surfaces are factors that increase kinetic energy and velocity of the rockfall (Wyllie, 2014). If forests are present in the rockfall path, they act as natural barriers which absorbs energy from the rockfall (Volkwein et al., 2011).

When the slope angle becomes lower and/or the slope surface changes to a softer material, the blocks lose enough kinematic energy to deposit (figure 2.2). Slopes with frequent rockfall activity has well-developed taluses where most rockfalls accumulate (Dorren, 2003; Wyllie, 2014). Due to rockfall dispersion, taluses will often develop a cone-shape with a 45-70 degree spreading angle from the talus apex (Wyllie, 2014). The taluses become sorted as smaller fragments are deposited first, mainly because the smaller mass gives the fragments lower total kinetic energy. But smaller fragments are also more easily retarded by obstacles, such as trees or large blocks. A few large blocks may also travel beyond the talus (Dorren, 2003; Wyllie, 2014).

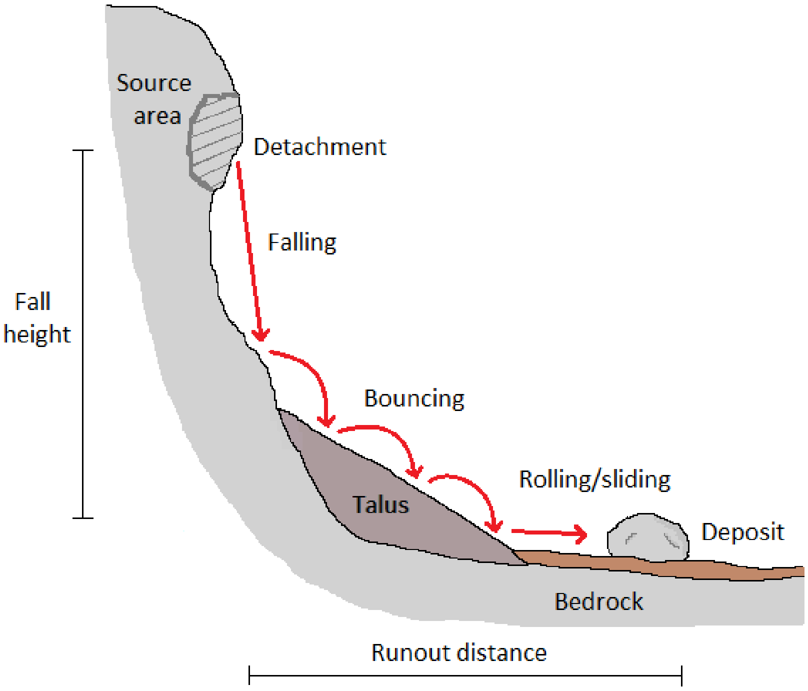

Figure 2.2 Schematic cross-section of a rockfall and associated terminology.

2.2.2 Triggering Factors

Rock masses become unstable and susceptible to rockfalls over time, as a result of several conditioning factors (see section 2.2.3), while the trigger of a rockfall event is the final factor that sets the rock mass in motion (Dorren, 2003; Varnes, 1978). The trigger provides external stimuli to the rock mass, increasing the stress and/or reducing the stabilizing forces, until the rock mass fails (Dietze et al., 2017). Rockfall activity in Norway displays seasonal variations, with an increased frequency of events happening during spring and autumn. The increase is accredited to freeze/thaw cycles, snowmelt during spring and increased precipitation during autumn (Devoli et al., 2011; NVE, 2020).

Both water infiltration and ice growth in cracks can act as triggers by increasing the pressure on blocks to the point where they are displaced and dislodged (Braathen et al., 2004; Wyllie et al., 2014). Ice-filled cracks can also have a stabilizing effect, in bonding the rock masses. The effect is however temporary, and many rockfalls occur during thawing when these ice-bonds melt and previously displaced blocks are released (Wyllie, 2014). Water can act as a trigger in several other ways. Saturation of a permeable rock volume increases its weight and adds to the stresses. Water can dissolve and wash away cohesive minerals in cracks, as well as contribute to weathering that produce lubricating infill. The water itself acts as a lubricator, reducing shear strength of slide surfaces (Braathen et al., 2004; Cruden & Varnes, 1996; Dietze et al., 2017). Expansion of cracks and subsequent rockfall triggering can be caused by swelling clay minerals that has been hydrated by water infiltration (Dietze et al., 2017; Varnes, 1978).

Recent studies show that thermal stresses might be a more important rockfall trigger than previously assumed, at least where exfoliation (see section 2.2.3) structures are present. The outer layer of a rock slope expands and contracts in response to diurnal, seasonal and annual temperature changes. It is the limited depth of the sheet-like blocks associated with exfoliation that exposes them to thermal stresses, because the expansion/contraction only occurs within dm-m distances from the rock surface. (Collins & Stock, 2016; Dietze et al., 2017). Studies performed in the European Alps, Southern New Zealand Alps and Norway indicate a relationship between permafrost degradation and rock slope failures. The mechanisms by which warming of permafrost is thought to trigger rockfalls are loss of ice-bonds in fractures, reduced shear strength, and increased hydrostatic pressure due to meltwater (Allen et al., 2009; Fischer et al., 2012; Hilger, 2019; Ravanel et al., 2017). Approximately 20 % of steep slope surfaces in mainland Norway are affected by sporadic permafrost and could potentially experience rockfalls triggered by permafrost degradation (Magnin et al., 2019).

The ground shaking generated by earthquakes, volcanic activity, and large landslides results in inertial forces that can trigger rockfalls. Several human activities also produce ground vibrations capable of releasing rockfalls, including blasting and construction work (Dietze et al., 2017). Erosion at the toe of a slope can cause it to become oversteepened and trigger rockfalls. The same effect can be observed when regulating the water level of reservoirs, and during excavations of road cuts or quarries (Highland & Bobrowsky, 2008; Cruden & Varnes, 1996). In addition to the above-mentioned triggers, both animals and vegetation can cause rockfalls. Tree roots can penetrate deep into cracks, both expanding and extending them.

Combined with wind the trees may also exert a leverage effect on the rock masses (Dietze et al., 2017; Wyllie, 2014).

2.2.3 Conditioning Factors

Many of the processes and phenomena presented as triggers in section 2.2.2 can also act solely as conditioning factors, promoting failure without initiating movement (Dorren, 2003). However, the most important factors controlling rockfalls are geology and topography (Devoli et al., 2011). Structural features play a crucial role in the stability of rock slopes. As intact rock often is strong and must be exposed to large stresses for fractures to be developed, rock slope failure tends to happen along weak, pre-existing discontinuity surfaces (Stead & Wolter, 2015; Wyllie & Mah, 2004).

A discontinuity is defined as a break in the rock and examples include joints, faults, bedding planes, and foliation (Wyllie & Mah, 2004). Discontinuities generated in the same manner or by the same event, will often appear in sets of parallel surfaces. A system of discontinuity sets can form potentially unstable blocks of rock. The size and shape of the blocks are controlled by discontinuity persistence (i.e. length), spacing, and number of sets (Wyllie & Mah, 2004).

The lithology of a rock mass determines how it responds to weathering and applied stresses that may cause fracturing and opening of joints (Dorren, 2003; Wyllie, 2014). In sedimentary rock, fractures preferentially develop along the bedding planes that formed during sediment deposition (Stead & Wolter, 2015; Wyllie & Mah, 2004). Similarly, fracturing often occurs along foliation or cleavage in metamorphic rock. Tectonically induced damage can affect all rock types, producing discontinuities and weakening the rock mass (Stead & Wolter, 2015). The stress release in rock slopes following glacial unloading can result in slope-parallel sheetlike fracturing, called exfoliation (Braathen et al., 2004). In addition, glacial erosion affects slope stability by changing the topography and steepening rock slopes (Stead et al., 2021).

The topography changes as landscapes evolve with time due to tectonic and seismic processes, groundwater cycles, weathering, erosion, and mass wasting (Stead et al., 2021). The significance of topography is that steep slopes are needed for rockfall initiation (section 2.2.1). Furthermore, the intersection between a slope surface and discontinuities in the rock mass determines the failure mode (section 2.2.4) and affects rockfall susceptibility (Stead & Wolter, 2015).

2.2.4 Failure Modes

The basic modes of failure in rock slopes are planar, wedge, toppling, and circular failure (Hoek & Bray, 1981). The former three are structurally controlled, while circular failure occurs in either very weak rock or heavily fractured rock containing randomly oriented discontinuities (Wyllie & Mah, 2004). A simplified illustration of these failure modes is presented in figure 2.3. Since this thesis focuses on the failure of relatively intact rock blocks, the circular failure mode will not be presented or discussed in greater detail.

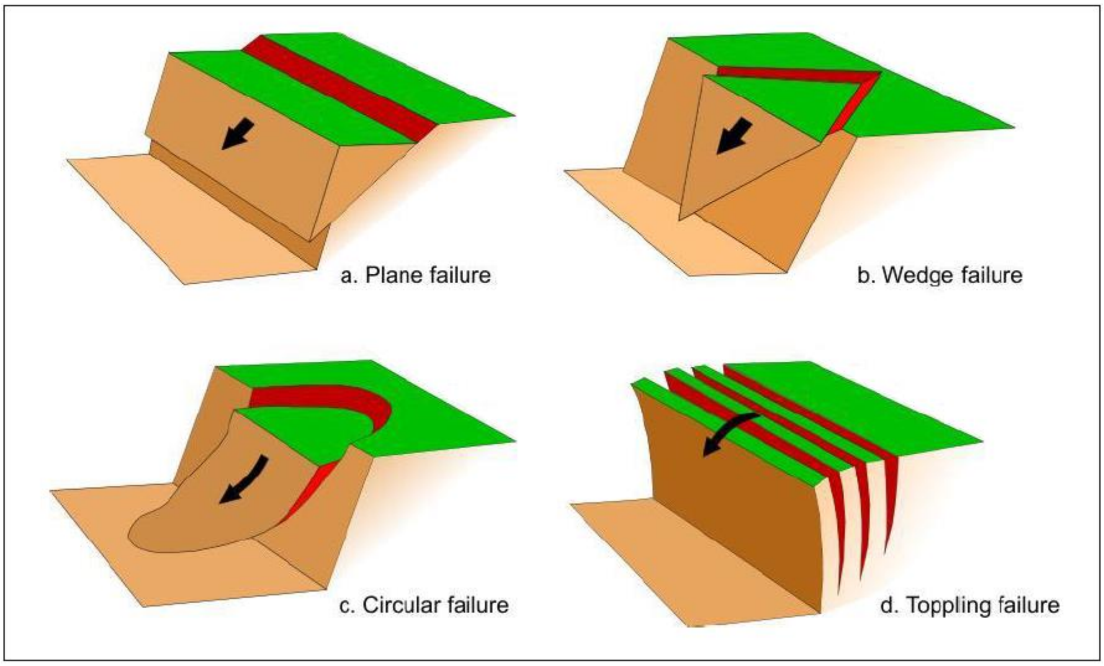

Figure 2.3 Illustration of basic rock slope failure modes (Hoek, 2009). The toppling mechanism that is shown in D is the type flexural toppling, which have no joint set defining a basal detachment surface.

Kinematic Analysis

A common method for identifying discontinuity sets and possible failure modes in rock slopes is to perform a kinematic analysis using stereographic projection. The stereonet is a 2D representation of a reference sphere, which defines all possible dip and strike angles. Structural data, such as discontinuity planes and traces, are projected onto the stereonet based on their measured orientations. A plane can be plotted as a great circle (line) or, as is more common when dealing with large amounts of data, a pole (point). Areas with higher concentrations of discontinuities within the stereonet are interpreted as discontinuity sets (Wyllie & Mah, 2004).

A critical zone can then be defined for each of the structurally controlled failure modes, based on the rock slope orientation, the assumed friction angle of the discontinuity surfaces and lateral limits specifying the angular range of strike/dip direction. Discontinuities or discontinuity intersections that plot within the respective critical zones indicate the potential for planar, wedge, or toppling failures. The kinematic analysis is useful for preliminary stability assessment. The method is however limited in the sense that it does not incorporate discontinuity persistence and spacing, nor consider the effects of water pressure along discontinuities (Stead et al., 2021; Wyllie & Mah, 2004).

Planar Failure

The planar failure mode (figure 2.3a) releases a block that slides along a single basal plane, dipping out of the face. The general conditions at which planar failure occurs are as follows (Hoek & Bray, 1981; Stead et al., 2021; Wyllie & Mah, 2004):

- The basal sliding plane must strike roughly parallel to the slope, within ± 20º.
- The basal sliding plane must daylight (i.e.) on the slope surface.
- The dip of the basal sliding plane must be smaller than the dip of the slope.

- The dip of the basal sliding plane must be larger than the friction angle of the plane’s surface.
- The rear release of the block can be formed by a continuation of the basal sliding plane into the upper slope or by another discontinuity intersecting the basal sliding plane, such as a tension crack.
- The lateral release of the block must not provide resistance to sliding.

Wedge Failure

The wedge failure mode (figure 2.3b) involves the release of a wedge-shaped block that has a base consisting of two persistent discontinuities which strike obliquely to the slope surface. The intersection of these two discontinuities forms a line that is dipping out of the slope (Wyllie & Mah, 2004). Depending on the orientations of the involved discontinuities, sliding can occur along both discontinuity planes in the direction of the intersection line, or on only one of the planes (Stead et al., 2021). Wedge failures can form over a considerably wider range of geological and geometric conditions compared to planar failures. The general conditions required for wedge failures are as follows (Wyllie & Mah, 2004):

- The two discontinuity planes that forms the wedge should intersect in a line.
- The intersection line must daylight on the slope surface and dip out of it.
- The plunge of the intersection line must be smaller than the dip of the slope.
- The plunge of the intersection line must be larger than the average friction angle of the sliding planes.

Toppling Failure

The toppling failure mode (figure 2.4) is characterized by an outwards rotation of rock blocks. The toppling occurs because the blocks are positioned so that their center of gravity falls outside the base of the block (Wyllie & Mah, 2004). Several types of toppling mechanisms have been described (Goodman & Bray, 1976; Hoek & Bray., 1981), but in kinematic analysis it is common to only distinguish between the two primary modes of block and flexural toppling (Wyllie & Mah, 2004). Block toppling can also be referred to as “direct toppling” (Hudson & Harrison, 2000).

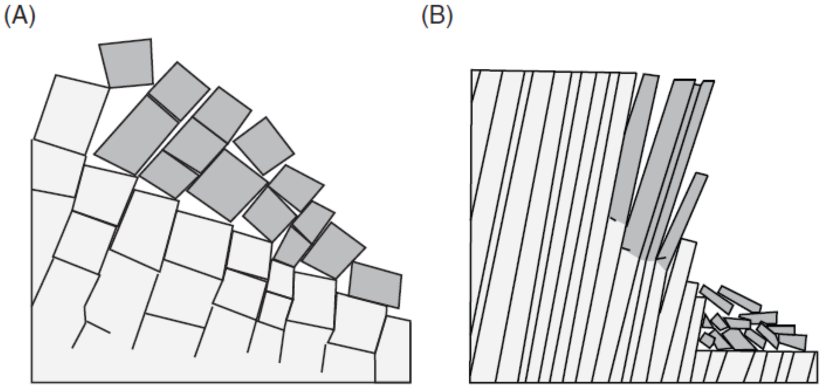

Figure 2.4 Illustration of the two primary toppling modes; A) block toppling and B) flexural toppling. The figure is modified from Stead et al. (2021).

All types of toppling are formed by discontinuity planes dipping steeply into the slope face. In the case of block toppling there is also a discontinuity set present that is orthogonal to the steeply dipping discontinuities and which forms the base of the failing blocks (figure 2.4a). Flexural toppling, on the other hand, occurs on continuous rock columns that break into blocks through tensile fracturing induced by forward rotation and bending of the columns (figure 2.4b). During flexural failure interlayer slip takes place along the steeply dipping and closely spaced discontinuities that separates the rock columns (Stead et al., 2021; Wyllie & Mah, 2004). Flexural toppling is most common in weak rock masses (Stead et al., 2021).

The general conditions required for block toppling are as follows (Hudson & Harrison, 2000):

- Two steep discontinuity sets acts as lateral and rear release planes, and their intersection dips into the slope.
- A third discontinuity set acts as basal release planes.
- The center of gravity must lie outside the base of the block. This criterion is satisfied when the block width and height ratio is smaller than the tangent of the basal plane dip, i.e. $w/h < \tan \Psi_B$.
- If the dip of the basal plane is less than the friction angle (i.e. $\Psi_B < \Phi_B$), failure occurs through toppling only. If the dip of the basal plane is greater than the friction angle (i.e. $\Psi_B > \Phi_B$), failure is a combination of sliding and toppling.

- The dip direction of the basal plane and the trend of the intersection line for the block faces must be within ± 20º of the slope dip direction. The exception is very steep slopes, for which oblique toppling is possible at a larger range of orientations.
- The angle between the slope face and the basal plane must be less than or equal to 90°.

The general conditions required for flexural toppling are as follows (Goodman, 1989; Hudson & Harrison, 2000):

- The rock columns are defined by of one discontinuity set, dipping steeply into the slope.

- Interlayer slip must be possible along the discontinuity planes. The discontinuity dip angles (Ψ_J) at which interlayer slip can occur depend on the friction angle of the discontinuity planes (Φ_J) and the slope dip (Ψ_S). The relationship is defined by the following equation: $\Psi_J \geq \Phi_J + (90 - \Psi_S)$.

- The discontinuity planes must strike roughly parallel to the slope, within ± 20-30º.

2.2.5 Shear Strength

Rockfalls are released when the driving forces exceed the shear strength of a rock volume. Because discontinuities constitute the weakest parts of a rock volume, stability assessments tend to focus on discontinuity strength rather than intact rock strength (unless the rock is very weak or heavily fractured). Several shear strength criteria exist, including the Mohr-Coulomb criterion, the Barton-Bandis criterion, and the generalized Hoek-Brown criterion. The shear strength of a discontinuity is determined by the friction and cohesion along its surface. Infill material may provide cohesion between two rock walls, whereas the shear strength for a clean discontinuity is defined only by its friction (Wyllie & Mah, 2004).

The Barton-Bandis criterion for a cohesionless discontinuity is outlined below (Barton & Choubey, 1977):

$$\tau = \sigma' tan\left(\varphi + JRC\ log_{10}\left(\frac{JCS}{\sigma'}\right)\right) \qquad \text{Eq. 1}$$

Where:

τ = shear stress

σ' = effective normal stress

φ = friction angle

JRC = Joint Roughness Coefficient

JCS = Joint Compressive Strength

The shear strength of a discontinuity is a function of the effective normal stress acting on its surface. Water pressure reduces the effective normal stress, and water infiltration in discontinuities therefore has a negative influence on shear strength (Stead et al., 2021; Wyllie & Mah, 2004). Friction is expressed as a friction angle, and it is generally higher in coarse-grained rock than in fine-grained rock (Wyllie & Mah, 2004). Large-scale undulations of the discontinuity surface and small-scale asperities on the rock walls causes interlocking (Stead & Wolter, 2015; Wyllie & Mah, 2004). The effect of the surface irregularities is expressed as a roughness component and added to the friction angle of the rock material. High normal stresses acting on a discontinuity surface can cause shear displacement and asperities to break off, thus reducing the friction angle (Wyllie and Mah, 2004). Discontinuity persistence is another important factor to consider because the presence of rock bridges between discontinuities can significantly increase the strength of a rock volume (Stead & Wolter, 2015).

3 Study Areas

Five study areas were chosen for photogrammetric modelling and subsequent digital mapping. The areas were chosen based on the criteria that they should each contain a natural rock slope, evidence of recent rockfall activity, and be sparsely vegetated. In addition, the specific requirements for operating the RPA (Remotely Piloted Aircraft) that would be used in data collection needed to be met (section 4.1.4). The study areas are located in different parts of Norway and have different characteristics.

3.1 Tunhovdfjorden

This study area is located along the eastern shores of Tunhovdfjorden, close to southern end of the lake, in Viken county (figure 3.1). It is situated just above the road Tunhovdvegen, at 760-890 m.a.s.l. (metres above sea level), and covers a distance of 360 m parallel to the road. The study area consists of a steep rock slope and a well-developed talus. The rock slope is S-SW facing and approximately 100 m high. Most of the rock slope has an angle of 80º and are therefore potential rockfall source areas. The talus appears mostly unvegetated, which indicates recent rockfall activity. The rock consists of quartzite (NGU, 2021).

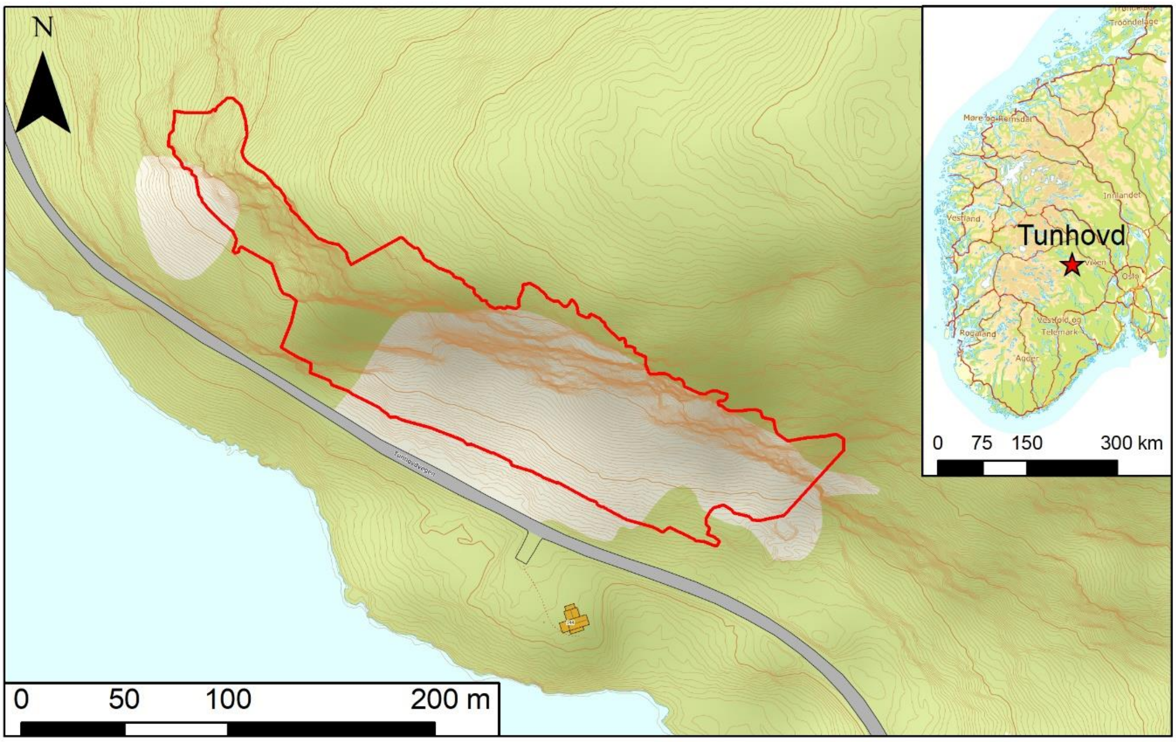

Figure 3.1 Location of the study area next to the Tunhovdveien road and the Tunhovdfjorden lake, where the red polygon defines the area that was surveyed and modelled. The inset map shows the study area location on an overview map over southern Norway (Kartverket, 2021).

3.2 Nomelandsfjellet

This study area is located next to the small town Valle, in the Setesdalen valley of Agder county (figure 3.2). It is situated along the mountainside of Nomelandsfjellet, at 315-665 m.a.s.l. and covers a distance of 530 m parallel to the valley. The study area consists of a gently dipping rock slope and an under-developed talus. The rock slope is SE facing and approximately 300 m high. The slope curvature is concave in the dip direction and convex parallel to the valley. Large areas of the rock slope have angles of 50° and are therefore potential rockfall source areas. The talus appears small and largely vegetated which indicates infrequent rockfall activity. The rock consists of granite (NGI, 2017).

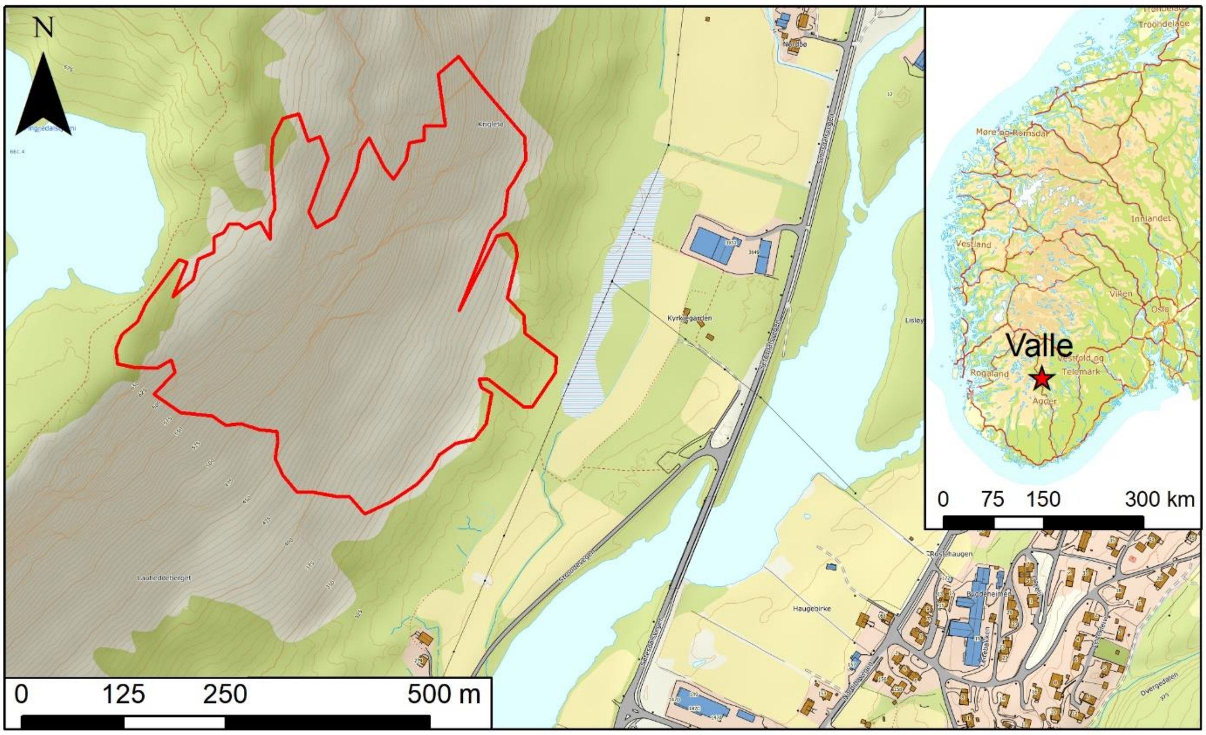

Figure 3.2 Location of the study area on the Nomelandsfjellet mountainside in Valle, Setesdal. The red polygon defines the area that was surveyed and modelled. The inset map shows the study area location on an overview map over southern Norway (Kartverket, 2021).

3.3 Lærdal

This study area is located along the southern mountainside of the narrow Lærdal valley, in Vestland county (figure 3.3). It is situated at 55-360 m.a.s.l. next to a farm called Ytstabø, and measures 420 m in length. The study area consists of a steep rock slope and a pronounced talus cone. The rock slope is N-NE facing and the surveyed slope section is approximately 200 m high. The slope curvature is concave both in the dip direction and parallel to the valley. Most of the rock slope have angles of 85° and are therefore potential rockfall source areas. The talus appears largely unvegetated which indicates recent rockfall activity. The rock consists of granite, which might locally be metamorphosed to augen gneiss (NGU, 2021).

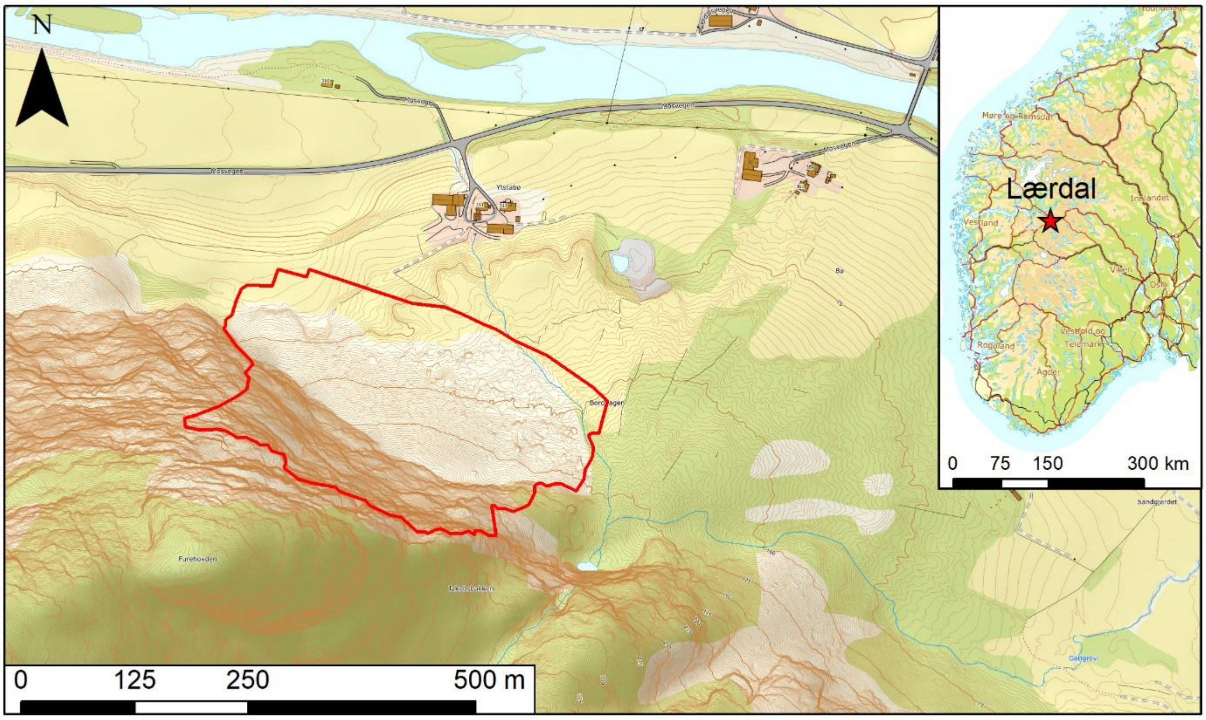

Figure 3.3 Location of the study area next to the Ytstabø farm in the Lærdal valley, where the red polygon defines the area that was surveyed and modelled. The inset map shows the study area location on an overview map over southern Norway (Kartverket, 2021).

3.4 Straumvatnet

There are two study areas located next to the Straumsvatnet lake, in Nordland county (figure 3.4). The largest study area covers nearly the entire southern mountainside of Straumklumpen, at 4-700 m.a.s.l. and measures 1340 m in length. Straumklumpen study area consists of a gently dipping rock slope and a well-developed talus. The rock slope is SW facing and the surveyed slope section is approximately 540 m high. The slope curvature, in the dip direction, is concave in the lower half of the slope and convex in the upper half. Most of the rock slope have angles of 40° with some steeper area and are therefore potential rockfall source areas. The talus covers a large area and is present below most of the rock slope. Some parts of the talus are less active and largely vegetated, while other areas display signs of recent and frequent rockfall activity. The rock consists of granite and granitic gneiss (NGU, 2021).

The smaller study area is situated east of Straumsvatnet, above the mountain road that serves as an access road for the local power plant, in a part of the slope called Ørnlia. The Ørnlia study area lies at 280-425 m.a.s.l. and measures 230 m in length. It consists of a gently dipping rock slope and a talus. The rock slope is W facing and the surveyed slope section is approximately 125 m high. Most of the rock slope have angles of 50º and are therefore potential rockfall source areas. Parts of the talus appear unvegetated which indicates recent rockfall activity. The rock consists of granitic gneiss (NGU, 2021).

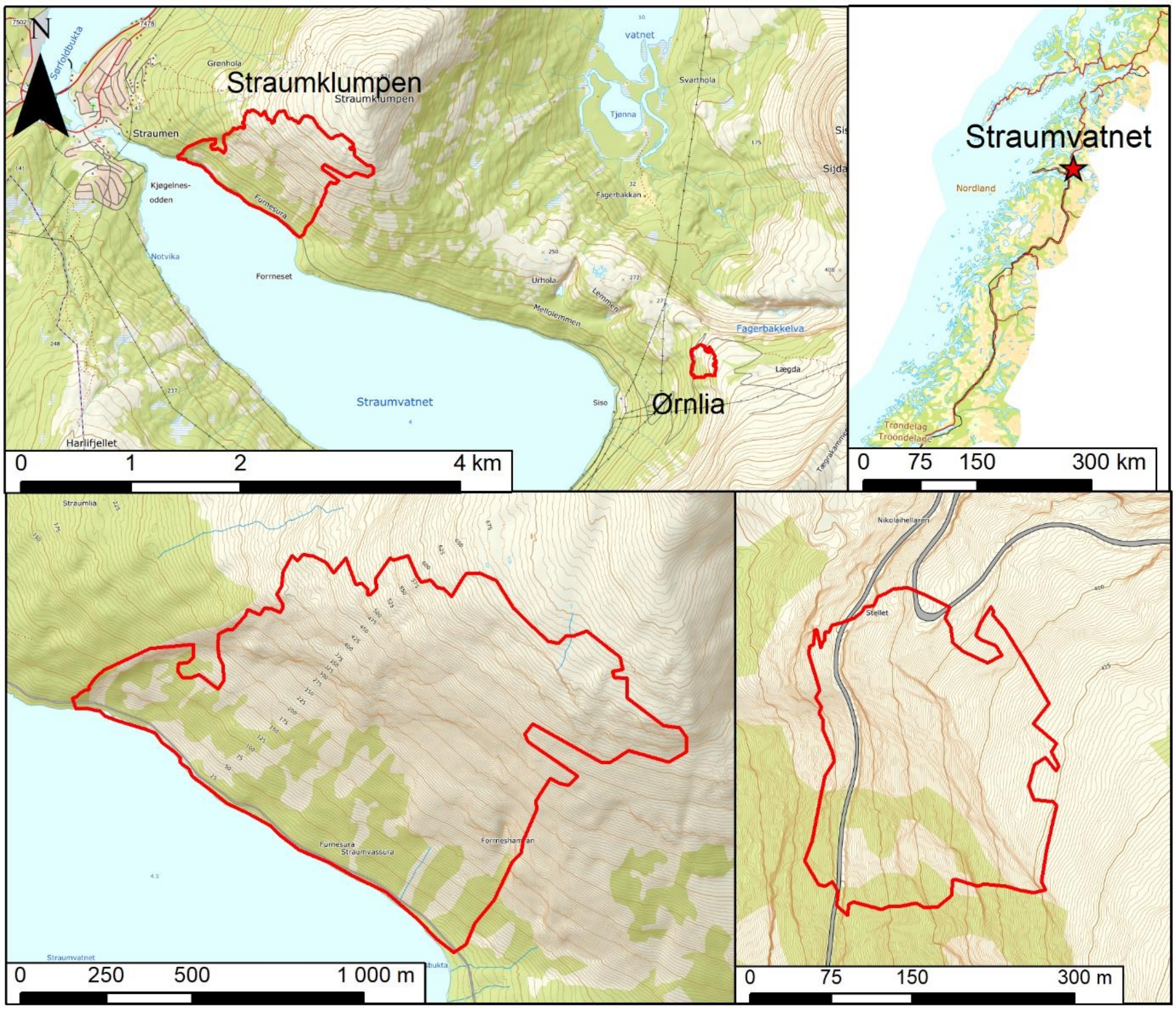

Figure 3.4 The top left map shows the locations of the two study areas next to Straumsvatnet in Nordland county, where the red polygons define the areas that were surveyed and modelled. A closer view of the topography in each study area is given in the lower maps – with Straumklumpen to the left and Ørnlia to the right. The overview map to the upper right shows the location of Straumsvatnet in central-northern Norway (Kartverket, 2021).

4 Methods

4.1 Data Collection

4.1.1 Fieldwork

Fieldwork was carried out on June 3rd (Tunhovdfjorden), August 10th – 13th (Valle), September 23rd – October 4th (Straumvatnet) and December 12th – 13th (Lærdal). In total 17 days were spent in the study areas. Fieldwork consisted of topographic surveys of rock slopes and taluses, using aerial SfM photogrammetry (section 2.1.2). The survey procedure was to place cross-markers on ground control points (GCPs) within the survey area, record the positions of these with Global Navigation Satellite Systems (GNSS) and obtain continuous and overlapping photo coverage of the survey area with a Remotely Piloted Aircraft System (RPAS).

4.1.2 Ground Control Points

Reference points were marked in the survey areas, to be used for two purposes during data processing – control points would be used to georeference the photogrammetric 3D-models and check points would be used to validate the georeferencing. In this chapter both types of reference points are jointly referred to as ground control points (GCPs), because during the fieldwork it had not yet been decided which of the reference points that would be used for what purpose.

Plastic sheets with crosses were used to mark the GCPs at the study area Tunhovdfjorden, while paper printouts with crosses were used at the other locations. The paper printouts were not laminated, in order to avoid reflections from glossy surfaces. The cross-markers were placed on flat surfaces within clear line of sight of the airspace above. Locations were chosen to ensure that the RPAS would be able to capture each marker from different angels. A minimum of 10 GCPs were used per survey area, which is the recommended number required to achieve high georeferencing accuracy in the photogrammetric reconstruction. Ideally GCPs should be evenly distributed throughout the survey area (Agisoft, 2021a), however, due to the steep inaccessible terrain it was not possible to obtain an even distribution. The survey areas were characterized by rock walls and the GCPs were placed at the base of these, mainly in taluses.

Figure 4.1 Left) a ground control point (GCP) on a boulder, marked with a cross. Right) the GNSS device (Altus APS-3G) used to record positions of the GCPs. The GNSS device is mounted on a pole, with the field computer attached to it.

4.1.3 GNSS Measurements

The positions of the GCPs were recorded with an Altus APS-3G GNSS receiver at the Tunhovdfjorden, Valle and Lærdal study areas (Figure 4.1). This is a Real Time Kinematic-Differential GNSS (RTK-DGNSS) device that utilises satellites from GPS, GLONASS, Galileo and BeiDou to record positions (Altus Positioning Systems, 2015). The device receives real-time correction data from the CPOS (centimetre positioning) service provided by the Norwegian Mapping Authority. When distances between permanent geodetic stations in the area are around 35 km, horizontal and vertical measurement accuracy associated with the CPOS service is 8 cm and 17 cm, respectively (Kartverket, 2020).

The GNSS receiver was mounted on a 2 m high pole and the pole height was factored into each measurement. The Archer 2 field computer (from Juniper Systems) and the SurvCE software (from Carlson Software Inc) were used to manage the data collection. Every GNSS recording was taken as an average of 10 measurements with one second intervals. At least two recordings were taken at every GCP, with some hours between recordings. This was done in order to get time-independent recordings, which is important for identifying measurement errors related to the satellites and the atmosphere. When recording at different times during the day, different combinations of satellites are used, and atmospheric conditions may change.

At the study area in Lærdal, the GNSS device was not able to obtain fixed (highest accuracy) solutions for the coordinates and instead raw GNSS data were logged for 10 min at every GCP. This was inconvenient since raw data requires post processing to determine positions. Recording difficulties at the Lærdal study area (figure 3.3) could be due to the location of the GCPs just below a steep north facing rock face in a narrow valley, which effectively blocks out areas of the sky and could result in poor satellite geometry. To achieve accurate GNSS measurements it is important that the satellites being used are spread out in different directions resulting in what is known as a good satellite geometry (Langley, 1999). Dilution of precision (DOP) is a measure of the error in GNSS positioning caused by satellite geometry, with higher values indicating poorer geometry and lower positioning accuracy (Kjerstad, 2020). An overview of the number of satellites and DOP values recorded during the GNSS measurements is given in table 4.1.

Due to unavailability of RTK-DGNSS equipment, a handheld Garmin GPS 60CSx was used to record the GCPs at the Straumvatnet study locality (figure 3.4). The device has considerably lower accuracy with a 95 % confidence of achieving error below 10 m (Garmin, 2007), although it still has the capacity to produce results with an acceptable degree of accuracy for the purposes of this study. Each position recording is an average of measurements taken over several minutes. In the end, the recordings taken with the Garmin GPS 60CSx proved to be of too low accuracy (1.2-11 m, in 3D) to be used for georeferencing the model. The survey at Straumvatnet coincided with unstable space weather conditions (NOSWE, 2021), which can have a negative impact on the accuracy of GNSS measurements, especially at high latitudes (SWPC, 2021).

Table 4.1 Overview of the differences between the survey areas, with regards to GNSS device, measurement status, satellite number and satellite geometry.

Study Area	Device		Status	Number of satellites	PDOP
	Brand/model	Type			
Tunhovd	Altus APS-3G	RTK-DGNSS	Fixed solution	Ra 9 – 12, M 10	Ra 1.8 – 3.9, M 2.6
Valle	Altus APS-3G	RTK-DGNSS	Fixed solution	Ra 5 – 11, M 9.6	Ra 1.6 – 2.9, M 2.0
Lærdal	Altus APS-3G	RTK-DGNSS	Raw data logging	Ra** 5 – 13, M** 9.8	NR
Straumvatnet	Garmin GPS 60CSx	Direct one-frequency GNSS	Autonomous	NR	NR

* PDOP = position dilution of precision (3D), Ra = range, M = mean, NR = not recorded. **Estimated from visual inspection of "occupation view", which is a graphical presentation of the satellites being measured to during data logging.

4.1.4 RPAS Photo Collection

4.1.4.1 Setup

All the surveys were conducted with a DJI Mavic Pro (Figure 4.2) provided by the University of Oslo. The RPAS consists of a foldable drone and a remote controller. The flight control app DJI Go 4, version 4.0 (DJI, 2020), was installed on an iPad and connected to the remote controller used to operate the drone. Photos with associated metadata were written to a 32 GB micro-SD card in the drone. The metadata includes information about the camera lens, sensor properties, camera settings, orientation, and position. The photos were stored in DNG file format, which is a raw image format with lossless compression.

The DJI Mavic Pro contains an onboard GNSS receiver that utilizes GPS and GLONASS satellite systems to record the camera position during photo capturing (DJI, 2017). The RPAS utilized the WGS84 coordinate system with ellipsoidal elevations. The DJI Mavic Pro has a built-in camera with a 26 mm (35 mm format equivalent) F/2.2 lens and a 1/2.3" CMOS sensor that takes 12.35 MP photos (DJI, 2017). The camera is mounted on a 3-axis gimbal that helps maintain the camera orientations during movement and allows the operator to change the camera angles (DJI, 2017).

Figure 4.2 DJI Mavic Pro drone was used to perform the photogrammetric surveys. The drone was provided by the University of Oslo.

4.1.4.2 Survey

All the surveys were performed with manual flight. Each survey area was divided into sections and the photo collection was conducted along sub-parallel lines within each section. It was attempted to maintain 80% forward and 60% lateral overlap between photos, as recommended by Agisoft (2021a). Photos were collected at a near constant distance perpendicular to the topography, to achieve consistent coverage. GCPs were also photographed at closer range, for easier recognition during processing. Photos were captured with the camera orientated both perpendicular to the average ground surface and with varying levels of obliqueness. Since the target in the scene was stationary and most of the photos were captured when the RPAS was hoovering, as opposed to drifting/flying, the resulting distortions are expected to be minor. The obtained ground sampling distance (GSD) varies between 1.4 and 2.2 cm/pixel for the different survey areas, which corresponds to average flight heights of 41 - 70 m.

Surveys were performed during the time of day when lighting conditions were most favourable to avoid shadows in the photos. Photos were captured with automatic adjustment of shutter speed and ISO-value.

4.1.4.3 Regulations and Considerations

The Civil Aviation Authority regulates the use of RPAS in Norway (Luftfartstilsynet, 2021b). According to the flight regulations at the time of surveying, RPA must keep a minimum horizontal distance of 50 m from people, vehicles and buildings (Luftfartstilsynet, 2020). Some of the surveying took place close to roads, where the RPAS operator had to have control on approaching cars and be prepared to divert the drone. Furthermore, it is required that the operator always maintains a visual line of sight (VLOS) to the RPA (Luftfartstilsynet, 2020). At the time of surveying, the RPA maximum flight height was restricted to 120 m vertically above the ground (Luftfartstilsynet, 2020). Due to the height restrictions and the requirement for VLOS, several different take-off points were used to cover most of the survey areas. The gentle slopes at Valle and Straumklumpen allowed the RPA to capture photos along the full height of the slope and still remain within the required 120 m above the ground.

In Norway, the disturbing of animals or birds is prohibited (Naturmangfoldloven, 2020, § 15), so the RPAS operator must take this into consideration when planning the survey and pay attention to the wildlife during fieldwork. When flying next to steep slopes and rock faces birds can be an issue. Birds of prey may try to attack the RPA and become injured by the propellers, a situation that needs to be avoided. On some occasions during surveying, falcons and eagles were observed, forcing the flight plan to be changed.

4.1.5 GCPs from LiDAR DEMs

Since the GNSS measurements for the GCPs at Straumklumpen and Ørnlia study areas had to be discarded due to low accuracy (1.2-11 m, in 3D), an alternative method was needed to obtain reference points. Further, the Valle study area GCPs were poorly distributed, and the project required additional GCPs. As such, several additional reference points were picked using GIS software. Orthorectified photos from aerial surveys were used to identify suitable and recognizable point features. The features were chosen from areas with relatively smooth terrain and no dramatic changes that might increase the uncertainty of extracted altitude values. Points were placed on these features and evenly distributed throughout the survey areas. Horizontal coordinates were generated for each point and their elevations were extracted from DEMs (Digital Elevation Models) based on aerial LiDAR (Light Detection and Ranging) surveys. Point coordinates were then exported as txt files and utilized for georeferencing the photogrammetric models. Accuracies of the GCPs were estimated to be 35-50 cm, based on the resolution and georeferencing accuracy of the orthophotos and DEMs (table 4.2).

Table 4.2 Datasets used for identifying suitable GCP placements and extracting their coordinates.

Study Area	**Dataset**			
	Type	**Name**	**Georeferencing Accuracy [m]**	**Resolution [m]**
Valle	Orthophoto	Agder 2019[1]	< 0.35*	0.1
	DEM	NDH Valle 5 pkt 2017[2]	0.021**	0.25
Ørnlia & Straumklumpen	Orthophoto	Sørfold 2018[3]	< 0.35*	0.1
		Nordland Nord 2015[4]	0.608*	0.25
	DEM	NDH Fauske 2 pkt 2017[5]	0.031**	0.5

[1] (Geovekst, 2019) [2] (Kartverket, 2017b) [3] (Geovekst, 2018) [4] (Omløpsfoto, 2015) [5] (Kartverket, 2017a)
*Horizontal RMSE. **Vertical standard deviation.

4.2 Data Processing

4.2.1 GCP Coordinates

The GNSS measurements were compiled in Excel spreadsheets, where the average coordinates horizontally (northing and easting) and vertically (elevation) were calculated for every GCP. The standard deviation for each averaged coordinate was calculated and used as measurement precision. The precision can be used as a proxy for accuracy. The residual of an individual measurement can be defined as the difference between that measurement and the averaged value of a group of measurements. In surveying, a measurement is considered to have a gross error if the residual has a higher value than the standard deviation multiplied by three (Kartverket, 2015). Measurements with gross errors were excluded from the dataset.

The GNSS measurements were recorded in the ETRS 1989 UTM zone 32N coordinate system and with ellipsoidal elevations. The vertical coordinates were converted from ellipsoidal to orthometric elevation, in the vertical datum NN2000. The difference between ellipsoidal and orthometric elevation is the theoretical reference surface being used. The orthometric elevation is given as the height above the geoid, more commonly referred to as height above mean sea level, whereas the ellipsoidal elevation is given as the height above the ellipsoid (Rød, 2020). Elevation conversions were performed in either GISLine Trans or in Agisoft Metashape Professional, during photogrammetric processing.

Post processing of the raw GNSS data logged in Lærdal was performed in GISLine Trans and Topcon Tools. The GCP coordinates were calculated based on GNSS measurements acquired from the closest base stations (ARDA and TYIC), in addition to the raw data logged in the survey (T. Eiken, personal communication, December 2020). The averaged GCP coordinates and corresponding measurement precisions for each survey area were saved in a txt-file for later use during photogrammetric processing.

4.2.2 Photogrammetric Processing

4.2.2.1 Software

Photogrammetric processing of the collected photos and generation of 3D-models were performed using Agisoft Metashape Professional, version 1.7.1 (Agisoft, 2021b). This is a widely used software which provides advanced tools for the entire workflow, from import of raw photos to export of point clouds, 3D models, DEMs and orthophotos. Metashape is not an open-source software and very little information has been made public regarding the algorithms used in the software. The system requirements for the workstation depend on the number of photos imported to a project, the resolution of the photos, which processes that will be performed and the desired product resolution. The software was run successfully on a workstation with Intel(R) Xeon(R) W-3235 CPU @ 3.30GHz, 96 GB RAM and NVIDIA Quadro RTX 4000 GPU.

4.2.2.2 Workflow and Settings

The photogrammetric workflow used in this study is based on the general workflow outlined in the Metashape manual (Agisoft, 2021a). While some processing steps are universal, the most appropriate workflow depend on the properties of the input dataset as well as the intended use of the resulting model. Processing steps and settings in the workflow were tailored to fit this specific study, through systematic testing and visual inspection of results. Arguments and explanations related to optimizing the workflow were obtained from posts in the Agisoft forum (Agisoft, 2021c), where both Metashape users and software developers are active. The full workflow is given in Appendix A and the most important steps of the workflow are explained below:

Photo Import and Quality Check

Photos were imported as DNG files with metadata containing information on camera positions, orientations and settings. To achieve good virtual models, it is important that the input is of good quality, meaning photos are focused and not over/under exposed. Metashape has a feature for automatic estimation of image quality. The feature identifies the best focused part of every photo and calculates the relative sharpness of each photo, in comparison to other photos in the dataset (Agisoft, 2021a). Though most of the collected photos were of good quality, some photos had an estimated quality value below the recommended threshold of 0.5 units (Agisoft, 2021a) and were excluded from the dataset.

Photo Alignment and Sparse Cloud Editing

The first processing step is the photo alignment, during which a feature detection algorithm is used to identify and describe interesting points (referred to as key points) in the source photos. The key point descriptors are then used to find matching points in other photos. A tie point is a set of key points that have been matched between different photos and represent the same feature point. Tie point coordinates are calculated with aerial triangulation and bundle block adjustment, creating a 3D-network of tie points which is visualized in the form of a sparse point cloud. Simultaneously these processes also adjust the camera positions and refine the camera orientations parameters (Agisoft, 2021a).

When running the alignment process on the survey datasets the accuracy was set as high, which means the photos are processed at their original resolution without any downscaling. The preselection option uses different criteria to group together photos that are likely to be overlapping and contain the same features, in order to reduce the processing time (Agisoft, 2021a). Both generic preselection, which uses lower accuracy settings to find overlapping photos, and source preselection, which uses camera locations to find overlapping photos, was applied in this study. The maximum number of points to be sampled in each photo was kept at the default value for key points (40 000) and tie points (4000) alike. The option “adaptive camera model fitting” was applied for an automatic selection of which camera parameters to include in the adjustment, based on their reliability estimates.

After alignment the sparse point cloud was inspected visually, and unwanted points were removed both manually and through filtering options. Points with a high reprojection error (>0.5) or a high reconstruction uncertainty (>25) were selected with the “Gradual selection” tool and deleted. Applying these filters may reduce noise and increase accuracy in the following processes (Agisoft, 2021a).

For one of the study areas, Ørnlia, there was a problem with photo alignment. The software was not able to recognize that two sets of images collected during different days actually viewed the same scene and should be aligned to form a single connected point cloud. Instead, two point clouds separated by a vertical offset were generated. This was caused by very large differences in recorded altitude between the two sets of images. A python script (Poliarnyi, 2021) was used in Metashape to manually change the altitudes recorded in the image metadata. One set containing 649 images was lowered by 66 m, which was the estimated average error. The second set containing 1098 images was elevated by 72 m. Applying this solution prior to alignment allowed for a successful joining of the separated point clouds.

GCP Import and Marker Placement

The averaged GCP coordinates and calculated measurement precisions from the GNSS recordings were imported in a txt-file. Each GCP (referred to as markers in Metashape) was localized and manually indicated on at least two photos, before applying a filter to select only the photos in which the marker is visible. The software automatically calculates and projects the position of the marker in the photos and predicted marker positions then needs to be refined manually (Agisoft, 2021a).

Markers were divided into control points (used to reference the model) and check points (used to validate the referencing accuracy of the model). The markers with the lowest measurement errors were preferentially chosen as control points. Check points were chosen so that they would be positioned in between and relatively close to control points. A larger number of markers were used as control points than check points.

Optimize Camera Alignment

This feature runs another bundle block adjustment to further refine camera parameters and tie point positions. The adjustment is based on image projections of tie points and markers, camera coordinates and control point coordinates. The importance of each measurement is decided based on their corresponding accuracies (Agisoft, 2021a). Since the markers have higher measurement accuracies than the camera coordinates, the markers will be weighted higher. The optimization settings applied in this study, include fitting values to all available camera parameters except k4 (f, k1-k3, cy, cx, p1, p2, b1, b2).

The optimization process provides error estimates for markers, and updates the error estimates for camera positions, camera parameters and tie points reprojections (Agisoft, 2021a). The sequence of first filtering out tie points with high reprojection errors, followed by a bundle block adjustment, was repeated a couple of times to reduce errors and improve accuracy.

Generation of Dense Point Cloud

In Metashape, the process of building a dense point cloud starts with the generation of depth maps (Agisoft, 2021a). Depth maps are images containing information about the distance between a viewpoint and a 3D-surface, which in SfM photogrammetry are the camera viewpoint and the ground surface (Smith et al., 2016). Distances are calculated based on the stereo view from an overlapping image pair and their corresponding orientation parameters, estimated in the bundle adjustments. A combined depth map is created for each camera by merging the individual depth maps. Points are then extracted from the depth maps and coloured based on the photos (Agisoft, 2021a).

In the work presented here, the dense point clouds were generated with high quality, which according to Agisoft corresponds to a downscaling by a factor of 4 from original photo resolution (2021a). Reducing the quality to high speeds up the processing time (Agisoft, 2021a), while still producing excessively dense point clouds. Depth filtering mode was set to mild, which is a requirement for basing the mesh reconstruction on the depth maps. This mode preserves small details that might be important in the later analyses of discontinuity roughness. The options of calculating point colours and calculating point confidence were both enabled. The confidence value represents the number of depth maps that was used to generate each point (Agisoft, 2021a). Editing of the dense cloud was done through filtering out points with low confidence values (< 5) and manually removing unwanted points (noise, outliers etc.).

Discontinuity analyzes can be performed directly on the dense point cloud, imported to the PointStudio software (Maptek, 2021).

Generation of 3D Surface Models

A mesh model was generated for each survey area, to be used as the basis for volume analyzes in PointStudio. The surface of a mesh consists of vertices, edges and polygons (referred to as faces). Different settings were tested before choosing to use the depth maps as source data and to use an arbitrary surface type, which makes no assumptions on the type of surface being modelled. The generated mesh was edited through filtering out isolated mesh fragments. A photorealistic texture was then created for the edited mesh.

Tiled models were generated to be used for visualization purposes in ArcGIS. The tiled model is a gridded surface model that maintain high resolution, while also allowing fast responses due to the hierarchical visualization levels (Agisoft, 2021a). The mesh was used as source data for the reconstruction.

Generation of DEM and Orthophoto

Digital elevation models (DEMs) were generated with the purpose of using them as the basis for creating hillshade maps in ArcGIS, which in turn would be used as visualization. Orthophotos were also generated for visualization purposes. DEMs with different resolutions and an orthophoto were prepared for the survey area in Lærdal and delivered to Elise Morken, as part of a MSc theses collaboration with focus on rockfalls. In the applied workflow, the dense cloud was used as source data for calculating the DEM, and the DEM was then selected as the surface onto which the orthophoto would be projected.

4.3 Model Validation

4.3.1 Georeferencing Accuracy

The georeferencing accuracy of a model can be defined as the mean difference between modelled point positions and their actual locations in the study area. Metashape provides 3D error estimates for control points (GCPs) and check points (CPs). Ideally, the given root mean square error (RMSE) values should be low (cm-dm level) and about the same magnitude for GCPs and CPs. Low RMSE values indicate high georeferencing accuracy and that credible GCP measurement precisions were used as input. A limitation of using this method is that the estimated georeferencing accuracy only applies to the model area that is bound by the reference points. A more comprehensive validation of the georeferencing accuracy was achieved by performing cloud-to-cloud comparisons in the open-source software CloudCompare (CloudCompare, 2021a). LiDAR point clouds from Høydedata with a high georeferencing accuracy (3-10 cm) were used as reference datasets (table 4.3).

Table 4.3 Point cloud datasets used as reference in cloud-to-cloud comparisons.

Study Area	**Point Cloud Dataset**			
	Name	**Vertical Georeferencing Accuracy [m]**	**Horizontal Georeferencing Accuracy [m]**	**Point Density [pts/m^2]**
Tunhovd	NDH Nore og Uvdal 5pkt 2018[1]	0.029*	0.09*	5
Valle	NDH Valle 5 pkt 2017[2]	0.021*	0.10*	5
Lærdal	Sogndal_Aurland_Lærdal 2pkt 2014[3]	0.04**	0.10**	2
Ørnlia & Straumklumpen	NDH Fauske 2 pkt 2017[4]	0.031*	0.09*	2

[1] (Kartverket, 2018) [2] (Kartverket, 2017b) [3] (Kartverket, 2014) [4] (Kartverket, 2017a) *Measured standard deviation. **Maximum tolerated standard deviation according to the applicable standard, FKB-Laser-C-DTM10 (Kartverket, 2019).

The C2C function in CloudCompare computes distances between each point in a cloud and the nearest point in a reference cloud (CloudCompare, 2021b). Since the reference clouds have considerably lower point densities than the photogrammetric clouds, the nearest point might not be the best approximation of the real surface. Local modelling that estimates the surface around points was applied to get more accurate distance estimates. The quadratic function was used as the local model and computed for the spherical neighborhood surrounding the nearest point. The radius of the sphere was set to 2.4 m when using reference datasets with a point density of 2 pts/m^2 and set to 1.5 m when the reference datasets had a point density of 5 pts/m2. Both radii correspond to 35 points (on average) within the spherical neighborhood.

Inspection of C2C results revealed that the longest distances coincided with holes in the reference models caused by steep topography (figure 4.3). Therefore, the distances above a threshold value were considered an effect of limitations in the reference dataset, rather than quantifiable errors in the photogrammetric models that were being evaluated. Based on these observations the maximum distance for the C2C computation was set to 3 m, meaning that points with longer distances are recorded with the threshold value instead.

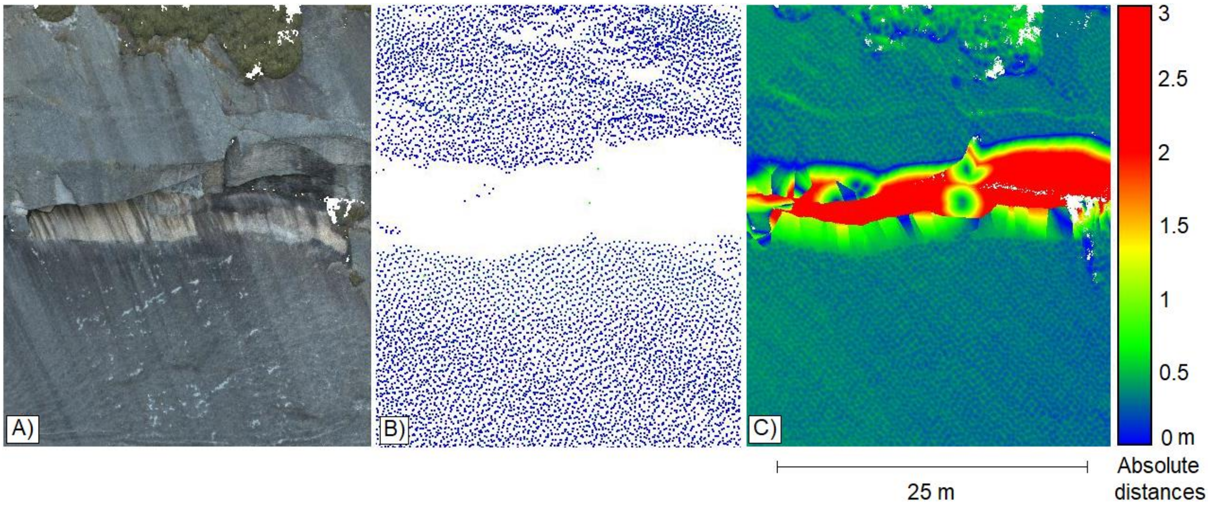

Figure 4.3 A) Section of a photogrammetric point cloud for Valle study area. The central part depicts a steep, partially overhanging area in the rock slope. B) LiDAR point cloud from Høydedata, for the same section. The model has a hole in the steep, central area. C) Computed distances between the photogrammetric point cloud and the LiDAR point cloud, colour coded onto the photogrammetric cloud. Red colour indicates the longest distances.

4.3.2 Systematic Errors

Models produced through SfM processing of aerial images taken with consumer-grade cameras are often subject to systematic error, expressed as doming of the model surface. Such errors are generally caused by a combination of using image sets with near-parallel viewing directions, and inaccurate camera calibration (James & Robson, 2014). The presence of systematic error was evaluated based on observed patterns in camera residuals after camera self-calibration, and error magnitudes were estimated based on computed C2C distances.

4.4 Analysis

4.4.1 Extraction of Discontinuities

Digital mapping of discontinuities was performed on the validated 3D models, using the PointStudio software produced by Maptek (Maptek, 2021a). PointStudio is a commercial software package that provides a variety of applications for working with point clouds, including geotechnical tools for mapping, and analysing structural data (Maptek, 2021b). Since it is possible to use either point cloud or mesh for extracting discontinuity surfaces, the functionality of both was tested. Using a mesh proved to be faster and less computer demanding. The mesh models were therefore used as a basis for the geotechnical analyses.

What kind of settings that should be used for the described PointStudio tools depend on the quality of the model, the scale of the investigated area, and the character of the discontinuities. The settings used in this study were chosen partly based on communication with the experienced PointStudio user Jessica Ka Yi Chiu at the Norwegian Geotechnical Institute (personal communication, June 2021), and partly through testing different values to find good fits for the specific data sets used. In PointStudio, there are three different tools that can be used for mapping discontinuity surfaces, and these are presented below.

Extract

The most automated tool is ‘extract’, which was also used most frequently in this study. The user defines one discontinuity by drawing a polygon, and the software then analyses the topography of the entire model in search of similarly oriented surfaces. It is a very fast method for extracting large amounts of data. The process of checking the extracted surfaces is, however, considerably more time consuming. Since the tool cannot differentiate between different types of surfaces, erroneous surfaces must be sorted out manually. Incorrect surfaces were often extracted from displaced blocks or vegetated areas in the models (figure 4.4), though this was mitigated by cleaning the models from unnecessary parts before starting the extraction. The angle threshold for how much the dip and strike of extracted planes were allowed to vary was set to 10º, while the minimum and maximum area of extracted planes were set to 0.5-1.2 m^2 and 40-50 m^2, respectively.

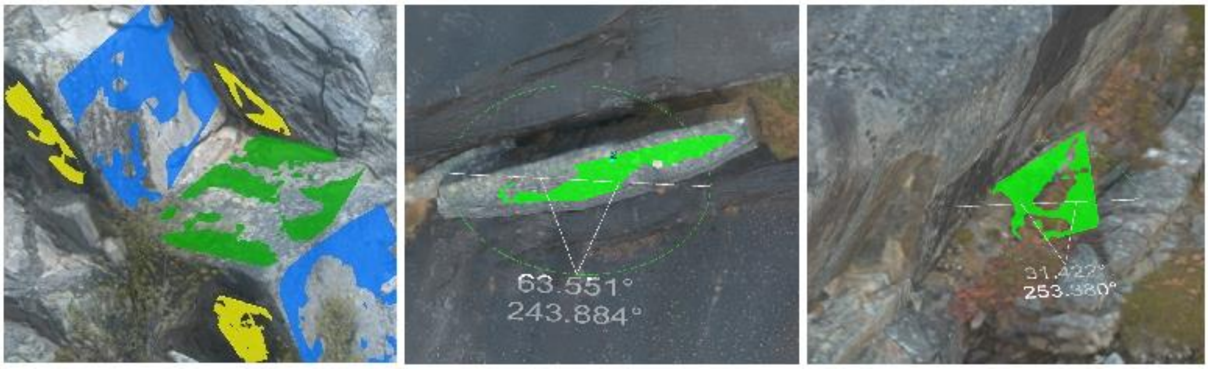

Figure 4.4 Examples of digitally mapped surfaces using the ‘extract’ tool in Maptek PointStudio. The left figure shows a correct extraction of discontinuity surfaces, while the middle and right figures illustrate incorrect extractions on a displaced block and a patch of vegetation, respectively. The surfaces are annotated with the dip and dip direction values.

Smart Query

‘Smart query’ is a semi-automated tool, where the user clicks ones on the desired discontinuity surface. The software then analyses the surrounding terrain and determines the extent of that surface, according to the applied settings. The ‘normal difference threshold’ specifies how much the orientation of the surface is allowed to vary, in order to be included as part of the plane. Values of 3-10º were used in this study. After the extent of the surface is determined, the software calculates the best fit plane. ‘Smart query’ was used as a complement to the more automated ‘extract’ tool, to pick surfaces that were not recognized by extract. It was also used as the main method for Lærdal study area, because it was faster to use than to evaluate the excessive number of both correct and incorrect surfaces that had been identified with ‘extract’.

Query dip and strike

The most manual tool for mapping discontinuities in PointStudio is ‘query dip and strike’, for which surfaces are manually defined by the user. The user draws a polygon along the perimeter of a discontinuity surface in the model and the software calculates the best fit plane. This tool was only used occasionally for picking discontinuities but was useful when analysing slope geometry for the kinematic analyses.

Merge

The ‘merge’ tool was used to join closely overlapping and similarly oriented discontinuity planes that would be better represented as one plane. Maximum spacing between merging planes was set to 10-15 cm, and they were allowed to have a maximum angle difference of 5-7^o.

4.4.2 Kinematic Analysis

Stereonet-based kinematic analyses were conducted to identify discontinuity sets, their mean dip and strike, and possible failure modes in the studied rock slopes. An initial assessment was done in Maptek PointStudio (Maptek, 2021a), while the final analyses were performed using the Dips software produced by Rocscience (Rocscience, 2021). Discontinuity and slope planes were plotted in stereonets, using a lower hemisphere and equal area projection. The discontinuities were represented as poles, and contouring was used to define sets. Study areas with varied slope orientations were divided into more homogenous sections, for which separate kinematic analyses were performed. In each section analyses, the entire discontinuity data set for the corresponding study area was utilized. The motivation for this was that the discontinuity sets appeared to be well-distributed throughout the study area.

The study areas were tested for planar, wedge, block toppling, and flexural toppling failure modes. The kinematic criteria for these failure modes are listed in section 2.2.4. Lateral limits were set to 20º for planar and toppling failures (Hudson & Harrison, 2000; Wyllie & Mah, 2004). Empirical values for the friction angles were obtained from Li et al. (2019), who performed vigorous lab-testing on core samples of different rock types. Based on the respective lithologies at each study area (chapter 3), the friction angle was set to 27º for Tunhovd and 30º for the other study areas. The values apply to clean joints without infill material.

4.4.3 Discontinuity Characterization

The mean orientation (dip and dip direction/strike) for each of the defined discontinuity sets was calculated in Maptek PointStudio. The sets were also analyzed for spacing (i.e. perpendicular distance between planes), persistence (i.e. discontinuity length) and surface roughness.

Spacing

Discontinuity spacings between adjacent planes, along with statistics for the entire discontinuity, set were calculated using the ‘spacing’ tool in Maptek PointStudio (figure 4.5). In the spacing analysis the discontinuity planes were assumed to be infinite in size. A minimum spacing was specified to avoid misinterpretation of planes that are so close they might represent one combined plane. Too small offsets cannot be accurately mapped, and the appropriate limit depends on the quality and resolution of the model. For this study the minimum spacing was set to 15 cm. A maximum spacing was also specified, and the chosen value varied between 15-50 m for the different discontinuity sets. The starting point was always set to 50 m, and a lower value was only used when the inspection of visualized spacings revealed one or few larger outliers that appeared to be a result of mapping constraints (e.g. discontinuities located on the margins of a model, or where parallel discontinuities are visible within the spacing distance but are too small to be accurately mapped).

Figure 4.5 Illustration of output from a discontinuity spacing analysis in Maptek PointStudio. The pink planes represent discontinuity surfaces and have been reoriented according to the mean orientation of the discontinuity set. The green lines represent the distance between adjacent planes, normal to the mean orientation of the discontinuity set.

Persistence

PointStudio does not provide statistics for persistence, but a txt file containing the individual discontinuity lengths was exported for each discontinuity set. The data was then imported to Excel, where common statistics such as mean, range and standard deviation were calculated.

Roughness

The surface roughness of each discontinuity set was estimated digitally by applying the ‘query waviness’ tool, in Maptek PointStudio, to identified discontinuity surfaces on the mesh models. A sample of 2-5 representative surfaces were chosen from each discontinuity set. When applying the tool, the user draws a polygon to define the area to be queried and the software extracts parallel cross sections in the dip direction, i.e. the assumed sliding direction.

PointStudio then calculates the maximum asperity amplitude along each profile line. The subdivision size was set to 1 m.

After excluding obvious outliers, the largest amplitude found within a sample was used to determine the Joint Roughness Coefficient (JRC) of the corresponding discontinuity set. A simple estimate of the JRC was obtained by using the chart in figure 4.6, which is constructed according to the established relationship between JRC, asperity amplitude and profile length (Barton, 1982; Barton and Bandis, 1990). The JRC scale has a range of 0-20, where low values correspond to smooth, planar surfaces and high values represent rough, undulating surfaces (Barton, 1982; Wyllie & Mah, 2004).

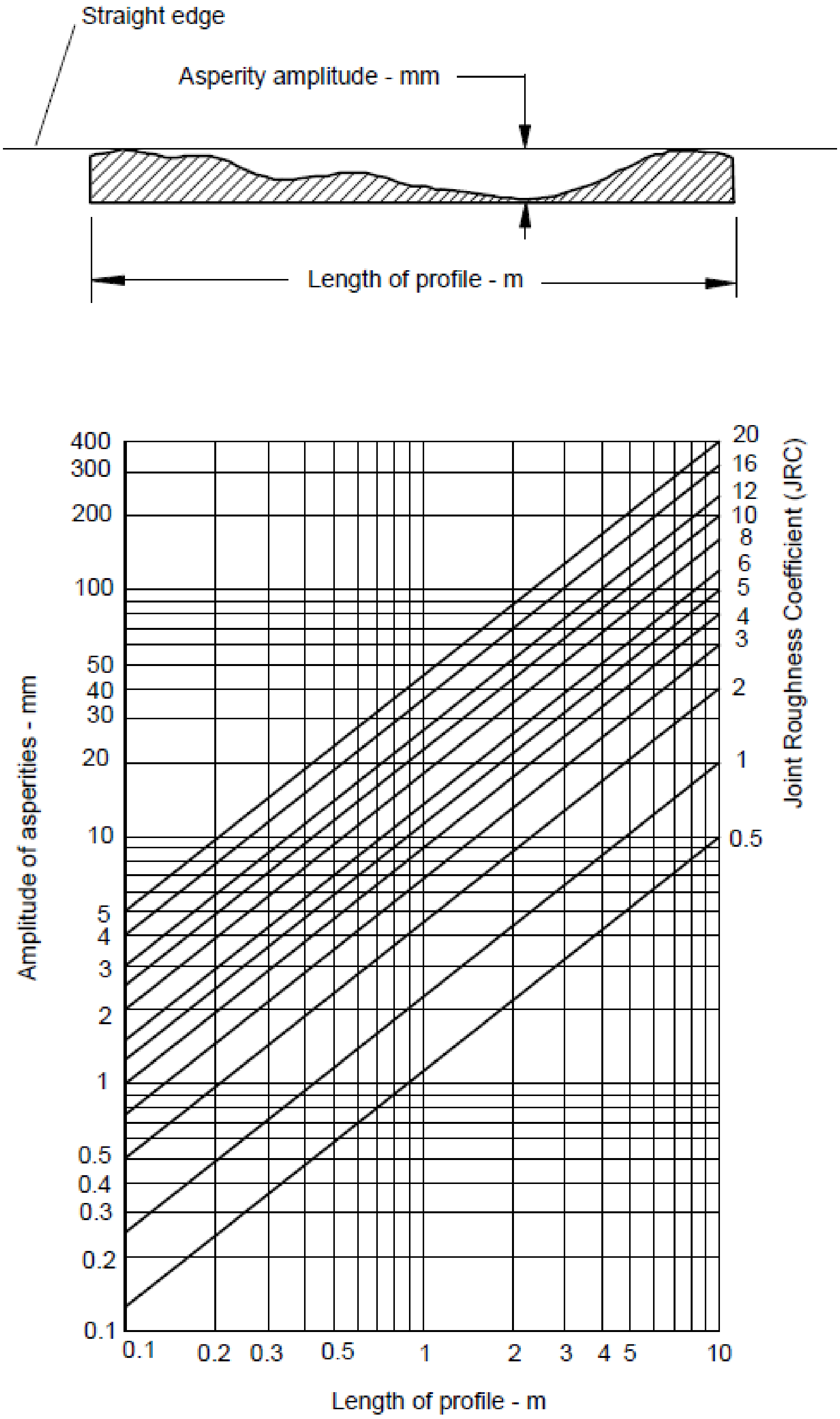

Figure 4.6 A chart for estimating the Joint Roughness Coefficient (JRC) based on measured asperity amplitudes along a surface profile (Hoek, 2007).

5 Results

5.1 Field Surveys

Topographic surveys of rock slopes and taluses were carried out at five study areas, where drone-based consumer-grade cameras and GNSS receivers were used to collect datasets for photogrammetric reconstructions. The study areas vary with regards to size, degree of vegetation, slope angle, and aspect (table 5.1). A total of 12 939 images were collected at Straumklumpen, which is the largest study are. At the considerably smaller study areas Tunhovd and Ørnlia, the collected datasets consist of 444 and 1747 images, respectively. Valle and Lærdal are moderately sized study areas, at which 2240 and 2005 images were collected, respectively. A majority of the collected images were of sufficient quality to be used as a basis for photogrammetric reconstructions. At minimum of 10 reference points were marked and recorded with GNSS for each study area. Due to low accuracy, the GNSS measurements at Ørnlia and Straumklumpen study areas had to be discarded.

Table 5.1 Overview of collected data and study area characteristics.

Study Area	Length [m]	Vertical Height [m]	Collected Images (Aligned[1])	Reference Points	Slope Characteristics	Talus Characteristics
Tunhovd	360	140	444 (99 %)	11	Steep, S-SW facing	Well-developed talus, little vegetation.
Valle	530	330	2240 (96 %)	10	Gently dipping, SE facing	Small talus, largely vegetated.
Lærdal	420	320	2005 (100 %)	11	Steep, N-NE facing	Pronounced talus fan, little vegetation.
Ørnlia	230	150	1747 (85 %)	10*	Gently dipping, W facing	Developed talus, some vegetation.
Straum-klumpen	1340	700	12 939 (91 %)	44*	Gently dipping, SW facing	Well-developed talus, large areas vegetated.

[1] Portion of images that were aligned during processing and used to generate 3D models. *Discarded due to low accuracy, see chapter 4.1.3 for details.

The focal length and f-stop were constant when taking the images, while ISO and shutter speed were adjusted automatically by the camera (table 5.2). There are large variations in shutter speed within and across surveys, ranging from 1/13 to 1/1900 seconds. ISO values are low and show little variation. Values for mean Ground Sampling Distance (GSD) and mean flight height measured normal to the ground (survey range), were estimated during processing in Agisoft Metashape. Valle and Ørnlia study areas have GSD ranging between 1.35-1.44 cm/px, corresponding to a mean survey range of approximately 40 m. Similarly, the study areas of Tunhovd, Lærdal and Straumklumpen have GSDs of 2.10-2.21 cm/px and a mean survey range of approximately 70 m.

Table 5.2 Statistic summary of image recording parameters.

Study Area	Parameter					
	Focal Length [mm]	F-stop	ISO	Shutter Speed [s]	Mean GSD* [cm/px]	Survey Range** [m]
Tunhovd	4.73	F/2.2	100	1/320 – 1/1500	2.11	67.8
Valle	4.73	F/2.2	100 – 140	1/100 – 1/1550	1.44	40.9
Lærdal	4.73	F/2.2	100 – 210	1/25 – 1/50	2.21	70.2
Ørnlia	4.73	F/2.2	100 – 200	1/50 – 1/370	1.35	42.6
Straumklumpen	4.73	F/2.2	100 – 280	1/13 – 1/1900	2.10	66.2

* GSD – Ground Sampling Distance **Ground-camera distance, measured perpendicular to the ground.

All RPAS flights and image recordings were conducted manually, without automated flight plans. Appendix B show RPAS camera positions over the study areas in map view. The study areas are colour coded according to the image overlap. Each point of the models was covered by more than 9 overlapping images, on average. The image coverage of Valle study area is somewhat uneven. Models for both Valle and Straumklumpen study areas contain discontinuous strips that could not be modelled, due to insufficient or poor-quality data. Although, the majority of the slopes have sufficient image cover and were successfully modelled. The figures in Appendix B were modified based on plots generated in Agisoft Metashape.

Reference point coordinates were recorded with an RTK-DGNSS, where a minimum of two measurements were taken at every point (section 4.1.3). The standard deviation is used as measurement precision (section 4.2.1), and calculated values are listed in table 5.3. GNSS measurements for Tunhovd and Valle study areas have small standard deviations of 1-2 cm horizontally and 2-4 cm vertically. Due to recording difficulties at the Lærdal study area, the highest accuracy measurement mode was unavailable. Instead, raw GNSS data was logged for 10 min at every point. After the required post-processing, GNSS measurement precision for Lærdal was found to be 6-18 cm horizontally and 34 cm vertically. Reference point coordinates and measurement precisions were imported to Agisoft Metahape and used to georeference the photogrammetric models.

Table 5.3 GNSS measurement precision for reference points at each study area.

Study Area	Reference Points		Standard Deviation [m]			
	GCPs	CPs	Northing	Easting	Elevation	3D
Tunhovd	8	3	Ra 0.011 – 0.015, M 0.012	Ra 0.015 – 0.019, M 0.018	Ra 0.026 – 0.042, M 0.033	M 0.039
Valle	8	2	Ra 0.009 – 0.015, M 0.011	Ra 0.010 – 0.015, M 0.013	Ra 0.021 – 0.028, M 0.024	M 0.030
Lærdal[1]	8	3	Ra 0.070 – 0.65, M 0.18	Ra 0.024 – 0.14, M 0.063	Ra 0.10 – 1.1, M 0.34	M 0.39

[1] Raw GNSS-data recorded for 10 min in every point. * GCP – Ground Control Point, CP – Check Point, Ra – Range, M – Mean

5.2 Photogrammetric Reconstructions

Collected images were processed in Agisoft Metashape according to the workflow described in section 4.2.2 and appendix A. Processing reports were generated and provided diagnostic plots for the camera self-calibration. The plots are presented in Appendix C and show the residual image distortion that the camera calibration model was unable to remove. For the Ørnlia study area, Metashape divided images into two different calibration groups and subsequently generated one plot for each. All study areas generated similar plots and an example from the Straumklumpen study area is shown in figure 5.1. The residuals display a concentric pattern with the highest distortion towards the centre and at the margins of each image. The error appears systematic, although the magnitudes of maximum residuals are small, at approximately one pixel. For Straumklumpen study area, where the survey range (i.e. camera-target distance) was 66.2 m, an image distortion of one pixel corresponds to 2.10 cm (on average) on the ground.

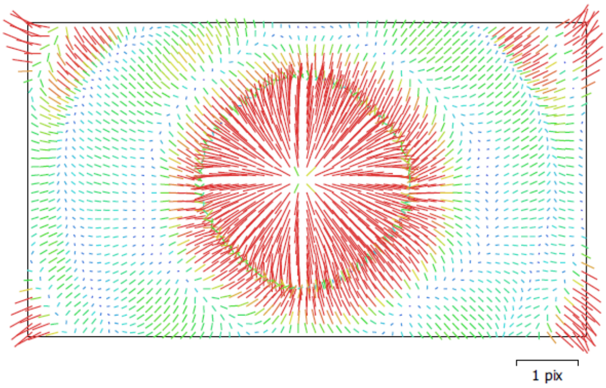

Figure 5.1 Residual image distortion after camera self-calibration in Agisoft Metashape, for Straumklumpen study area. The residual image distortion is visualised as lines, which show the direction of the distortion. The distortion lines have been greatly enlarged compared to the image frame, for better visualization. The lines are colour-coded according distortion magnitude, with red representing the largest distortions. One pixel corresponds to 2.10 cm (on average) on the ground.

The measure for georeferencing accuracy provided by Agisoft Metashape is the RMSE for ground control points (GCPs) and check points (CPs); refer to sections 4.2.2 and 4.3.1 for details. For GCPs, RMSE represents the residual error after fitting the photogrammetric network to the GCP coordinates. CPs are not part of the georeferencing process and are solely used to validate the accuracy. Appendix D contains figures displaying GCP and CP locations on orthophotos for each study area. Error estimates are visualized as colour-coded ellipses. The figures in Appendix D were modified based on plots generated in Agisoft Metashape.

A summary of the mean RMSE in 3D space is given in table 5.4. Tunhovd exhibits the lowest RMSE values at approximately 4 cm for both GCPs and CPs. Conversely, Straumklumpen is estimated to have over one meter in RMSE. RMSE given in pixels is not a measure of the georeferencing accuracy but provides a diagnostic for how precisely the GCPs and CPs were manually indicated in the images. All survey areas have relatively low RMSE values, ranging between 0.712-1.59 px. Obtained model resolutions are in the range 514-569 points/m^2 for Tunhovd, Lærdal and Straumklumpen study areas, and the resolutions for Valle and Ørnlia are more than twice as high, at 1210-1380 points/m^2.

Table 5.4 Estimated georeferencing accuracies for reconstructed models in Agisoft Metashape, given for reference points as Root Mean Squared Error (RMSE). Final model resolutions are also listed.

Study Area	Model Resolution [pts/m^2]	Reference Points			
		Type	Number of Points	Mean RMSE [m]	Mean RMSE [px]
Tunhovd	562	GCP	8	0.0355	1.38
		CP	3	0.0431	1.59
Valle[1]	1210	GCP	18	0.779	0.856
		CP	5	0.535	0.712
Lærdal	514	GCP	8	0.196	1.37
		CP	3	0.406	1.30
Ørnlia[2]	1380	GCP	16	0.307	1.05
		CP	7	0.470	1.33
Straumklumpen[2]	569	GCP	29	1.18	1.10
		CP	8	1.10	1.13

[1] Includes both reference points measured with GNSS, and points extracted from LiDAR digital elevation models (DEMs). [2] Only reference points extracted from LiDAR DEMs. * GCP – Ground Control Point, CP – Check Point.

Cloud-to-cloud (C2C) comparisons were performed to get a more comprehensive and robust validation of the models (section 4.3). LiDAR point clouds from Høydedata were used as reference models. Computed distances between the photogrammetric point clouds and the reference models were colour coded onto the photogrammetric clouds (figure 5.2). The figure also shows the photogrammetric point clouds in original colours. A summary of mean distances and standard deviations for the C2C comparisons are shown in table 5.5.

Table 5.5 Statistics for cloud-to-cloud comparisons between the reconstructed photogrammetric point clouds and LiDAR point clouds from Høydedata used as reference models.

Study Area	**Cloud-to-Cloud Comparison**	
	Mean Distance [m]	**Standard Deviation [m]**
Tunhovd	0.196	0.222
Valle	0.369	0.318
Lærdal	0.372	0.378
Ørnlia	0.165	0.176
Straumklumpen	0.596	0.420

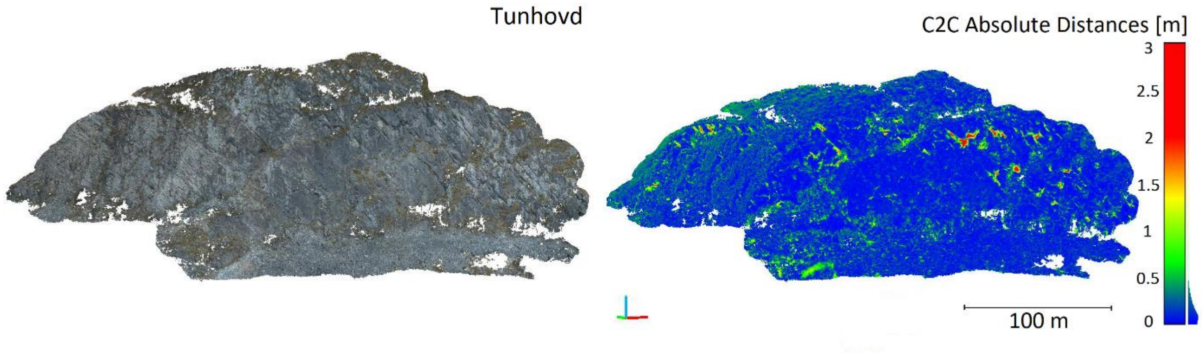

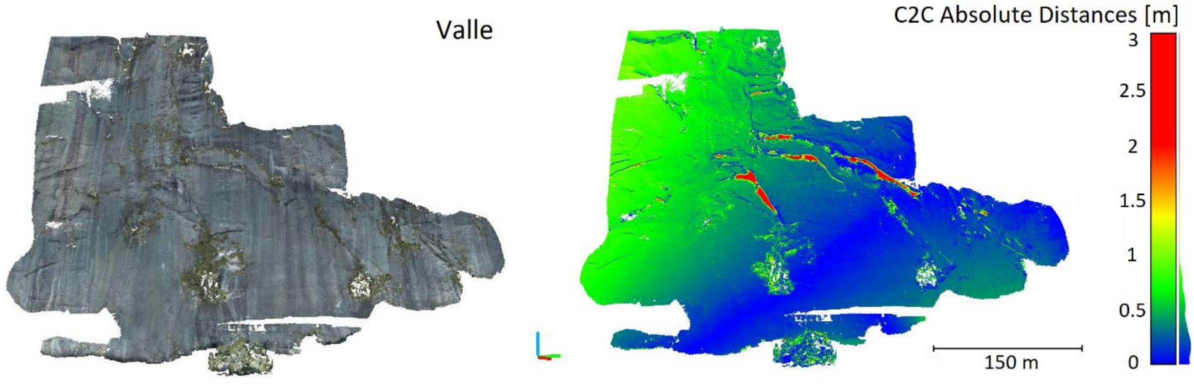

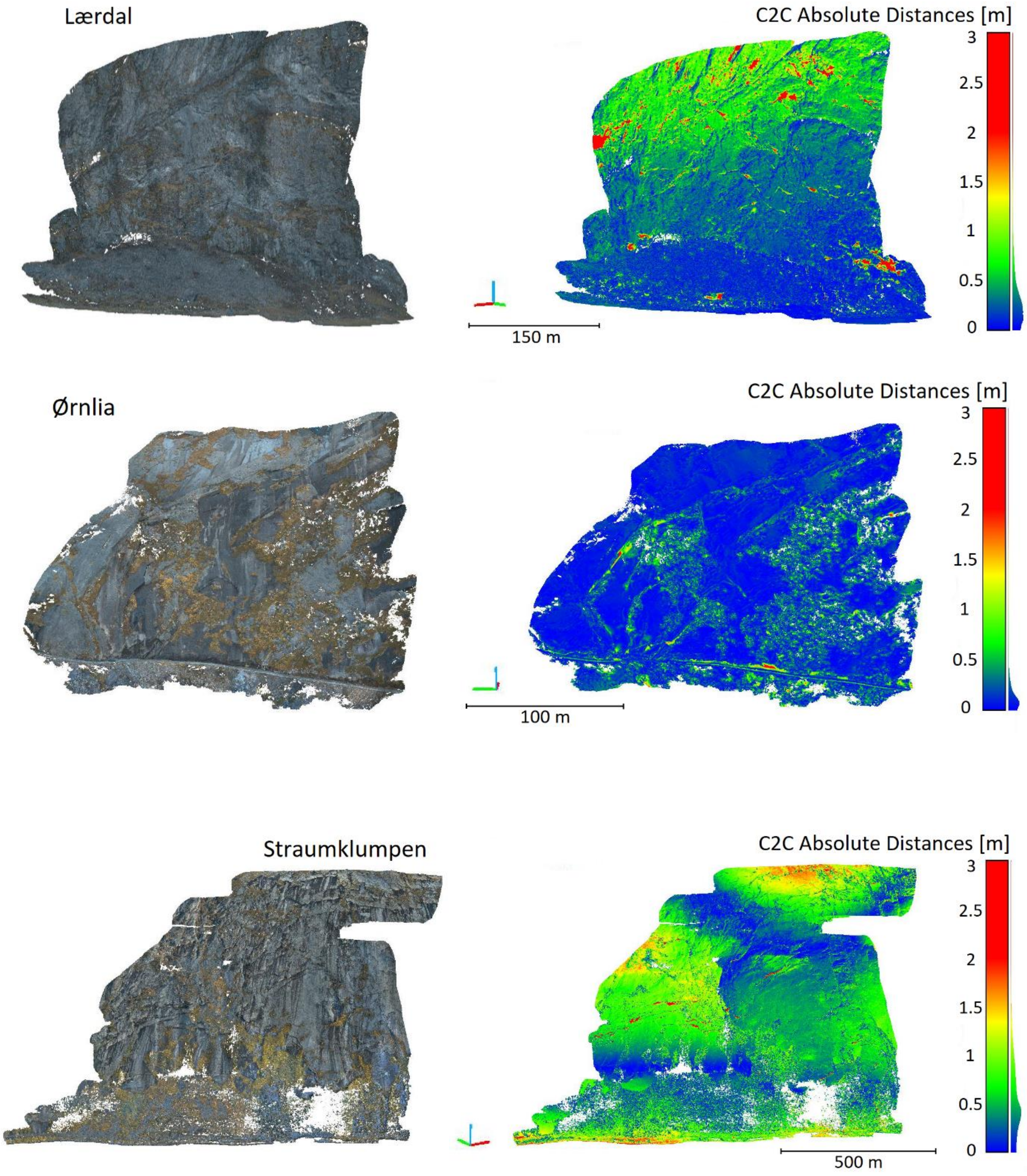

Figure 5.1 Figures to the left show reconstructed photogrammetric point clouds for each survey area. Figures to the right show computed distances between the photogrammetric models and the reference models, colour-coded onto every point of the photogrammetric cloud. LiDAR point clouds from Høydedata were used as reference models, and the C2C comparisons were made in CloudCompare. Blue colour indicates short distances and red indicates long distances.

C2C distances for Tunhovd and Ørnlia study areas are generally below 50 cm and do not exhibit any systematic error (figure 5.1). The mean C2C distance is 20 cm for Tunhovd and 17 cm for Ørnlia. Valle, Lærdal and Straumklumpen study areas all display systematic error.

The largest areas of error are concentrated at high elevations for Valle and Lærdal. There is also a diagonal pattern to the error in Valle. However, C2C distances for Valle and Lærdal are generally well below one meter with a mean distance of 37 cm. The Straumklumpen study area displays a more complicated error pattern. For most parts of Straumklumpen, the C2C distances are smaller than one meter and the overall mean distance is 60 cm. However, there are two areas of continuous larger distances (1.5-2 m), situated at the top of the model and at the middle left margin. Because of the large georeferencing errors in these areas, they were excluded in the discontinuity analysis.

5.3 Digital Mapping of Discontinuities

Discontinuity surfaces were mapped on the validated 3D models, using the Maptek PointStudio software, as described in section 4.4.1. The rock slopes of Lærdal and Straumklumpen 3D models were not mapped in their entirety, due to vast amounts of data and the corresponding workload for controlling its quality. Observations indicate that the discontinuities of the slope sections that were mapped, appear to accurately represent the entirety of the slopes. The modelled rock slopes of the other study areas were mapped to their full extent.

It was observed that extraction of surfaces is biased towards slope parallel discontinuities, with poorer sampling of obliquely oriented sets. As long as a sufficient number of discontinuities are mapped for the concentration of poles to be visible in a stereonet, this is not a problem for defining sets or finding their mean orientations (section 4.4.2). However, preferential extraction of slope parallel discontinuities can create an unrealistic difference in sample size, which in turn can affect the reliability of the spacing and persistence estimates (section 4.4.3).

5.3.1 Tunhovd

Three joint sets, that are roughly perpendicular to each other, were identified on the S-SW facing steep rock face of Tunhovd study area (figure 5.2 and 5.3). The rock consists of quartzite and appears blocky, with discontinuities present throughout the slope. The most dominant set (J1) is parallel to the slope, with a mean orientation of 82/188 (table 5.6). Based on the PointStudio analysis J1 has the smallest spacing and is the most persistent out of the three sets. J1 is intersected by set J2 that dips with 55º towards the east and set J3 that dips with 50º towards the west. J3 appears more prominent in the western part of the rock slope, which is SW facing and thereby semi-parallel to J3.

Most joints appear very systematic, in well-defined sets and there are few randomly oriented discontinuities present. Surfaces are generally smooth, especially for sets J1 and J3. The character of the joints in combination with a relatively high-resolution 3D model, made the mapping and interpretation straight forward and in addition it generated a good level of confidence in the orientation results. The discontinuity orientation, spacing and persistence defines elongated rectangular blocks. This shape is consistent with observations of blocks in the 3D model.

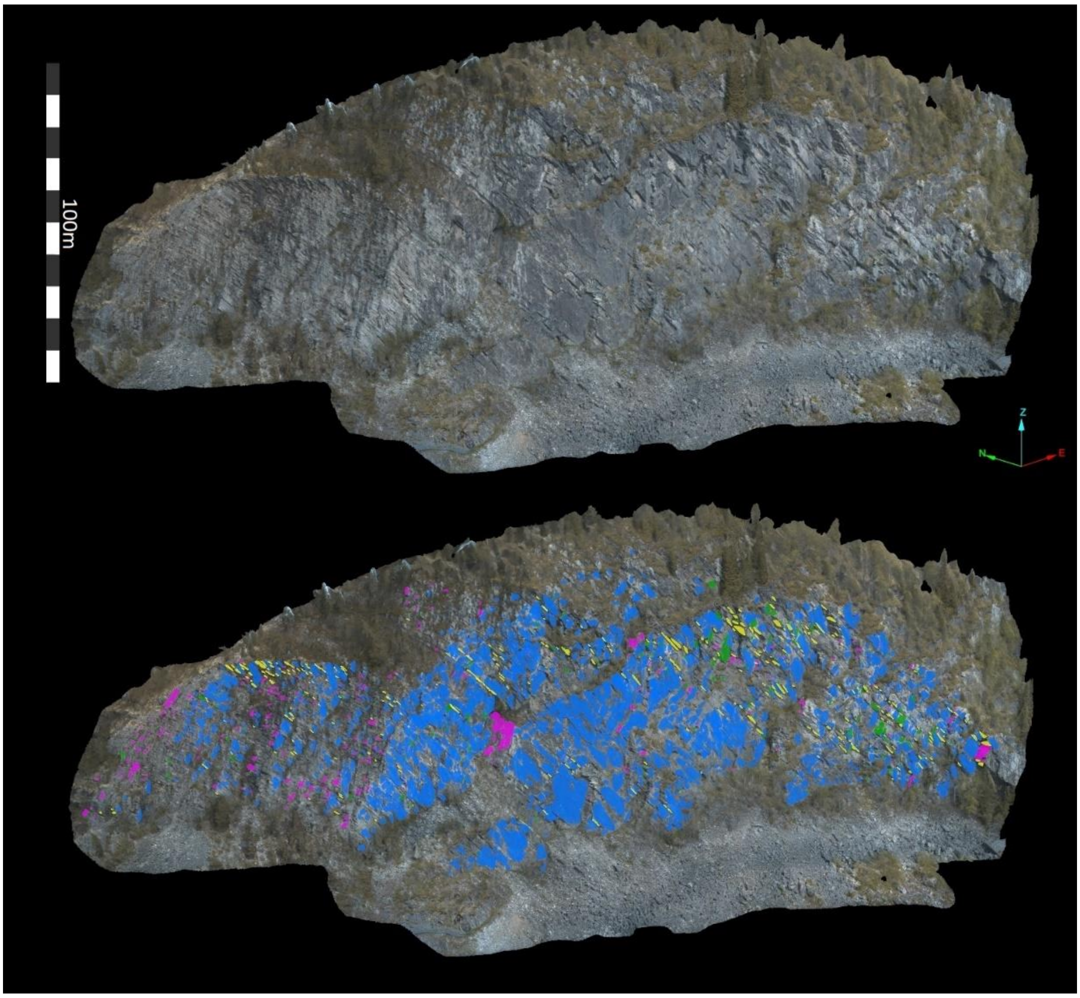

Figure 5.2 Top) Photogrammetric 3D mesh model for Tunhovd survey area. Bottom) Mapped discontinuity surfaces are displayed on the model, and colour coded according to what joint set they belong to. Green represents randomly oriented discontinuities.

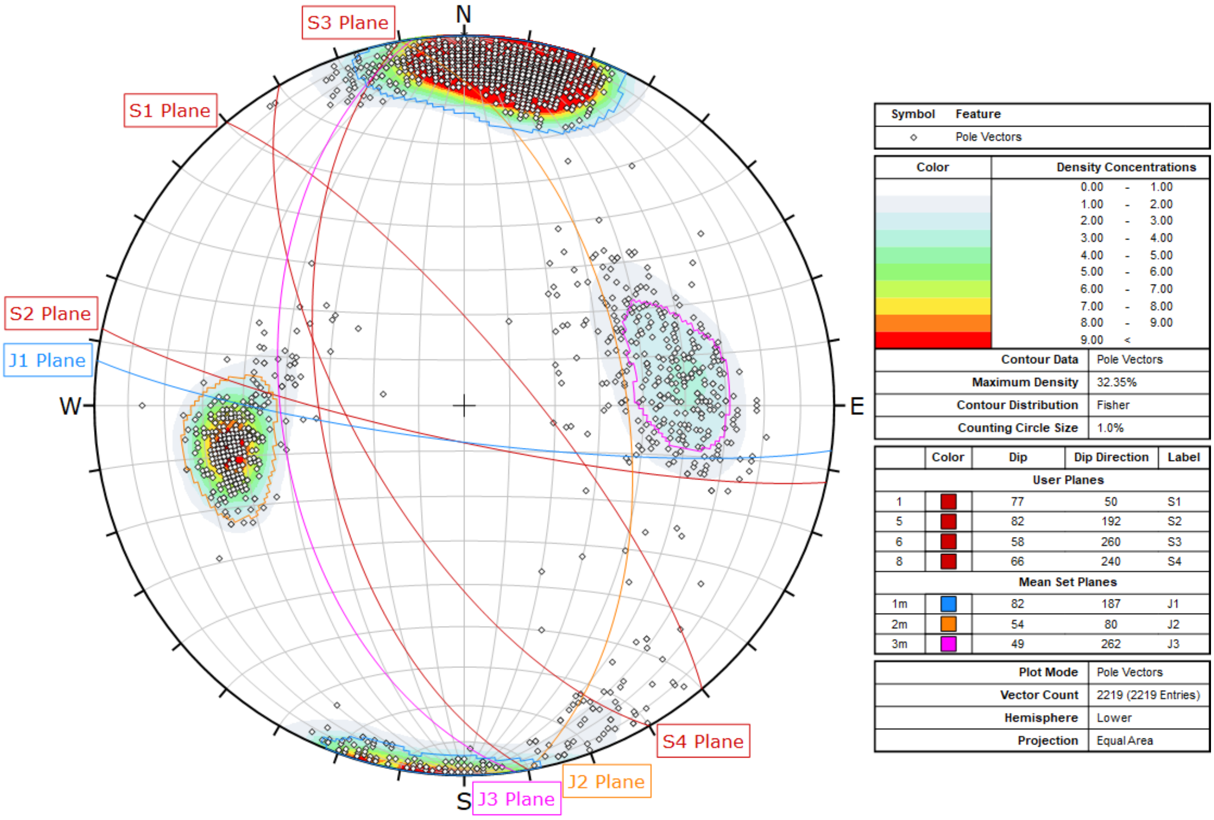

Figure 5.3 Mapped discontinuities for Tunhovd study area are represented by poles (points) in the stereonet. The density concentrations of the poles are visualized with a graded colour scale and was used to identify discontinuity sets. The poles that form the identified sets (J1, J2 and J3) are encircled. The mean planes of the discontinuity sets, and the planes of the identified slope sections (S1, S2, S3 and S4) are plotted as great circles (lines).

Table 5.6 Discontinuity set properties for Tunhovd survey area.

Discontinuity Set [colour]	Number of measurements	Mean Orientation [dip/dip direction/ strike]	Spacing[1] [m]	Persistence [m]	Max Asperity Amplitude (Profile Length)	JRC
J1 (Blue)	1441	82/188/098	M 0.25, R 0.15-4.89, SD 0.25	M 3.22, R 0.44-22.2, SD 2.30	156 mm (10.1 m)	7
J2 (Yellow/Orange)	325	55/080/350	M 0.85, R 0.15-7.93, SD 1.08	M 2.25, R 0.38-12.6, SD 1.41	71 mm (3.6 m)	10
J3 (Pink)	157	50/263/173	M 1.35, R 0.16-10.9, SD 2.31	M 1.77, R 0.42-8.36, SD 1.18	62 mm (4.5 m)	7

[1] The minimum spacing was set to 15 cm. * M – mean, R – range, SD – standard deviation, JRC – Joint Roughness Coefficient.

5.3.2 Valle

Three joint sets were identified on the SE facing rock slope of Valle study area (figure 5.4. and 5.5). The rock consists of massive, good quality granite with relatively few discontinuities. The dominant joint set (J1) is slope parallel, with a mean orientation of 44/124 (table 5.7). J1 defines the basal surface of exfoliation sheets. J2 is a vertical joint set that strikes nearly parallel to the slope and defines the rear release surface of the forming rock blocks. The discontinuities of J2 often appear as curved surfaces. This posed a challenge when discontinuities are mapped as planar surfaces, and each curved discontinuity had to be represented by two or more planes to capture the main orientations.

The third joint set (J3) is roughly perpendicular to the slope and the other two sets, with a mean orientation of 75/047. J3 appears infrequently and its sample size only amounts to 40 planes. The small sample size is mostly due to there being relatively few of these joints, and partly due to the exposed surfaces being too small to be accurately mapped at the model resolution, i.e. some underestimation. The spacing and persistence values defines sheet-like or tabular blocks, where J1 appear closely spaced and more persistent than the other sets. This shape is consistent with observations of blocks in the 3D model.

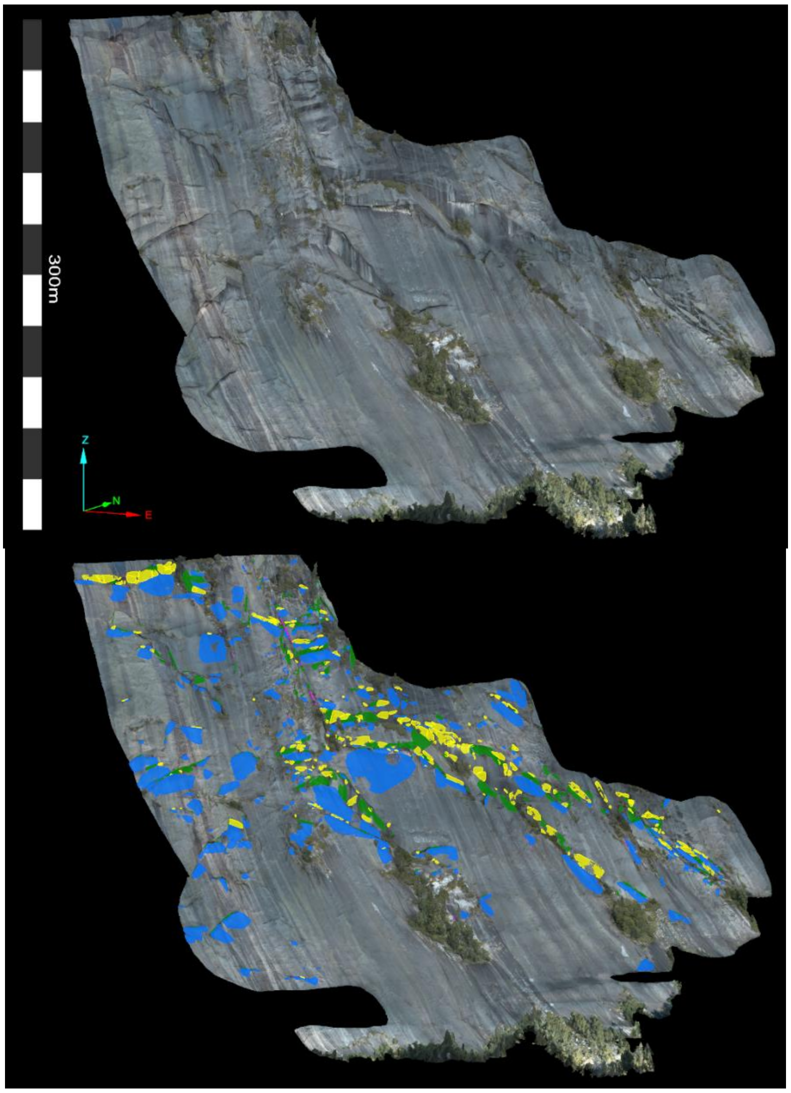

Figure 5.4 Top) Photogrammetric 3D mesh model for Valle survey area. Bottom) Mapped discontinuity surfaces are displayed on the model, and colour coded according to what joint set they belong to. Green represents randomly oriented discontinuities.

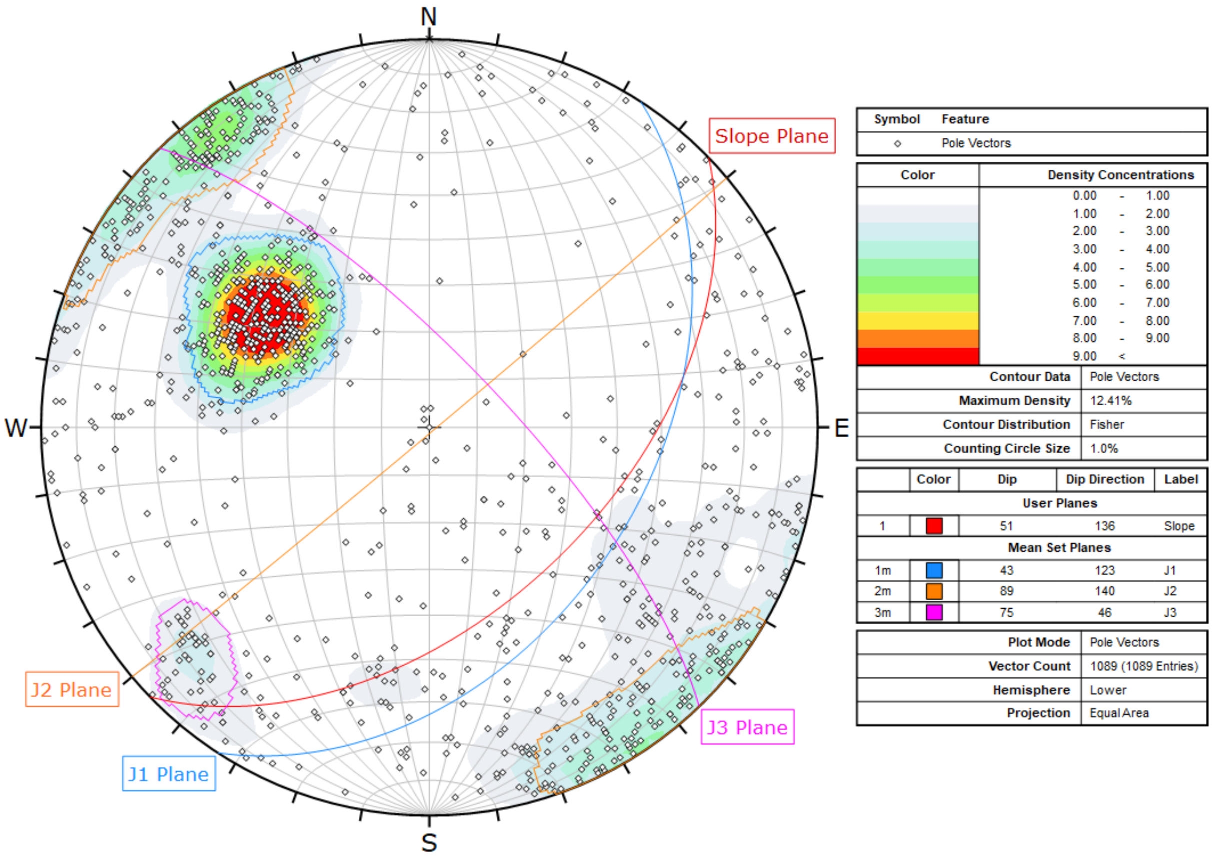

Figure 5.5 Mapped discontinuities for Valle study area are represented by poles (points) in the stereonet. The density concentrations of the poles are visualized with a graded colour scale and was used to identify discontinuity sets. The poles that form the identified sets (J1, J2 and J3) are encircled. The mean planes of the discontinuity sets, and the slope plane are plotted as great circles (lines).

Table 5.7 Discontinuity set properties for Valle survey area.

Discontinuity Set [colour]	Number of measurements	Mean Orientation [dip/dip direction/ strike]	Spacing[1] [m]	Persistence [m]	Max Asperity Amplitude (Profile Length)	JRC
J1 (Blue)	344	44/124/034	M 0.34, R 0.15-1.84, SD 0.22	M 6.78, R 0.53-54.4, SD 6.84	104 mm (4.4 m)	11
J2 (Yellow/Orange)	253	90/141/051	M 0.63, R 0.15-19.8, SD 1.25	M 4.61, R 0.58-23.1, SD 3.25	82 mm (4.0 m)	10
J3 (Pink)	40	75/047/317	M 6.17, R 0.16-41.6, SD 10.1	M 1.88, R 0.38-13.0, SD 2.24	25 mm (1.4 m)	8

[1] The minimum spacing was set to 15 cm. * M – mean, R – range, SD – standard deviation, JRC – Joint Roughness Coefficient.

5.3.3 Lærdal

Three joint sets were identified on the steep N-NE facing rock slope of Lærdal study area (figure 5.6 and 5.7). The rock consists of granite, which may locally be metamorphosed to augen gneiss. The slope has two main orientations. Discontinuities are present throughout the slope and does not appear regular. When plotted in a stereonet, the scattered poles of the mapped surfaces indicates that there are many randomly oriented discontinuities present. Low model quality can cause an increase of scatter in mapped surfaces, although it is unlikely to account for all the scatter observed here. The dominant joint set (J1) is semi-parallel to slope section 1, with a mean orientation of 70/024 (table 5.8). J2 dips with 76º towards the south-east. The intersection between J1 and J2 forms an angle of about 120º. Joint set (J3) has a mean orientation of 73/069.

A several meters thick band of broken rock can be seen cutting through the mapped section. The structure appears to be a normal fault. Bedrock surrounding faults can have fault related damages.

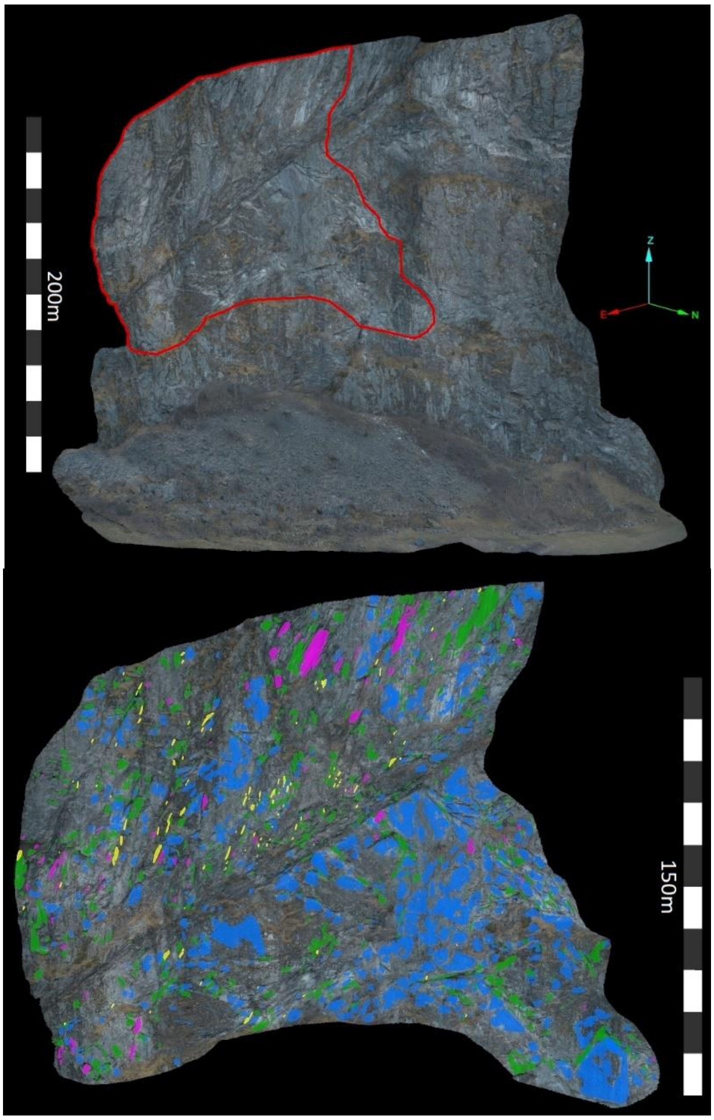

Figure 5.6 Top) Photogrammetric 3D mesh model for Lærdal survey area. The marked area was selected for digital mapping and constitutes 37 % of the modelled slope. Bottom) Mapped discontinuity surfaces are displayed on the chosen section of the model, and colour coded according to what joint set they belong to. Green represents randomly oriented discontinuities.

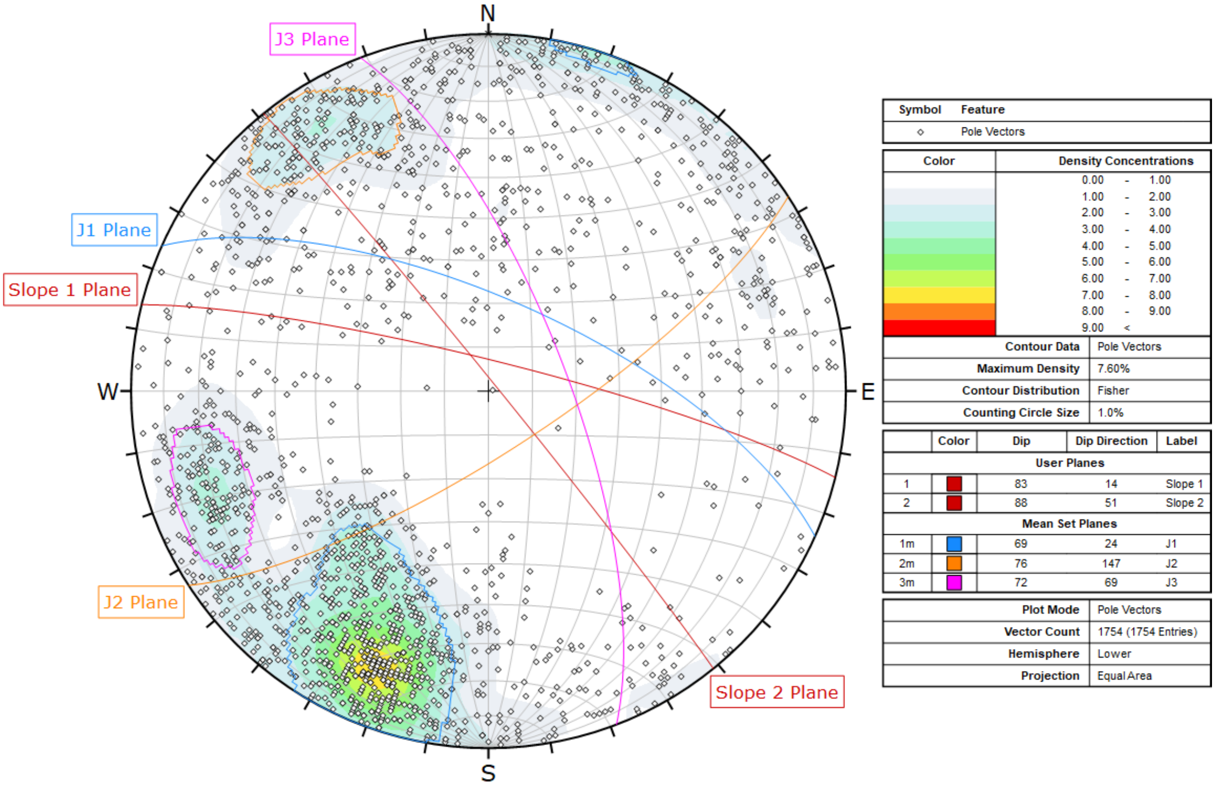

Figure 5.7 Mapped discontinuities for Lærdal study area are represented by poles (points) in the stereonet. The density concentrations of the poles are visualized with a graded colour scale and was used to identify discontinuity sets. The poles that form the identified sets (J1, J2 and J3) are encircled. The mean planes of the discontinuity sets, and the planes of the identified slope sections are plotted as great circles (lines).

Table 5.8 Discontinuity set properties for Lærdal survey area.

Discontinuity Set [colour]	Number of measurements	Mean Orientation [dip/dip direction/ strike]	Spacing[1] [m]	Persistence [m]	Max Asperity Amplitude (Profile Length)	JRC
J1 (Blue)	562	70/024/294	M 0.21, R 0.15-0.70, SD 0.07	M 3.50, R 0.48-27.4, SD 3.02	129 mm (7.4 m)	8
J2 (Yellow/Orange)	123	76/148/058	M 1.17, R 0.15-12.5, SD 1.68	M 1.85, R 0.49-7.41, SD 1.25	85 mm (3.6 m)	11
J3 (Pink)	107	73/069/339	M 1.73, R 0.15-14.6, SD 2.18	M 2.66, R 0.36-15.8, SD 2.44	80 mm (5.6 m)	7

[1] The minimum spacing was set to 15 cm. * M – mean, R – range, SD – standard deviation, JRC – Joint Roughness Coefficient.

5.3.4 Ørnlia

Three joint sets were identified on the west facing rock slope of Ørnlia study area (figure 5.8 and 5.9). The rock consists of massive, good quality granite/granitic gneiss with relatively few discontinuities. Ørnlia share some of the main traits for Valle study area, such as a gentle slope dip angle, how the joints are oriented relative to the slope and the presence of curved surfaces. The dominant joint set (J1) is slope parallel, with a mean orientation of 35/257 (table 5.9). J1 defines the basal surface of exfoliation sheets. J2 is vertical and striking NW-SE, and J3 dips with 66° towards the SE. With only 68 mapped planes, joint set J3 is the least prominent of the three sets. J2 and J3 form the lateral and rear release surfaces of rock blocks. Their orientations are oblique to the slope and defines a wedge with an angle that varies between 60-120°.

The spacing and persistence values defines sheet-like or tabular blocks, where J1 appear very closely spaced and more persistent than the other sets. The confidence in the accuracy of the results is high, because of the relatively high-resolution 3D model and the good correspondence between observations and analyzed characteristics.

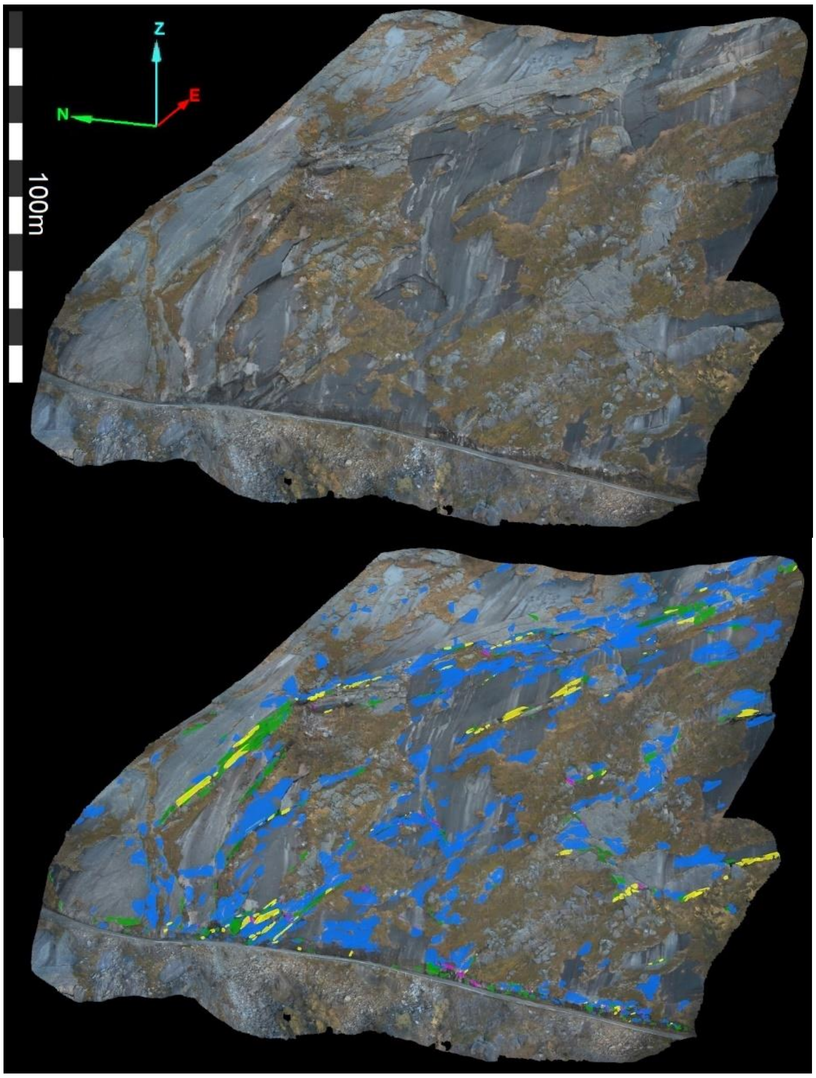

Figure 5.8 Top) Photogrammetric 3D mesh model for Ørnlia survey area. Bottom) Mapped discontinuity surfaces are displayed on the model, and colour coded according to what joint set they belong to. Green represents randomly oriented discontinuities.

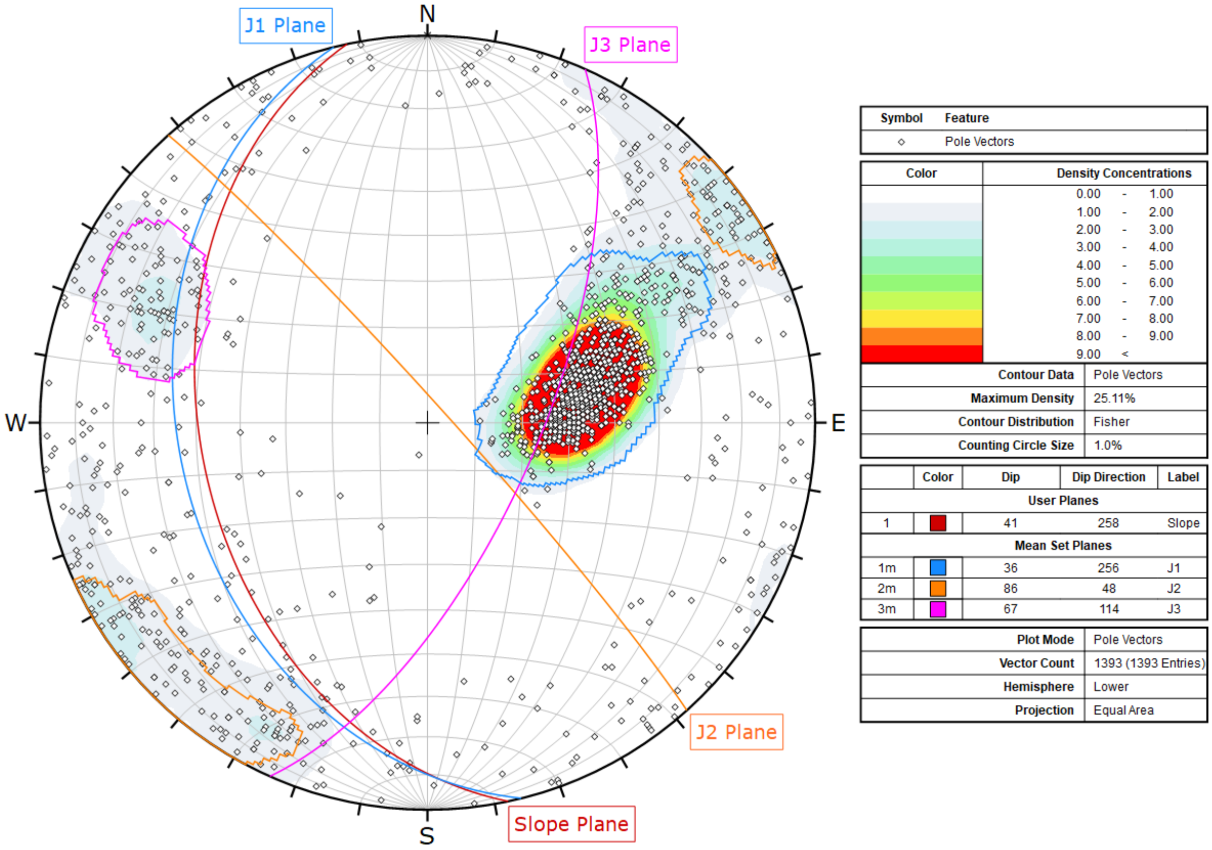

Symbol	Feature
◇	Pole Vectors

Color	Density Concentrations
	0.00 - 1.00
	1.00 - 2.00
	2.00 - 3.00
	3.00 - 4.00
	4.00 - 5.00
	5.00 - 6.00
	6.00 - 7.00
	7.00 - 8.00
	8.00 - 9.00
	9.00 <

Contour Data	Pole Vectors
Maximum Density	25.11%
Contour Distribution	Fisher
Counting Circle Size	1.0%

	Color	Dip	Dip Direction	Label
User Planes				
1	🟥	41	258	Slope
Mean Set Planes				
1m	🟦	36	256	J1
2m	🟧	86	48	J2
3m	🟪	67	114	J3

Plot Mode	Pole Vectors
Vector Count	1393 (1393 Entries)
Hemisphere	Lower
Projection	Equal Area

Figure 5.9 Mapped discontinuities for Ørnlia study area are represented by poles (points) in the stereonet. The density concentrations of the poles are visualized with a graded colour scale and was used to identify discontinuity sets. The poles that form the identified sets (J1, J2 and J3) are encircled. The mean planes of the discontinuity sets, and the slope plane are plotted as great circles (lines).

Table 5.9 Discontinuity set properties for Ørnlia survey area.

Discontinuity Set [colour]	Number of measurements	Mean Orientation [dip/dip direction/ strike]	Spacing[1] [m]	Persistence [m]	Max Asperity Amplitude (Profile Length)	JRC
J1 (Blue)	767	35/257/167	M 0.17, R 0.15-0.98, SD 0.06	M 3.99, R 0.43-31.0, SD 2.97	68 mm (5.2 m)	6
J2 (Yellow/Orange)	119	88/050/320	M 1.34, R 0.15-20.6, SD 2.48	M 3.03, R 0.39-18.0, SD 2.92	24 mm (1.4 m)	8
J3 (Pink)	68	66/114/024	M 2.88, R 0.17-16.6, SD 4.03	M 1.35, R 0.43-4.15, SD 0.80	28 mm (1.6 m)	8

[1] The minimum spacing was set to 15 cm. * M – mean, R – range, SD – standard deviation, JRC – Joint Roughness Coefficient.

5.3.5 Straumklumpen

Three joint sets were identified on the SW facing rock slopes of Straumklumpen (figure 5.10 and 5.11). The dominant joint set (J1) is slope parallel, with a mean orientation of 38/217 (table 5.10). J1 defines the basal surface of exfoliation sheets. J2 is a vertical joint set that strikes W-E and defines the rear release surface of the forming rock blocks. Joint set J3 dips with 69º towards the SSE and forms an angle of approximately 60º to the slope. J3 defines the lateral release surfaces, though the mapped discontinuities only amount to 69 planes. There is an additional small, contoured area in the stereonet, which was not used to define a joint set because it represents too few poles.

The spacing and persistence values defines sheet-like or tabular blocks, where J1 appear very closely spaced and more persistent than the other sets. There is a high level of correspondence between observations and analyzed characteristics. However, the digital mapping results of Straumklumpen are potentially the least accurate of the studied areas. This is due to a much larger spatial coverage of the 3D model, a relatively low portion of the model slope being mapped (12 %), and the model being the one with the lowest quality.

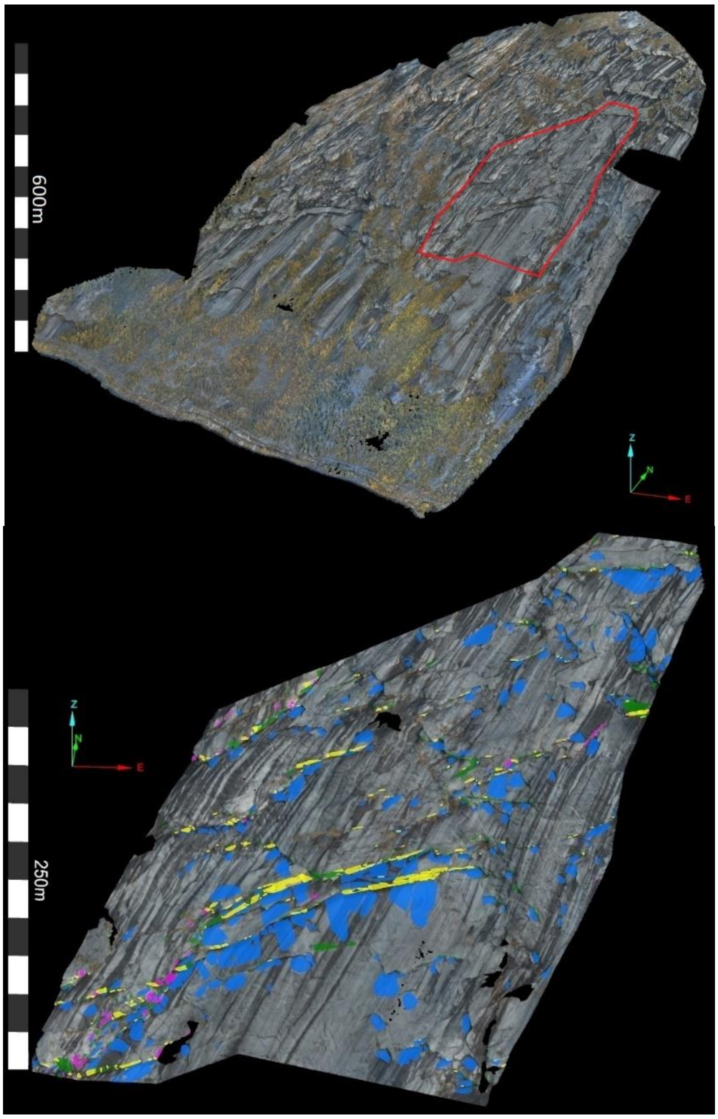

Figure 5.10 Top) Photogrammetric 3D mesh model for Straumklumpen survey area. The marked area was selected for digital mapping and constitutes 12 % of the model slope. Bottom) Mapped discontinuity surfaces are displayed on the chosen section of the model, and colour coded according to what joint set they belong to. Green represents randomly oriented discontinuities.

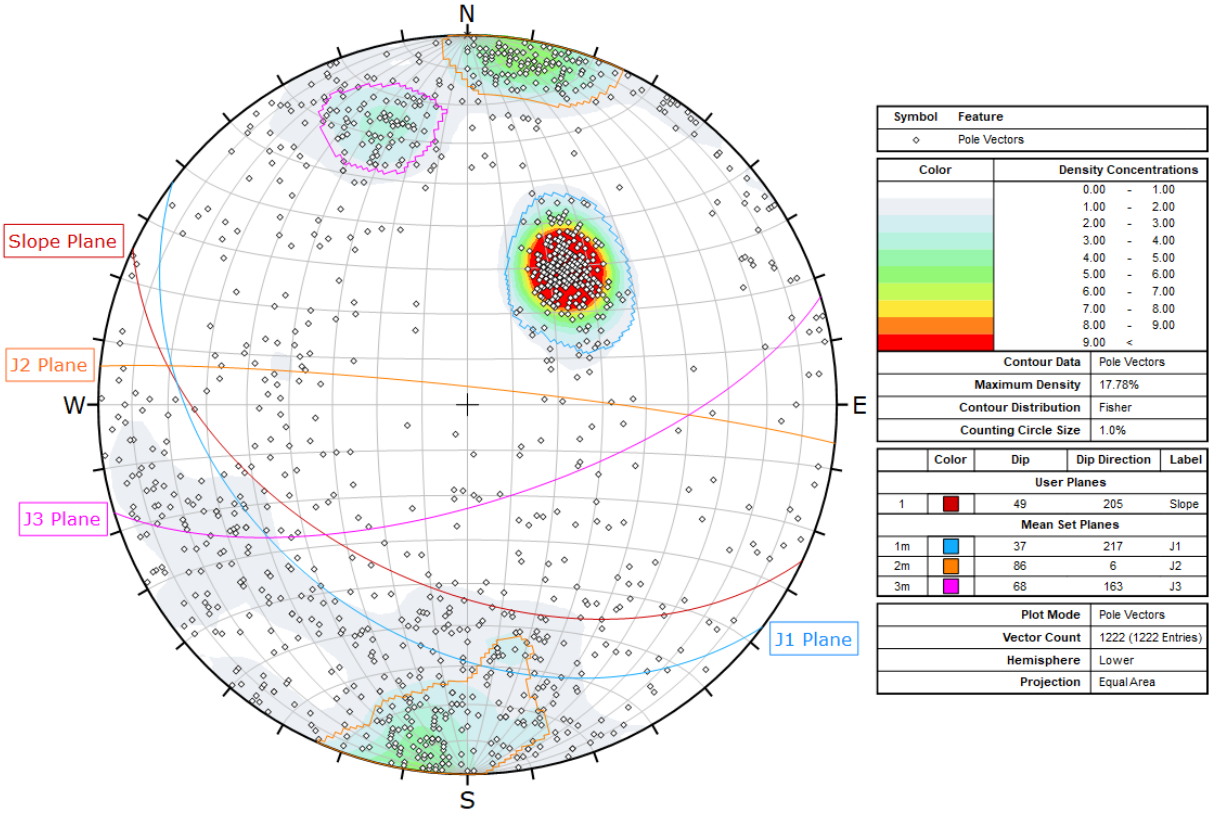

Figure 5.11 Mapped discontinuities for Straumklumpen study area are represented by poles (points) in the stereonet. The density concentrations of the poles are visualized with a graded colour scale and was used to identify discontinuity sets. The poles that form the identified sets (J1, J2 and J3) are encircled. The mean planes of the discontinuity sets, and the slope plane are plotted as great circles (lines).

Table 5.10 Discontinuity set properties for Straumklumpen survey area.

Discontinuity Set [colour]	Number of measurements	Mean Orientation [dip/dip direction/ strike]	Spacing[1] [m]	Persistence [m]	Max Asperity Amplitude (Profile Length)	JRC
J1 (Blue)	304	38/217/127	M 0.25, R 0.15-2.67, SD 0.18	M 7.65, R 0.76-37.5, SD 5.87	74 mm (6.6 m)	5.5
J2 (Yellow/Orange)	269	85/006/276	M 1.23, R 0.15-16.4, SD 2.10	M 3.53, R 0.58-26.9, SD 3.31	75 mm (3.3 m)	11
J3 (Pink)	69	69/163/073	M 3.94, R 0.15-33.9, SD 6.4	M 2.84, R 0.50-10.4, SD 1.76	79 mm (3.3 m)	11

[1] The minimum spacing was set to 15 cm. * M – mean, R – range, SD – standard deviation, JRC – Joint Roughness Coefficient.

5.4 Kinematic Analysis and Failure Modes

Kinematic analyses were performed on the digitally mapped discontinuities, to identify possible failure modes in the study areas. The analyses were done using the Dips software by Rocscience (section 4.4.2). For those study areas with little variation in the slope dip direction, it was sufficient to perform the analyses only on one slope orientation, representing the steepest section of the slope. This was the case in Valle, Ørnlia and Straumklumpen study areas. Due to the varied topography at Lærdal and Tunhovd study areas, the kinematic analyses were performed for two and four slope orientations, respectively.

5.4.1 Tunhovd

A total of 2219 discontinuity measurements were mapped for the Tunhovd study area and included in the kinematic analyses. The friction angle was set to 27º and lateral limits to 20º. Stereonets containing the kinematic analysis results for planar sliding, wedge sliding, flexural toppling and direct toppling are presented in figures 5.12-5.15. The included plots show the results for the slope orientation that yielded the highest potential for each individual failure mode. The orientations (dip/dip direction) of the four main slope sections are: 77/050 (S1), 82/192 (S2), 58/260 (S3) and 66/240 (S4).

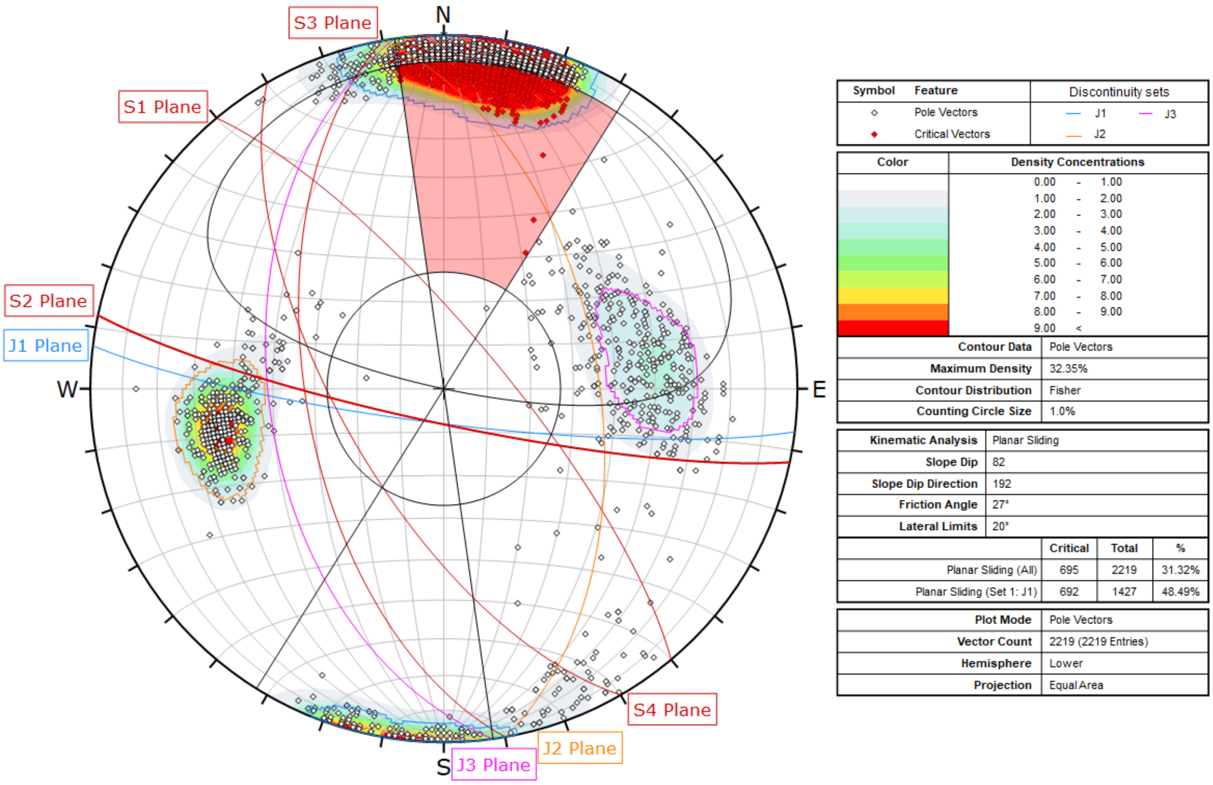

Symbol	Feature	Discontinuity sets
◇	Pole Vectors	— J1 — J3
◆	Critical Vectors	— J2

Color	Density Concentrations
⬜	0.00 - 1.00
⬜	1.00 - 2.00
⬜	2.00 - 3.00
🟩	3.00 - 4.00
🟩	4.00 - 5.00
🟩	5.00 - 6.00
🟨	6.00 - 7.00
🟨	7.00 - 8.00
🟧	8.00 - 9.00
🟥	9.00 <

Contour Data	Pole Vectors
Maximum Density	32.35%
Contour Distribution	Fisher
Counting Circle Size	1.0%

Kinematic Analysis	Planar Sliding
Slope Dip	82
Slope Dip Direction	192
Friction Angle	27°
Lateral Limits	20°

	Critical	Total	%
Planar Sliding (All)	695	2219	31.32%
Planar Sliding (Set 1: J1)	692	1427	48.49%

Plot Mode	Pole Vectors
Vector Count	2219 (2219 Entries)
Hemisphere	Lower
Projection	Equal Area

Figure 5.12 Kinematic analysis for planar sliding in slope section 2, at Tunhovd study area. Mapped discontinuities are represented by poles (points) in the stereonet. Poles located within the critical zone (red shaded area) represent potential basal sliding surfaces.

The kinematic analysis show that planar sliding is a likely failure mechanism in slope section 2, with 31.32 % of all measurements plotting within the critical zone (figure 5.12). Almost all the critical discontinuities belong to joint set J1, which would act as a steep basal sliding plane of failing blocks. The release surfaces are defined by J2 and J3.

The kinematic analyses of the other slope sections showed that there is also potential for planar sliding along J3, but it is unlikely for J2 to act as a basal sliding plane.

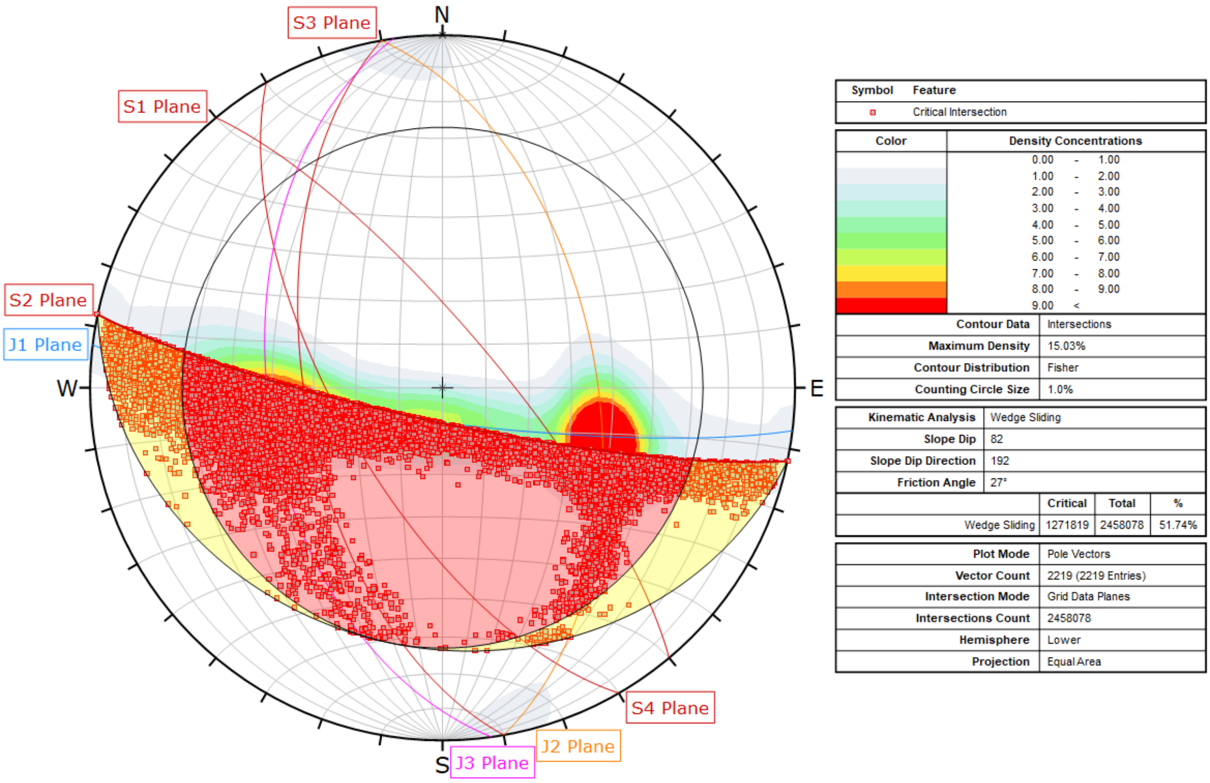

Figure 5.13 Kinematic analysis for wedge sliding in slope section 2, at Tunhovd study area. Intersections between mapped discontinuities are contoured, and visible as points when they are located within the critical zones (red/yellow shaded areas). Discontinuities with critical intersections represent the basal planes of potential wedge failures.

Wedge sliding presents as a very likely failure mechanism, with 51.74 % of all discontinuity intersections plotting within the critical zones for slope section 2 (figure 5.13). Two possible combinations of joint sets can form critical wedges, J1+J2 and J1+J3. The intersections of the two combinations plot in both the primary and the secondary critical zones (red and yellow shaded areas). This means that in some cases sliding occurs along both discontinuity planes, and in other cases sliding only occur along J1, which is semi-parallel to the slope.

The kinematic analyses of the other slope sections showed that wedge sliding is a likely failure mechanism in the entire slope since all sections had over 25 % of the discontinuity intersections plotted within the critical zones. The analysis also showed that a combination of J2 and J3 could form wedges in the other slope sections.

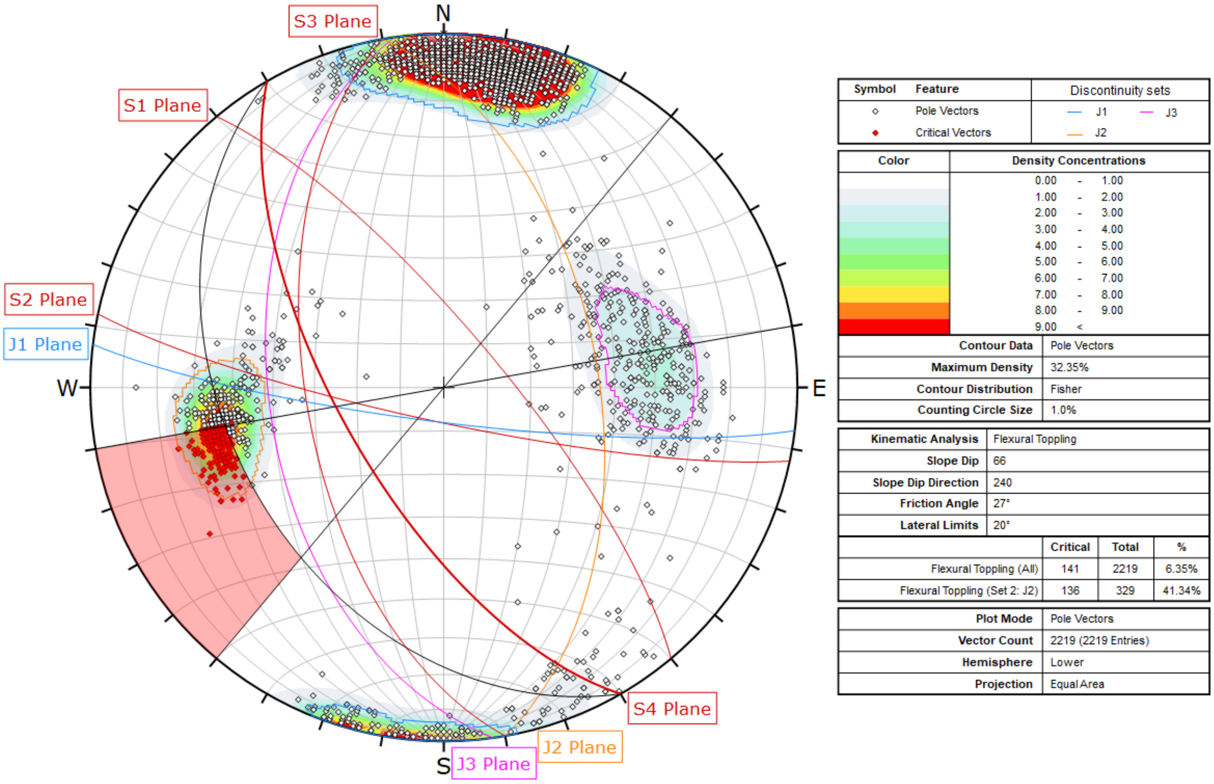

Symbol	Feature	Discontinuity sets
◇	Pole Vectors	— J1 — J3
◆	Critical Vectors	— J2

Color	Density Concentrations
⬜	0.00 - 1.00
⬜	1.00 - 2.00
🟦	2.00 - 3.00
🟦	3.00 - 4.00
🟩	4.00 - 5.00
🟩	5.00 - 6.00
🟨	6.00 - 7.00
🟨	7.00 - 8.00
🟧	8.00 - 9.00
🟥	9.00 <

Contour Data	Pole Vectors
Maximum Density	32.35%
Contour Distribution	Fisher
Counting Circle Size	1.0%

Kinematic Analysis	Flexural Toppling
Slope Dip	66
Slope Dip Direction	240
Friction Angle	27°
Lateral Limits	20°

	Critical	Total	%
Flexural Toppling (All)	141	2219	6.35%
Flexural Toppling (Set 2: J2)	136	329	41.34%

Plot Mode	Pole Vectors
Vector Count	2219 (2219 Entries)
Hemisphere	Lower
Projection	Equal Area

Figure 5.14 Kinematic analysis for flexural toppling in slope section 4, at Tunhovd study area. Mapped discontinuities are represented by poles (points) in the stereonet. Poles located within the critical zone (red shaded area) represent the potential slip surface between blocks.

The kinematic analysis indicates that flexural toppling is a possible failure mechanism in slope section 4, with 6.35 % of all measurements plotting within the critical zone (figure 5.14). Almost all the critical discontinuities belong to joint set J2.

The kinematic analyses of the other slope sections indicate that flexural toppling is an unlikely failure mechanism in those parts of the slope.

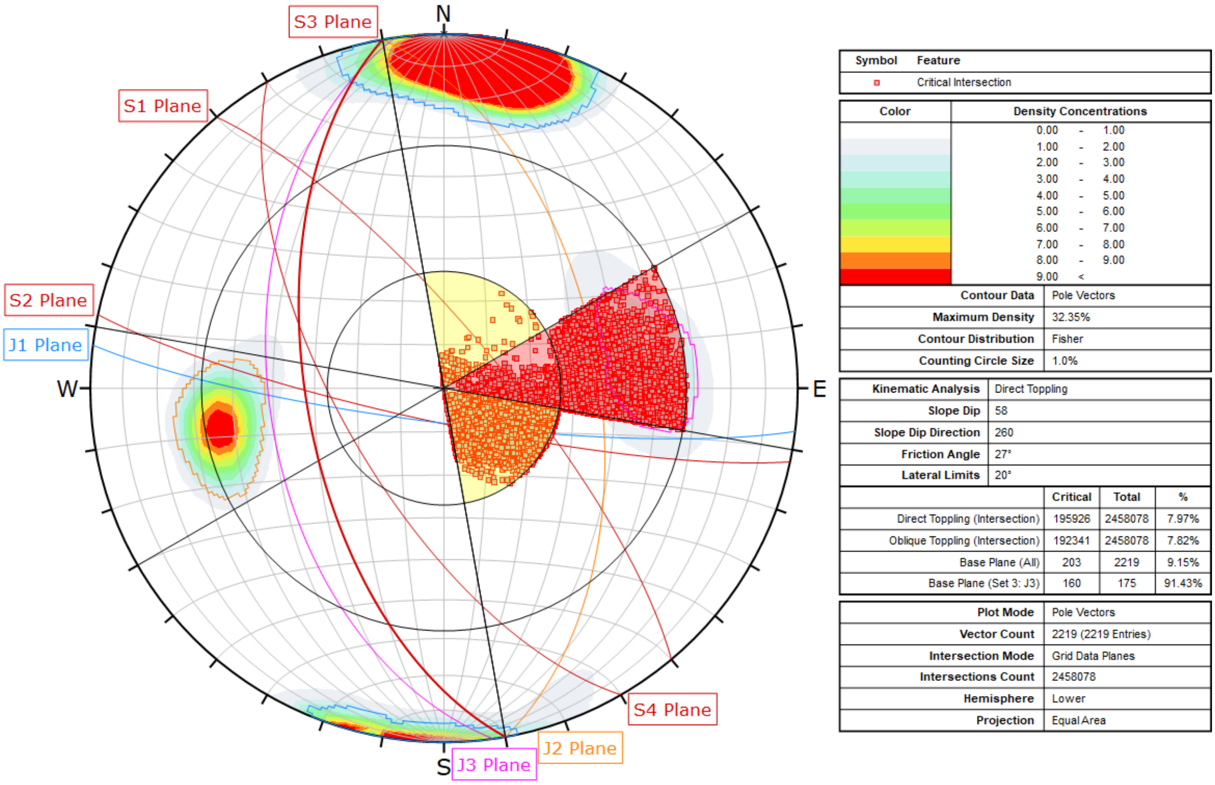

Symbol	Feature
▫	Critical Intersection

Color	Density Concentrations
⬜	0.00 - 1.00
⬜	1.00 - 2.00
🟦	2.00 - 3.00
🟩	3.00 - 4.00
🟩	4.00 - 5.00
🟩	5.00 - 6.00
🟨	6.00 - 7.00
🟨	7.00 - 8.00
🟧	8.00 - 9.00
🟥	9.00 <

Contour Data	Pole Vectors
Maximum Density	32.35%
Contour Distribution	Fisher
Counting Circle Size	1.0%

Kinematic Analysis	Direct Toppling
Slope Dip	58
Slope Dip Direction	260
Friction Angle	27°
Lateral Limits	20°

	Critical	**Total**	**%**
Direct Toppling (Intersection)	195926	2458078	7.97%
Oblique Toppling (Intersection)	192341	2458078	7.82%
Base Plane (All)	203	2219	9.15%
Base Plane (Set 3: J3)	160	175	91.43%

Plot Mode	Pole Vectors
Vector Count	2219 (2219 Entries)
Intersection Mode	Grid Data Planes
Intersections Count	2458078
Hemisphere	Lower
Projection	Equal Area

Figure 5.15 Kinematic analysis for direct toppling in slope section 3, at Tunhovd study area. Mapped discontinuities are contoured in the stereonet. Discontinuity intersections are visible as points when they are located within the critical zones (red/yellow shaded areas). Critical poles represent the potential basal surfaces of toppling blocks, while the discontinuities with critical intersections represents the lateral and rear surfaces of those blocks.

The kinematic analysis indicates that direct and oblique toppling are potential failure mechanisms in slope section 3 (figure 5.15). Joint set J3 is likely to act as the basal plane of failing blocks, while J1 and J2 forms the lateral and rear release surfaces. Out of all discontinuity intersections, 7.97 % plot within the primary critical zone (red shaded area) that indicates direct toppling, and 7.82 % plot within the secondary critical zone (yellow shaded area) that indicates oblique toppling.

The kinematic analyses of the other slope sections indicate that direct and oblique toppling are possible failure mechanisms in the entire slope, but not very likely. However, it appears like the toppling potential in slope section 2 could be underestimated, when considering the observed bias (towards slope parallel orientations) during extraction of discontinuities.

Summary

In Tunhovd study area, the kinematic analyses suggest that the most likely failure mechanisms are planar and wedge sliding, with toppling being considerably less likely to occur. Slope observations indicate that toppling failure is much more common in Tunhovd than suggested by the kinematic analysis (figure 5.16), perhaps also the main mechanism (section 6.4). The observed blocks and columns appear to have traits of both flexural and direct toppling and could be classified as the transitional form called block-flexural toppling.

Figure 5.16 Examples of toppling blocks in Tunhovd study area, shown on the 3D mesh model. While the situation in the left figure resembles direct toppling, the situation in the right figure looks more like flexural toppling.

5.4.2 Valle

A total of 1089 discontinuity measurements were mapped for the Valle study area and included in the kinematic analyses. The friction angle was set to 30º and lateral limits to 20º. The analyzed slope section has an orientation of 51/136. Stereonets containing the kinematic analysis results for planar sliding, wedge sliding, flexural toppling and direct toppling are presented in figures 5.17-5.20.

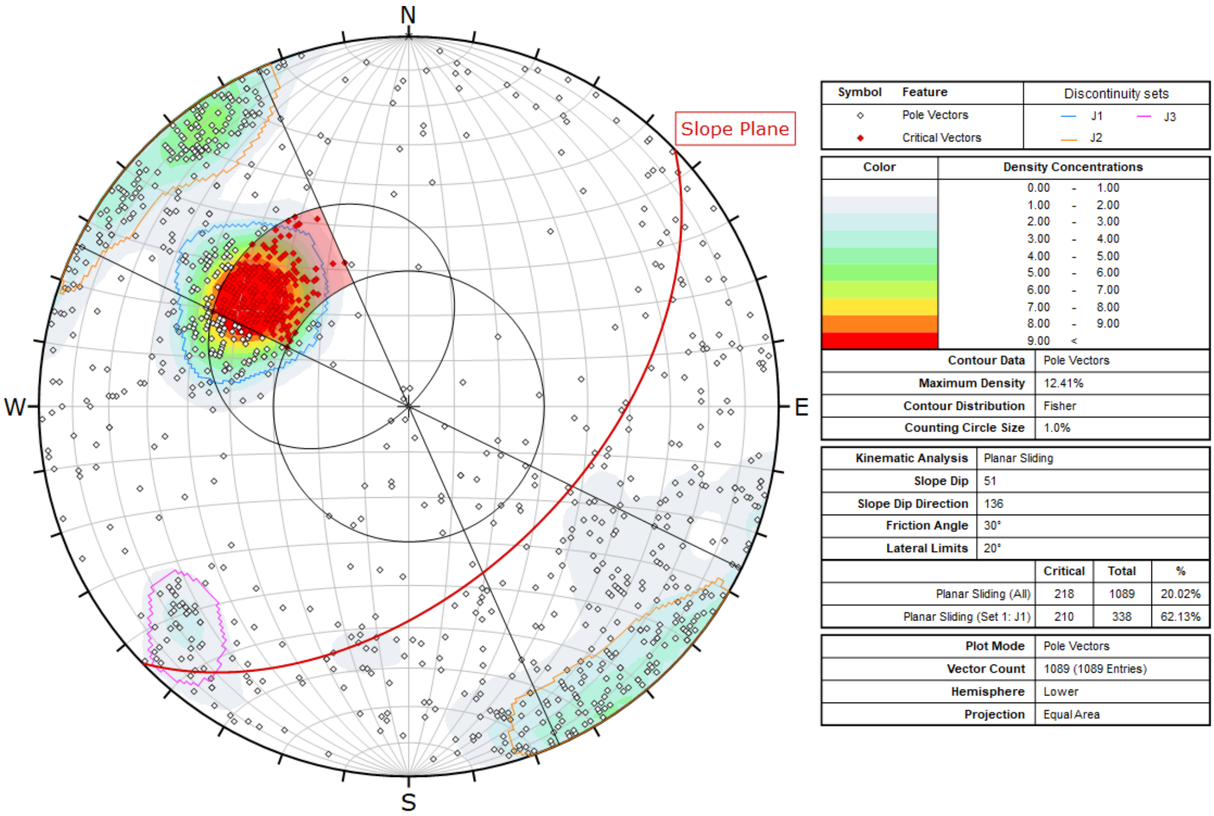

Symbol	Feature	Discontinuity sets
◇	Pole Vectors	— J1 — J3
◆	Critical Vectors	— J2

Color	Density Concentrations
⬜	0.00 - 1.00
⬜	1.00 - 2.00
🟦	2.00 - 3.00
🟩	3.00 - 4.00
🟩	4.00 - 5.00
🟩	5.00 - 6.00
🟨	6.00 - 7.00
🟨	7.00 - 8.00
🟧	8.00 - 9.00
🟥	9.00 <

Contour Data	Pole Vectors
Maximum Density	12.41%
Contour Distribution	Fisher
Counting Circle Size	1.0%

Kinematic Analysis	Planar Sliding
Slope Dip	51
Slope Dip Direction	136
Friction Angle	30°
Lateral Limits	20°

	Critical	Total	%
Planar Sliding (All)	218	1089	20.02%
Planar Sliding (Set 1: J1)	210	338	62.13%

Plot Mode	Pole Vectors
Vector Count	1089 (1089 Entries)
Hemisphere	Lower
Projection	Equal Area

Figure 5.17 Kinematic analysis for planar sliding at Valle study area. Mapped discontinuities are represented by poles (points) in the stereonet. Poles located within the critical zone (red shaded area) represent potential basal sliding surfaces.

The kinematic analysis show that planar sliding is a likely failure mechanism, with 20.02 % of all measurements plotting within the critical zone (figure 5.17). Almost all the critical discontinuities belong to joint set J1, which would act as the basal sliding plane of failing blocks. The rear release surface is defined by J2, and J3 could form the lateral release. Though the degree of scatter in the plot reveals that there are also many random discontinuities that could act as release surfaces.

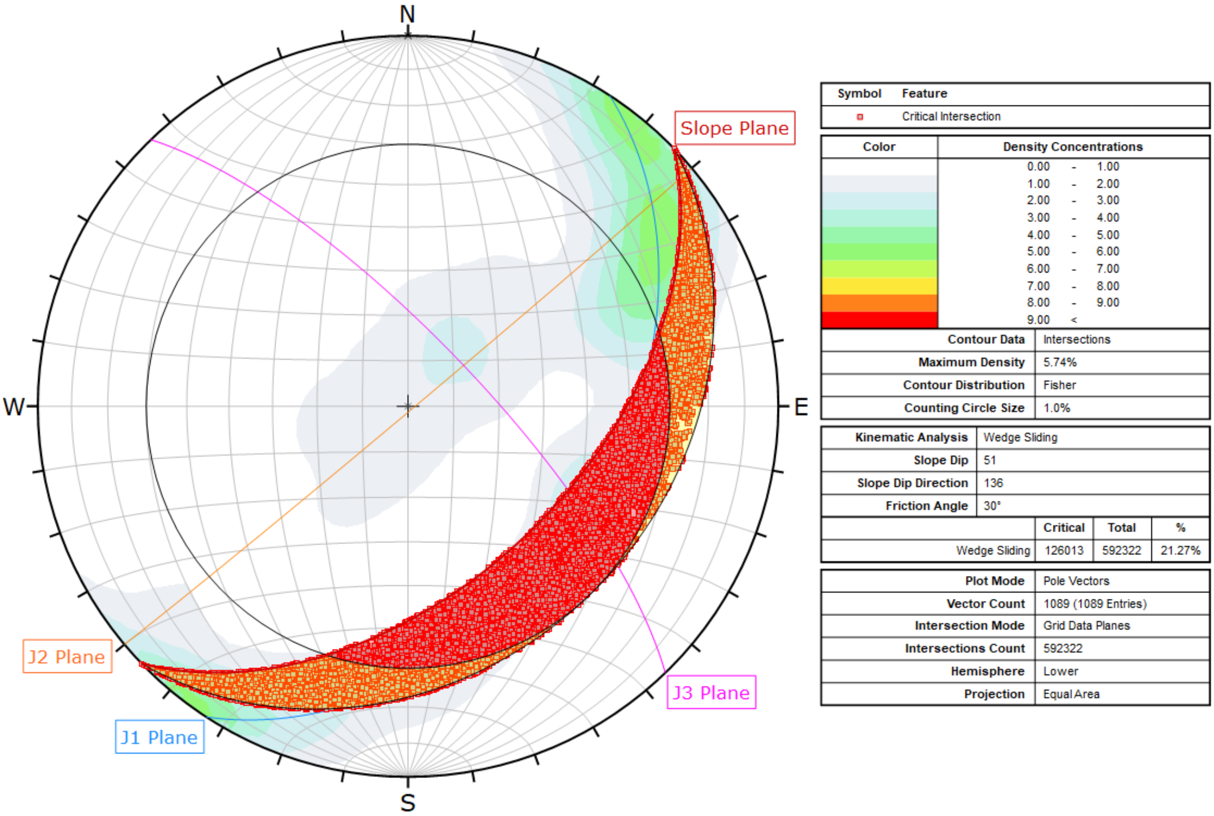

Symbol	Feature
🟥	Critical Intersection

Color	Density Concentrations
⬜	0.00 - 1.00
⬜	1.00 - 2.00
🟦	2.00 - 3.00
🟦	3.00 - 4.00
🟩	4.00 - 5.00
🟩	5.00 - 6.00
🟩	6.00 - 7.00
🟨	7.00 - 8.00
🟧	8.00 - 9.00
🟥	9.00 <

Contour Data	Intersections
Maximum Density	5.74%
Contour Distribution	Fisher
Counting Circle Size	1.0%

Kinematic Analysis	Wedge Sliding
Slope Dip	51
Slope Dip Direction	136
Friction Angle	30°

	Critical	**Total**	**%**
Wedge Sliding	126013	592322	21.27%

Plot Mode	Pole Vectors
Vector Count	1089 (1089 Entries)
Intersection Mode	Grid Data Planes
Intersections Count	592322
Hemisphere	Lower
Projection	Equal Area

Figure 5.18 Kinematic analysis for wedge sliding at Valle study area. Intersections between mapped discontinuities are contoured, and visible as points when they are located within the critical zones (red/yellow shaded areas). Discontinuities with critical intersections represent the basal planes of potential wedge failures.

Wedge sliding also presents as a likely failure mechanism, with 21.27 % of all discontinuity intersections plotting within the critical zones (figure 5.18). The joint sets J1 and J3 mainly intersects within the primary critical zone (red shaded area), which indicates that they could form the basal sliding surfaces of failing rock wedges. A combination of J1 and J2 could also produce wedges, but since the intersections plot within the secondary critical zone (yellow shaded area) the sliding would only be along J1, which is semi-parallel to the slope.

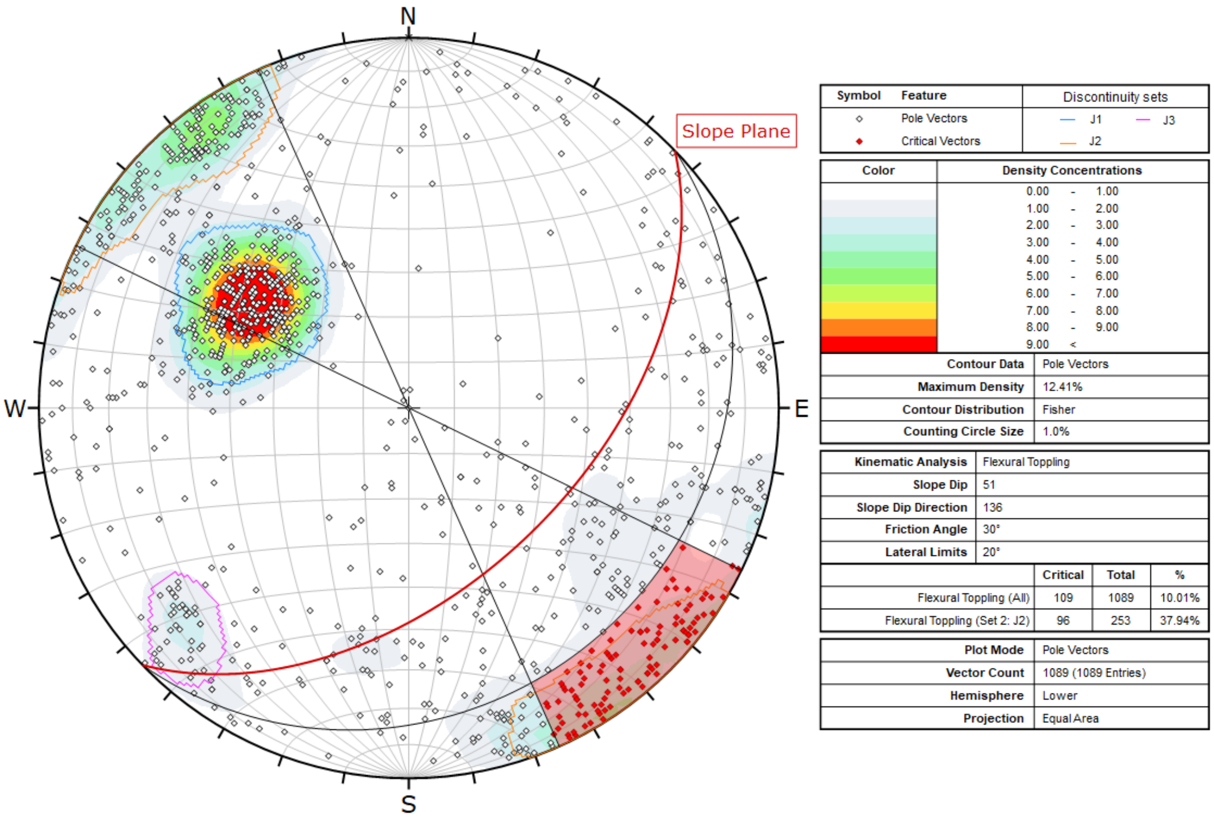

Symbol	Feature	Discontinuity sets
◇	Pole Vectors	— J1 — J3
◆	Critical Vectors	— J2

Color	Density Concentrations
⬜	0.00 - 1.00
⬜	1.00 - 2.00
⬜	2.00 - 3.00
🟩	3.00 - 4.00
🟩	4.00 - 5.00
🟩	5.00 - 6.00
🟨	6.00 - 7.00
🟨	7.00 - 8.00
🟧	8.00 - 9.00
🟥	9.00 <

Contour Data	Pole Vectors
Maximum Density	12.41%
Contour Distribution	Fisher
Counting Circle Size	1.0%

Kinematic Analysis	Flexural Toppling
Slope Dip	51
Slope Dip Direction	136
Friction Angle	30°
Lateral Limits	20°

	Critical	**Total**	**%**
Flexural Toppling (All)	109	1089	10.01%
Flexural Toppling (Set 2: J2)	96	253	37.94%

Plot Mode	Pole Vectors
Vector Count	1089 (1089 Entries)
Hemisphere	Lower
Projection	Equal Area

Figure 5.19 Kinematic analysis for flexural toppling at Valle study area. Mapped discontinuities are represented by poles (points) in the stereonet. Poles located within the critical zone (red shaded area) represent the potential slip surface between blocks.

The kinematic analysis indicates that flexural toppling is a possible failure mechanism, with 10.01 % of all measurements plotting within the critical zone (figure 5.19). Almost all the critical discontinuities belong to joint set J2, which would act as the steep slip surface between toppling rock columns.

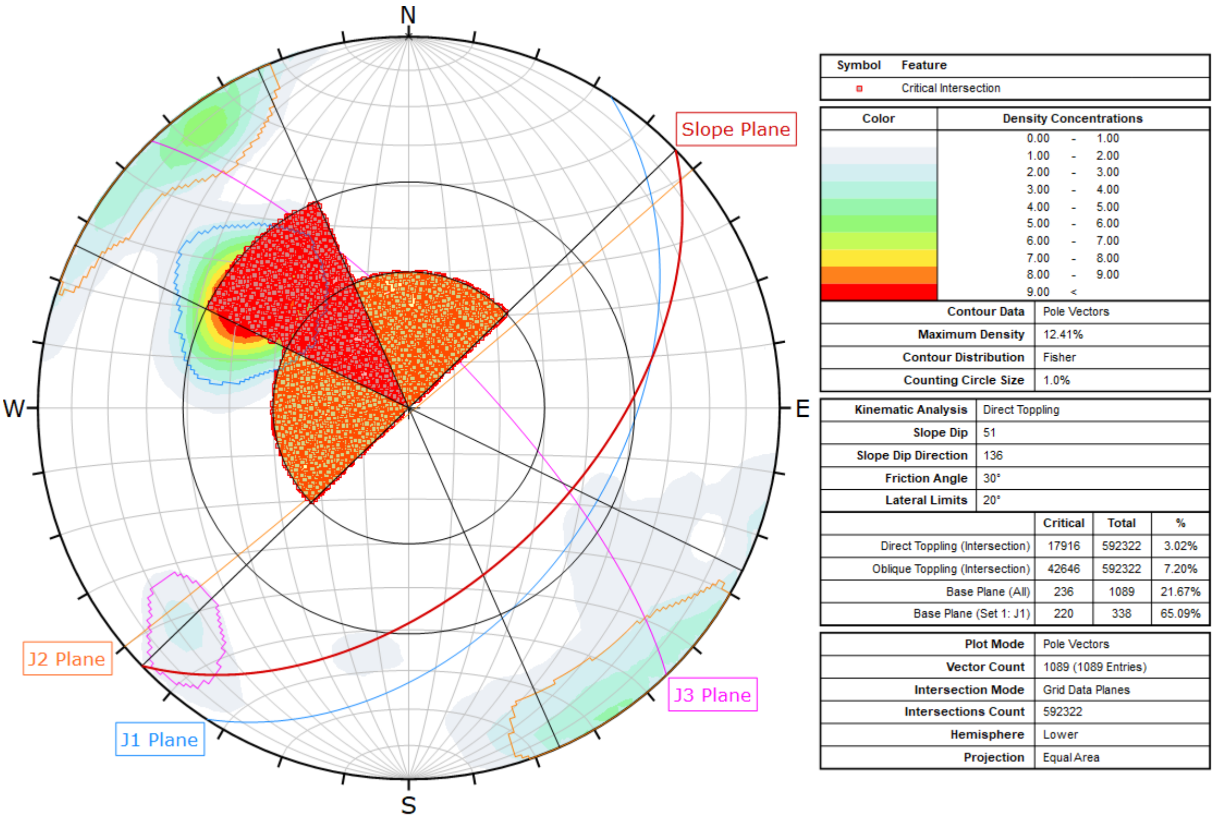

Symbol	Feature
▫	Critical Intersection

Color	Density Concentrations
⬜	0.00 - 1.00
⬜	1.00 - 2.00
🟦	2.00 - 3.00
🟦	3.00 - 4.00
🟩	4.00 - 5.00
🟩	5.00 - 6.00
🟩	6.00 - 7.00
🟨	7.00 - 8.00
🟧	8.00 - 9.00
🟥	9.00 <

Contour Data	Pole Vectors
Maximum Density	12.41%
Contour Distribution	Fisher
Counting Circle Size	1.0%

Kinematic Analysis	Direct Toppling
Slope Dip	51
Slope Dip Direction	136
Friction Angle	30°
Lateral Limits	20°

	Critical	**Total**	**%**
Direct Toppling (Intersection)	17916	592322	3.02%
Oblique Toppling (Intersection)	42646	592322	7.20%
Base Plane (All)	236	1089	21.67%
Base Plane (Set 1: J1)	220	338	65.09%

Plot Mode	Pole Vectors
Vector Count	1089 (1089 Entries)
Intersection Mode	Grid Data Planes
Intersections Count	592322
Hemisphere	Lower
Projection	Equal Area

Figure 5.20 Kinematic analysis for direct toppling at Valle study area. Mapped discontinuities are contoured in the stereonet. Discontinuity intersections are visible as points when they are located within the critical zones (red/yellow shaded areas). Critical poles represent the potential basal surfaces of toppling blocks, while the discontinuities with critical intersections represents the lateral and rear surfaces of those blocks.

The kinematic analysis indicates that direct toppling is possible, but that oblique toppling is more likely (figure 5.20). Joint set J1 is likely to act as a basal plane, while J2 and J3 could form the lateral and rear release surfaces of toppling blocks. Only 3.20 % of the intersections plot within the primary critical zone (red shaded area) that indicates direct toppling, and 7.20 % plot within the secondary critical zone (yellow shaded area) that indicates oblique toppling.

Summary

In Valle study area, the kinematic analyses suggest that the most likely failure mechanisms are planar and wedge sliding. Observations confirms that planar failure is common. But when it comes to wedges, they are observed to be truncated by a slope parallel plane at the base and the intersecting planes that form the wedges appear very steep (figure 5.21). This indicates that sliding occur mainly along the basal plane and that the failure mode is closer to planar sliding. The analyses also suggest that flexural and direct/oblique toppling are possible. But there are no observations supporting this, as blocks tend to form sheets rather than columns. Also, when considering that the rock slope consists of massive granite, it appears unlikely that blocks would break in flexure (section 2.2.4).

Figure 5.21 Example of a common joint configuration in Valle study area, shown on the 3D mesh model. The joints define a block with a slope parallel basal plane and wedge-shaped sides.

5.4.3 Lærdal

A total of 1754 discontinuity measurements were mapped for the Lærdal study area and included in the kinematic analyses. The friction angle was set to 30° and lateral limits to 20°. Slope section 1 has an orientation of 83/014 and section 2 has an orientation of 88/051. Stereonets containing the kinematic analysis results for planar sliding, wedge sliding, flexural toppling and direct toppling are presented in figures 5.22-5.25. The included plots show the results for the slope orientation that yielded the highest potential for each individual failure mode.

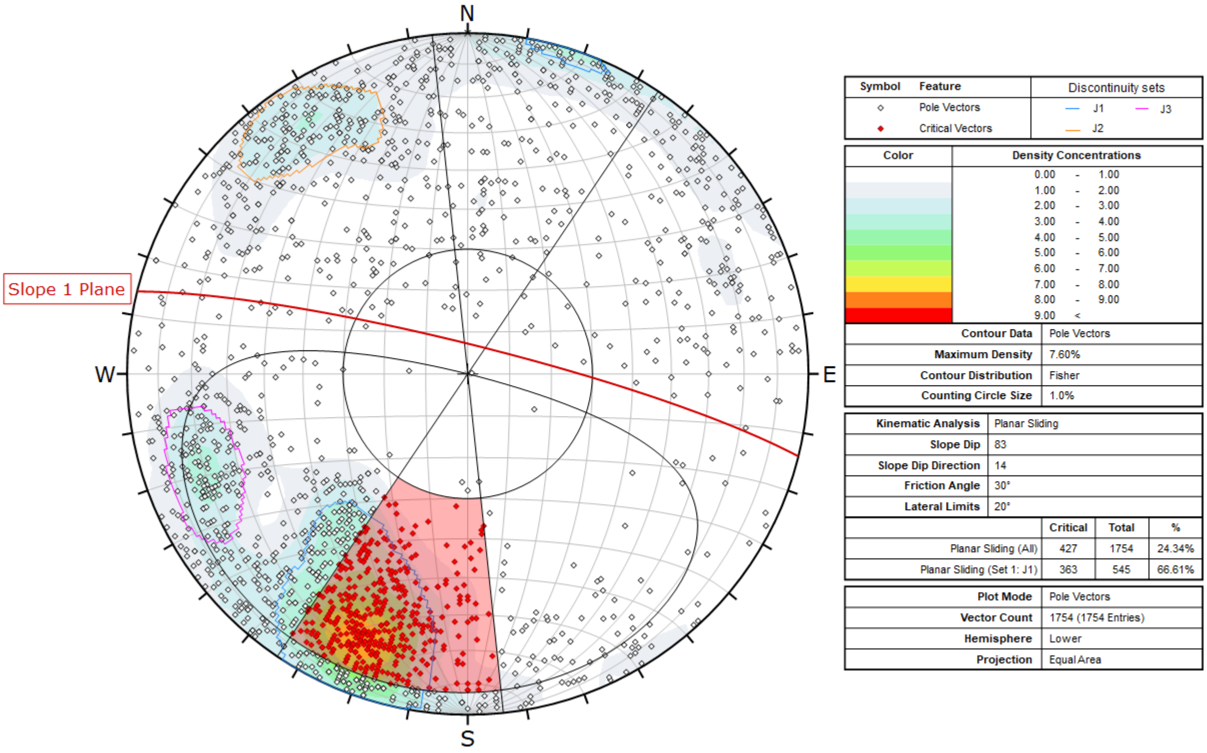

Figure 5.22 Kinematic analysis for planar sliding in slope section 1, at Lærdal study area. Mapped discontinuities are represented by poles (points) in the stereonet. Poles located within the critical zone (red shaded area) represent potential basal sliding surfaces.

The kinematic analysis show that planar sliding is a likely failure mechanism, with 24.34 % of all measurements plotting within the critical zone (figure 5.22). Many of the critical discontinuities belong to joint set J1, which would act as the basal sliding plane of failing blocks. The rear release surface could also be defined by J1, and either J2 or J3 could form the lateral release. Though the degree of scatter in the plot reveals that there are many random discontinuities that could act as release surfaces as well.

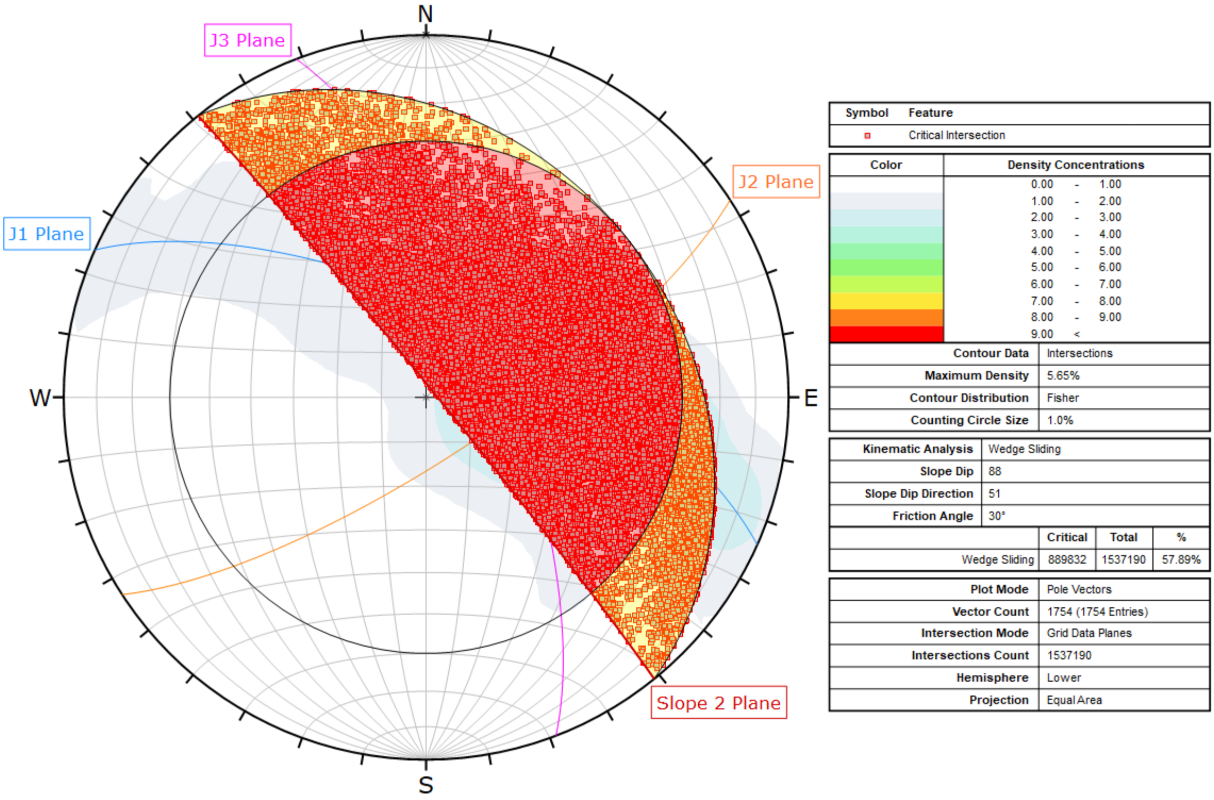

Symbol	Feature
🟥	Critical Intersection

Color	Density Concentrations
⬜	0.00 - 1.00
⬜	1.00 - 2.00
🟦	2.00 - 3.00
🟦	3.00 - 4.00
🟩	4.00 - 5.00
🟩	5.00 - 6.00
🟨	6.00 - 7.00
🟨	7.00 - 8.00
🟧	8.00 - 9.00
🟥	9.00 <

Contour Data	Intersections
Maximum Density	5.65%
Contour Distribution	Fisher
Counting Circle Size	1.0%

Kinematic Analysis	Wedge Sliding
Slope Dip	88
Slope Dip Direction	51
Friction Angle	30°

	Critical	Total	%
Wedge Sliding	889832	1537190	57.89%

Plot Mode	Pole Vectors
Vector Count	1754 (1754 Entries)
Intersection Mode	Grid Data Planes
Intersections Count	1537190
Hemisphere	Lower
Projection	Equal Area

Figure 5.23 Kinematic analysis for wedge sliding in slope section 2, at Lærdal study area. Intersections between mapped discontinuities are contoured, and visible as points when they are located within the critical zones (red/yellow shaded areas). Discontinuities with critical intersections represent the basal planes of potential wedge failures.

Wedge sliding presents as a very likely failure mechanism, with 57.89 % of all discontinuity intersections plotting within the critical zones (figure 5.23). All the possible joint set combinations (J1+J2, J1+J3 and J2+J3) mainly intersect within the primary critical zone (red shaded area), which indicates that either of the pairs could form the basal sliding surfaces of failing rock wedges.

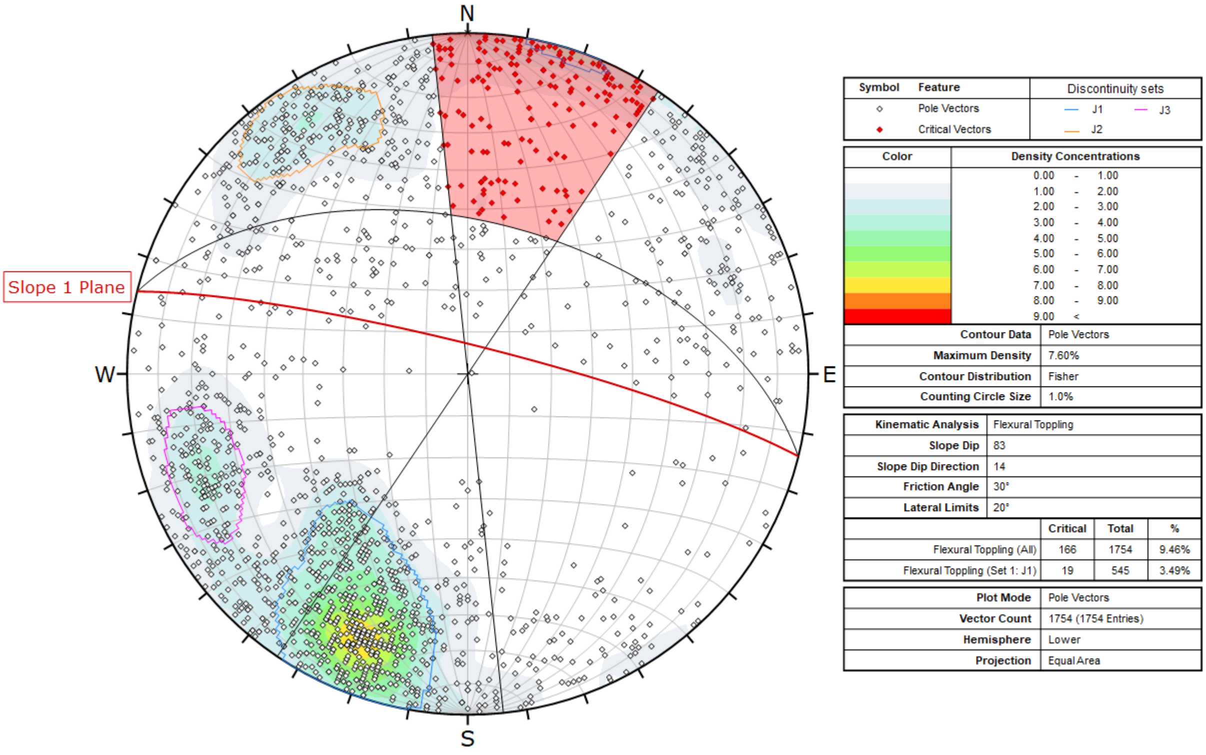

Symbol	Feature	Discontinuity sets
◇	Pole Vectors	— J1 — J3
◆	Critical Vectors	— J2

Color	Density Concentrations
⬜	0.00 - 1.00
⬜	1.00 - 2.00
⬜	2.00 - 3.00
🟩	3.00 - 4.00
🟩	4.00 - 5.00
🟩	5.00 - 6.00
🟨	6.00 - 7.00
🟨	7.00 - 8.00
🟧	8.00 - 9.00
🟥	9.00 <

Contour Data	Pole Vectors
Maximum Density	7.60%
Contour Distribution	Fisher
Counting Circle Size	1.0%

Kinematic Analysis	Flexural Toppling
Slope Dip	83
Slope Dip Direction	14
Friction Angle	30°
Lateral Limits	20°

	Critical	**Total**	**%**
Flexural Toppling (All)	166	1754	9.46%
Flexural Toppling (Set 1: J1)	19	545	3.49%

Plot Mode	Pole Vectors
Vector Count	1754 (1754 Entries)
Hemisphere	Lower
Projection	Equal Area

Figure 5.24 Kinematic analysis for flexural toppling in slope section 1, at Lærdal study area. Mapped discontinuities are represented by poles (points) in the stereonet. Poles located within the critical zone (red shaded area) represent the potential slip surface between blocks.

The kinematic analysis indicates that flexural toppling is a possible failure mechanism, with 9.46 % of all measurements plotting within the critical zone (figure 5.24). A few of the critical discontinuities belong to joint set J1, but most of them appear random.

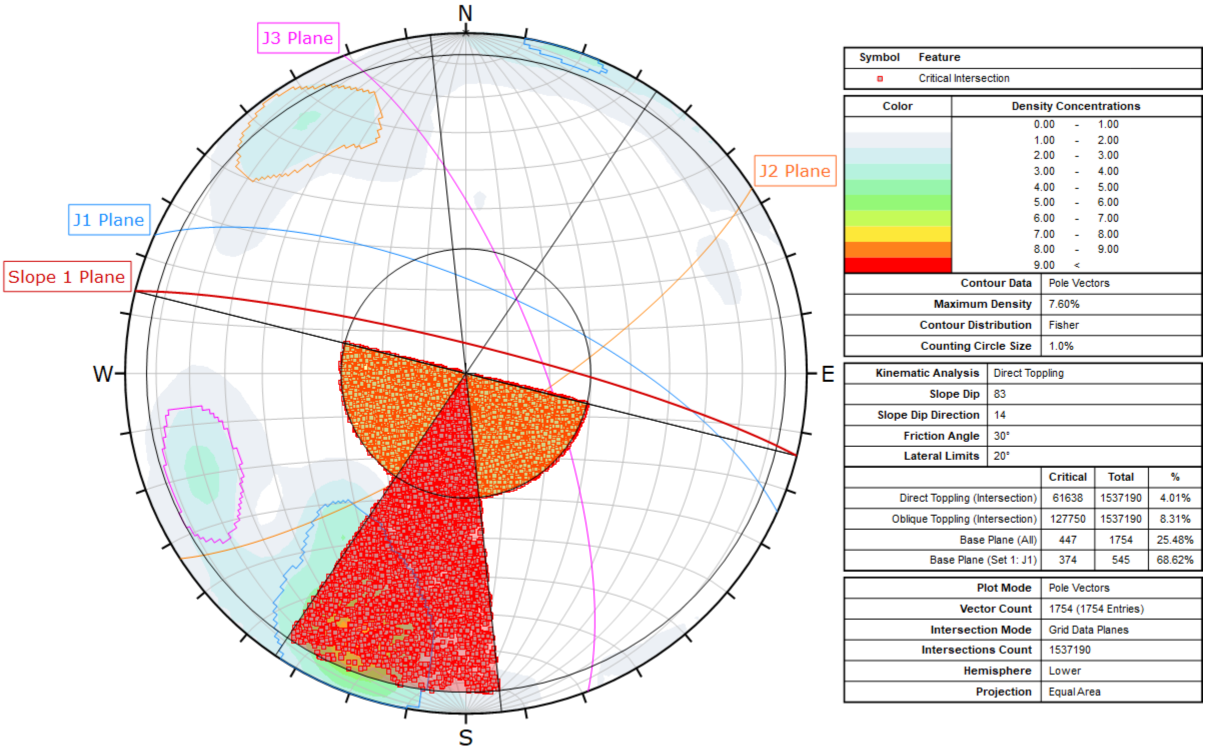

Symbol	Feature
▫	Critical Intersection

Color	Density Concentrations
⬜	0.00 - 1.00
⬜	1.00 - 2.00
🟦	2.00 - 3.00
🟦	3.00 - 4.00
🟩	4.00 - 5.00
🟩	5.00 - 6.00
🟨	6.00 - 7.00
🟨	7.00 - 8.00
🟧	8.00 - 9.00
🟥	9.00 <

Contour Data	Pole Vectors
Maximum Density	7.60%
Contour Distribution	Fisher
Counting Circle Size	1.0%

Kinematic Analysis	Direct Toppling
Slope Dip	83
Slope Dip Direction	14
Friction Angle	30°
Lateral Limits	20°

	Critical	**Total**	**%**
Direct Toppling (Intersection)	61638	1537190	4.01%
Oblique Toppling (Intersection)	127750	1537190	8.31%
Base Plane (All)	447	1754	25.48%
Base Plane (Set 1: J1)	374	545	68.62%

Plot Mode	Pole Vectors
Vector Count	1754 (1754 Entries)
Intersection Mode	Grid Data Planes
Intersections Count	1537190
Hemisphere	Lower
Projection	Equal Area

Figure 5.25 Kinematic analysis for direct toppling in slope section 1, at Lærdal study area. Mapped discontinuities are contoured in the stereonet. Discontinuity intersections are visible as points when they are located within the critical zones (red/yellow shaded areas). Critical poles represent the potential basal surfaces of toppling blocks, while the discontinuities with critical intersections represents the lateral and rear surfaces of those blocks.

The kinematic analysis indicates that direct toppling is possible, but that oblique toppling is more likely (figure 5.25). Joint set J1 is likely to act as a basal plane, while J2 and J3 could form the lateral and rear release surfaces of toppling blocks. Only 4.01 % of the intersections plot within the primary critical zone (red shaded area) that indicates direct toppling, but because of the large discontinuity datasets this is still a considerable amount. Furthermore, 8.31 % of all the intersections plot within the secondary critical zone (yellow shaded area) that indicates oblique toppling.

Summary

In Lærdal study area, the kinematic analyses suggest that the most likely failure mechanisms are planar and wedge sliding. This corresponds well with observations. The analyses also suggest that flexural and direct/oblique toppling are possible. There are no observations of systematic and closely spaced rock columns in the slope. However, the steep slope and the heavily jointed rock mass suggests that both flexural and direct/oblique toppling might be possible.

5.4.4 Ørnlia

A total of 1393 discontinuity measurements were mapped for the Ørnlia study area and included in the kinematic analyses. The friction angle was set to 30º and lateral limits to 20º. The analyzed slope section has an orientation of 41/258. Stereonets containing the kinematic analysis results for planar sliding, wedge sliding, flexural toppling and direct toppling are presented in figures 5.26-5.29.

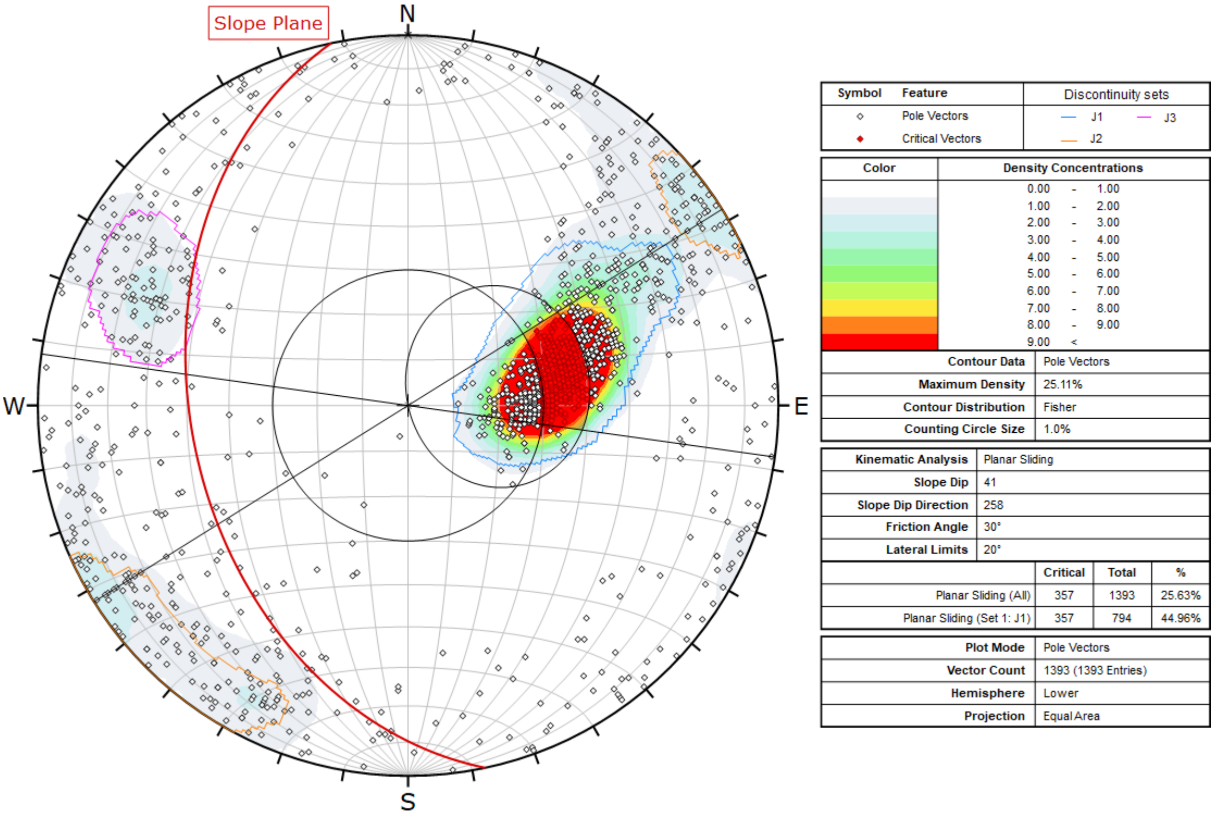

Symbol	Feature	Discontinuity sets
◇	Pole Vectors	— J1 — J3
◆	Critical Vectors	— J2

Color	Density Concentrations
⬜	0.00 - 1.00
⬜	1.00 - 2.00
🟦	2.00 - 3.00
🟦	3.00 - 4.00
🟩	4.00 - 5.00
🟩	5.00 - 6.00
🟩	6.00 - 7.00
🟨	7.00 - 8.00
🟧	8.00 - 9.00
🟥	9.00 <

Contour Data	Pole Vectors
Maximum Density	25.11%
Contour Distribution	Fisher
Counting Circle Size	1.0%

Kinematic Analysis	Planar Sliding
Slope Dip	41
Slope Dip Direction	258
Friction Angle	30°
Lateral Limits	20°

	Critical	Total	%
Planar Sliding (All)	357	1393	25.63%
Planar Sliding (Set 1: J1)	357	794	44.96%

Plot Mode	Pole Vectors
Vector Count	1393 (1393 Entries)
Hemisphere	Lower
Projection	Equal Area

Figure 5.26 Kinematic analysis for planar sliding at Ørnlia study area. Mapped discontinuities are represented by poles (points) in the stereonet. Poles located within the critical zone (red shaded area) represent potential basal sliding surfaces.

The kinematic analysis show that planar sliding is a likely failure mechanism, with 25.63 % of all measurements plotting within the critical zone (figure 5.26). All the critical discontinuities belong to joint set J1, which would act as the basal sliding plane of failing blocks. The rear release surface is defined by J2, and J3 could form the lateral release. The scatter in the plot reveals that there are also random discontinuities that could act as release surfaces.

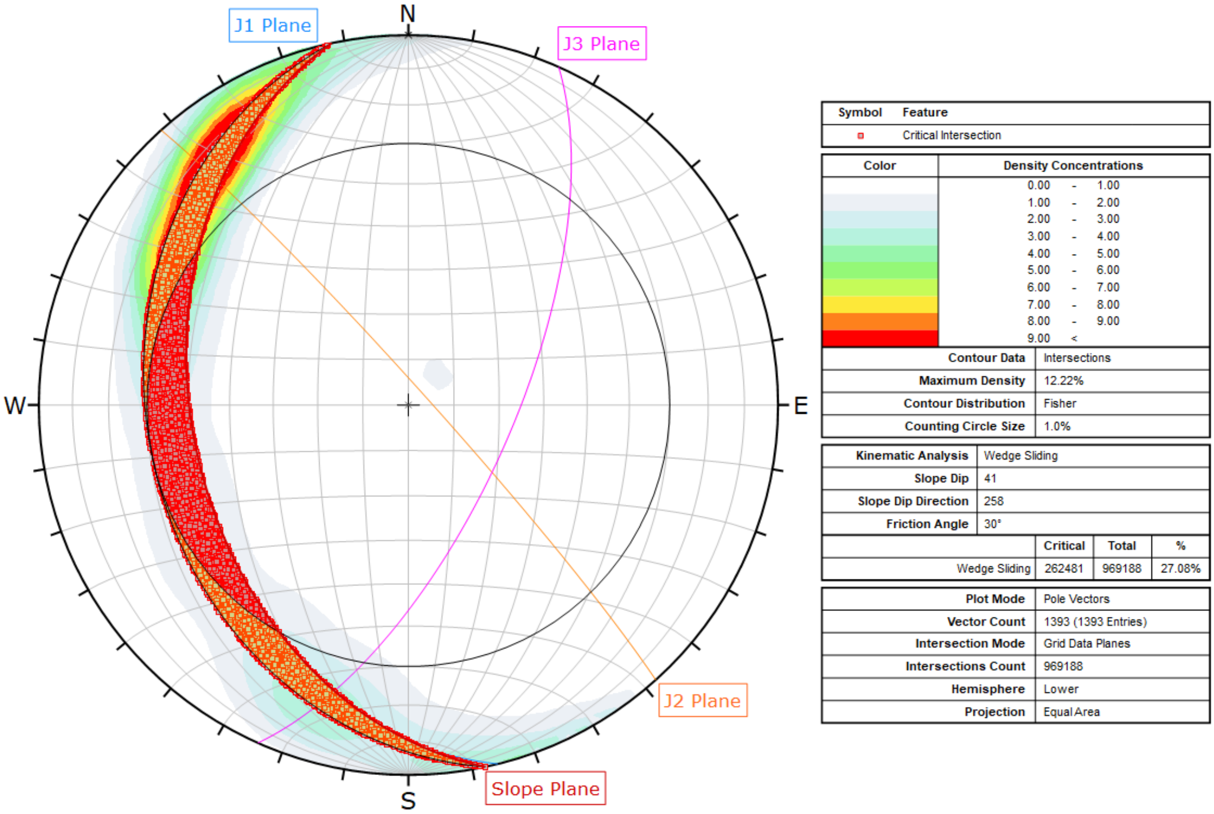

Symbol	Feature
▫	Critical Intersection

Color	Density Concentrations
⬜	0.00 - 1.00
⬜	1.00 - 2.00
⬜	2.00 - 3.00
🟩	3.00 - 4.00
🟩	4.00 - 5.00
🟩	5.00 - 6.00
🟨	6.00 - 7.00
🟨	7.00 - 8.00
🟧	8.00 - 9.00
🟥	9.00 <

Contour Data	Intersections
Maximum Density	12.22%
Contour Distribution	Fisher
Counting Circle Size	1.0%

Kinematic Analysis	Wedge Sliding
Slope Dip	41
Slope Dip Direction	258
Friction Angle	30°

	Critical	Total	%
Wedge Sliding	262481	969188	27.08%

Plot Mode	Pole Vectors
Vector Count	1393 (1393 Entries)
Intersection Mode	Grid Data Planes
Intersections Count	969188
Hemisphere	Lower
Projection	Equal Area

Figure 5.27 Kinematic analysis for wedge sliding at Ørnlia study area. Intersections between mapped discontinuities are contoured, and visible as points when they are located within the critical zones (red/yellow shaded areas). Discontinuities with critical intersections represent the basal planes of potential wedge failures.

Wedge sliding also presents as a likely failure mechanism, with 27.08 % of all discontinuity intersections plotting within the critical zones (figure 5.27). Two possible combinations of joint sets can form critical wedges, J1+J2 and J1+J3. The intersections of the two combinations plot in both the primary and the secondary critical zones (red and yellow shaded areas). This means that in some cases sliding occurs along both discontinuity planes, and in other cases sliding only occur along J1, which is semi-parallel to the slope.

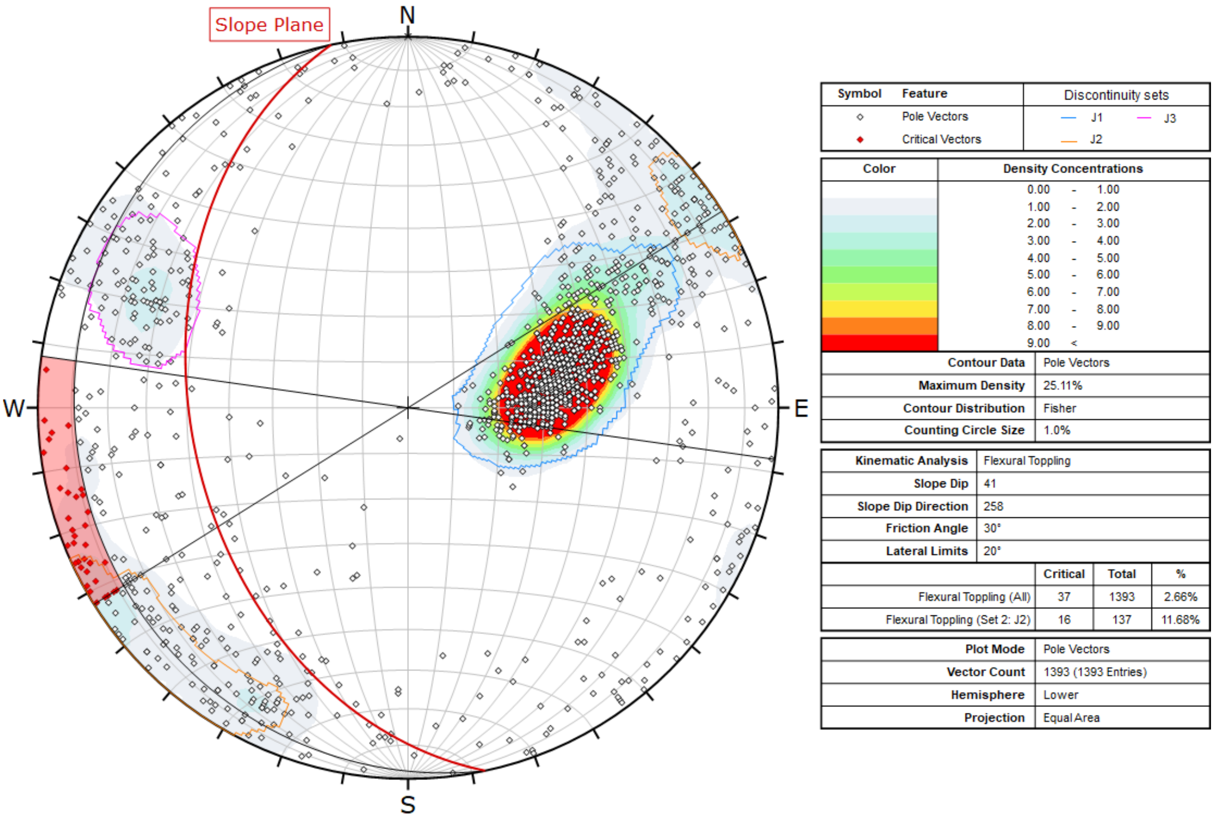

Figure 5.28 Kinematic analysis for flexural toppling at Ørnlia study area. Mapped discontinuities are represented by poles (points) in the stereonet. Poles located within the critical zone (red shaded area) represent the potential slip surface between toppling rock columns.

The kinematic analysis indicates that flexural toppling is an unlikely failure mechanism, with only 2.66 % of all measurements plotting within the critical zone (figure 5.28).

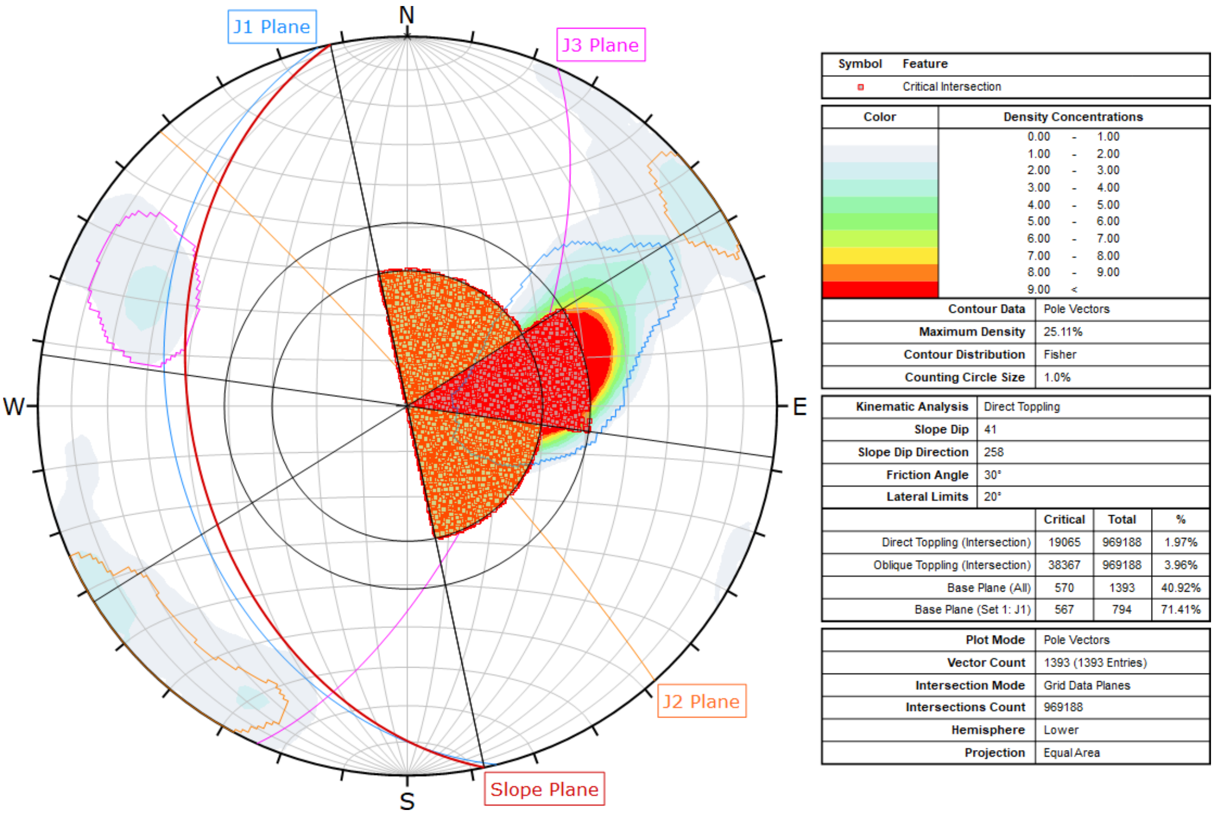

Symbol	Feature
▫	Critical Intersection

Color	Density Concentrations
⬜	0.00 - 1.00
⬜	1.00 - 2.00
⬜	2.00 - 3.00
🟩	3.00 - 4.00
🟩	4.00 - 5.00
🟩	5.00 - 6.00
🟨	6.00 - 7.00
🟨	7.00 - 8.00
🟧	8.00 - 9.00
🟥	9.00 <

Contour Data	Pole Vectors
Maximum Density	25.11%
Contour Distribution	Fisher
Counting Circle Size	1.0%

Kinematic Analysis	Direct Toppling
Slope Dip	41
Slope Dip Direction	258
Friction Angle	30°
Lateral Limits	20°

	Critical	Total	%
Direct Toppling (Intersection)	19065	969188	1.97%
Oblique Toppling (Intersection)	38367	969188	3.96%
Base Plane (All)	570	1393	40.92%
Base Plane (Set 1: J1)	567	794	71.41%

Plot Mode	Pole Vectors
Vector Count	1393 (1393 Entries)
Intersection Mode	Grid Data Planes
Intersections Count	969188
Hemisphere	Lower
Projection	Equal Area

Figure 5.29 Kinematic analysis for direct toppling at Ørnlia study area. Mapped discontinuities are contoured in the stereonet. Discontinuity intersections are visible as points when they are located within the critical zones (red/yellow shaded areas). Critical poles represent the potential basal surfaces of toppling blocks, while the discontinuities with critical intersections represents the lateral and rear surfaces of those blocks.

The kinematic analysis indicates that direct and oblique toppling are possible but unlikely failure mechanisms (figure 5.29). While joint set J1 is likely to act as a basal plane, there is only a small portion of the discontinuity intersections that could represent the lateral and rear release surfaces that are required for block toppling. As little as 1.97 % of the intersections plot within the primary critical zone (red shaded area) that indicates direct toppling, and 3.96 % plot within the secondary critical zone (yellow shaded area) that indicates oblique toppling.

Summary

In Ørnlia study area, the kinematic analyses suggest that the most likely failure mechanisms are planar and wedge sliding. Observations confirms that planar failure is common. Like Valle study area, wedges are observed to be truncated by a slope parallel plane at the base and the intersecting planes that form the wedges appear very steep. This indicates that sliding occur mainly along the basal plane and that the failure mode is closer to planar sliding.

5.4.5 Straumklumpen

A total of 1222 discontinuity measurements were mapped for the Straumklumpen study area and included in the kinematic analyses. The friction angle was set to 30º and lateral limits to 20º. The analyzed slope section has an orientation of 49/205. Stereonets containing the kinematic analysis results for planar sliding, wedge sliding, flexural toppling and direct toppling are presented in figures 5.30-5.33.

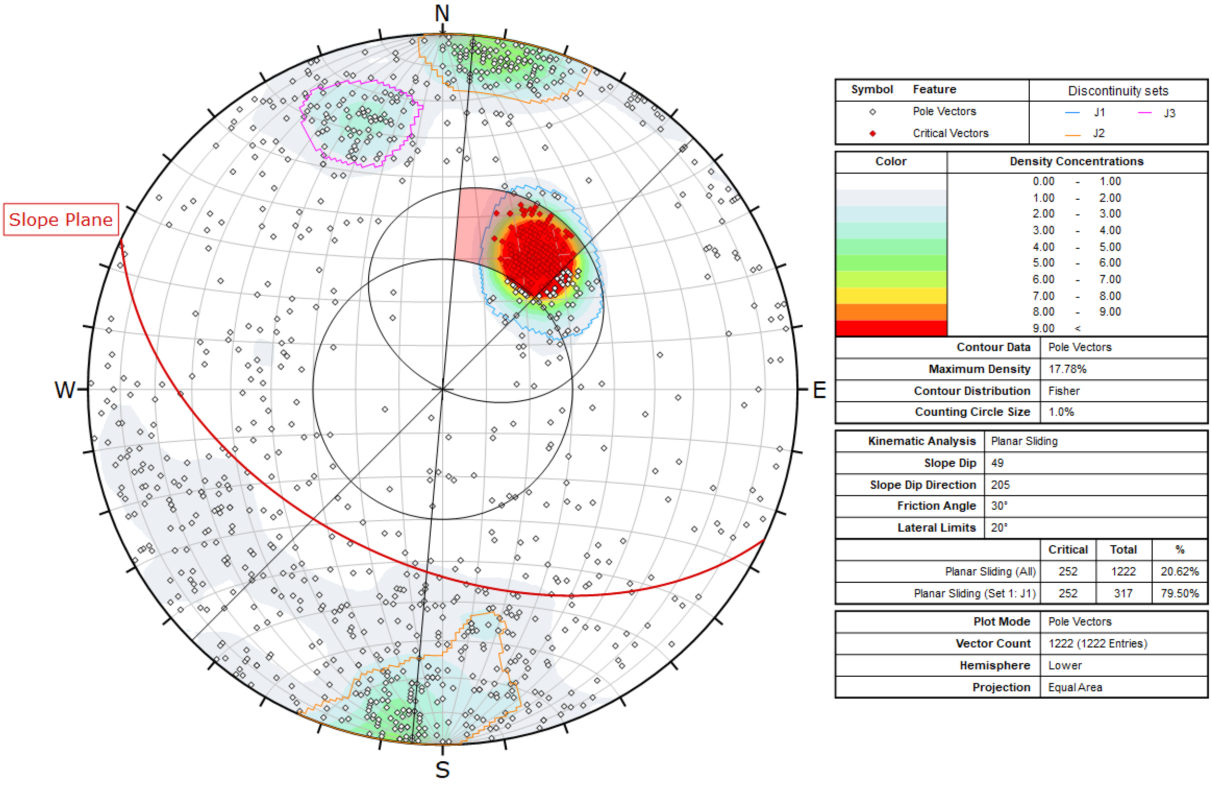

Figure 5.30 Kinematic analysis for planar sliding at Straumklumpen study area. Mapped discontinuities are represented by poles (points) in the stereonet. Poles located within the critical zone (red shaded area) represent potential basal sliding surfaces.

The kinematic analysis show that planar sliding is a likely failure mechanism, with 20.62 % of all measurements plotting within the critical zone (figure 5.30). All the critical discontinuities belong to joint set J1, which would act as the basal sliding plane of failing blocks. The rear release surface could be defined by J2, and the lateral release by J3. Though the degree of scatter in the plot reveals that there are also many random discontinuities that could act as release surfaces.

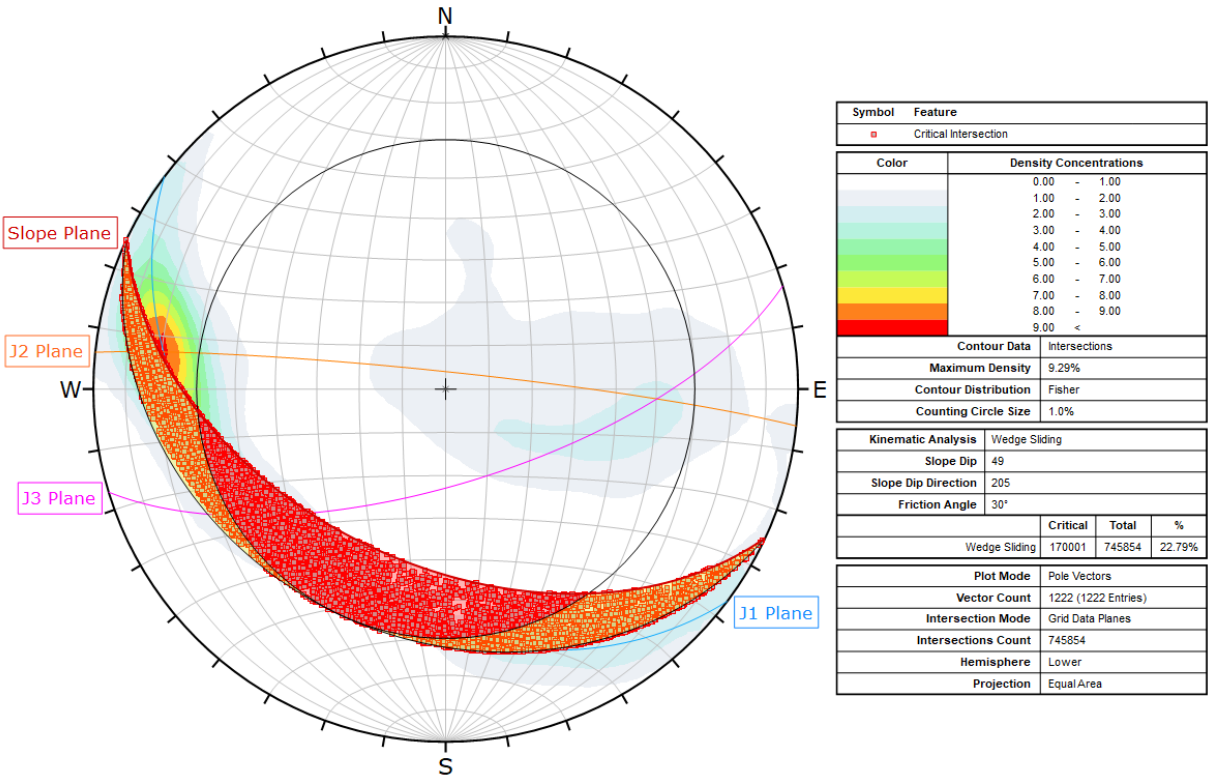

Symbol	Feature
▫	Critical Intersection

Color	Density Concentrations
⬜	0.00 - 1.00
⬜	1.00 - 2.00
🟦	2.00 - 3.00
🟩	3.00 - 4.00
🟩	4.00 - 5.00
🟩	5.00 - 6.00
🟨	6.00 - 7.00
🟨	7.00 - 8.00
🟧	8.00 - 9.00
🟥	9.00 <

Contour Data	Intersections
Maximum Density	9.29%
Contour Distribution	Fisher
Counting Circle Size	1.0%

Kinematic Analysis	Wedge Sliding
Slope Dip	49
Slope Dip Direction	205
Friction Angle	30°

	Critical	**Total**	**%**
Wedge Sliding	170001	745854	22.79%

Plot Mode	Pole Vectors
Vector Count	1222 (1222 Entries)
Intersection Mode	Grid Data Planes
Intersections Count	745854
Hemisphere	Lower
Projection	Equal Area

Figure 5.31 Kinematic analysis for wedge sliding at Straumklumpen study area. Intersections between mapped discontinuities are contoured, and visible as points when they are located within the critical zones (red/yellow shaded areas). Discontinuities with critical intersections represent the basal planes of potential wedge failures.

Wedge sliding also presents as a likely failure mechanism, with 22.79 % of all discontinuity intersections plotting within the critical zones (figure 5.31). The joint sets J1 and J3 intersects both within the primary critical zone (red shaded area) and the secondary critical zone (yellow shaded area). This means that in some cases sliding occurs along both discontinuity planes, and in other cases sliding only occur along J1, which is semi-parallel to the slope. A combination of J1 and J2 could also produce wedges, with sliding only along J1.

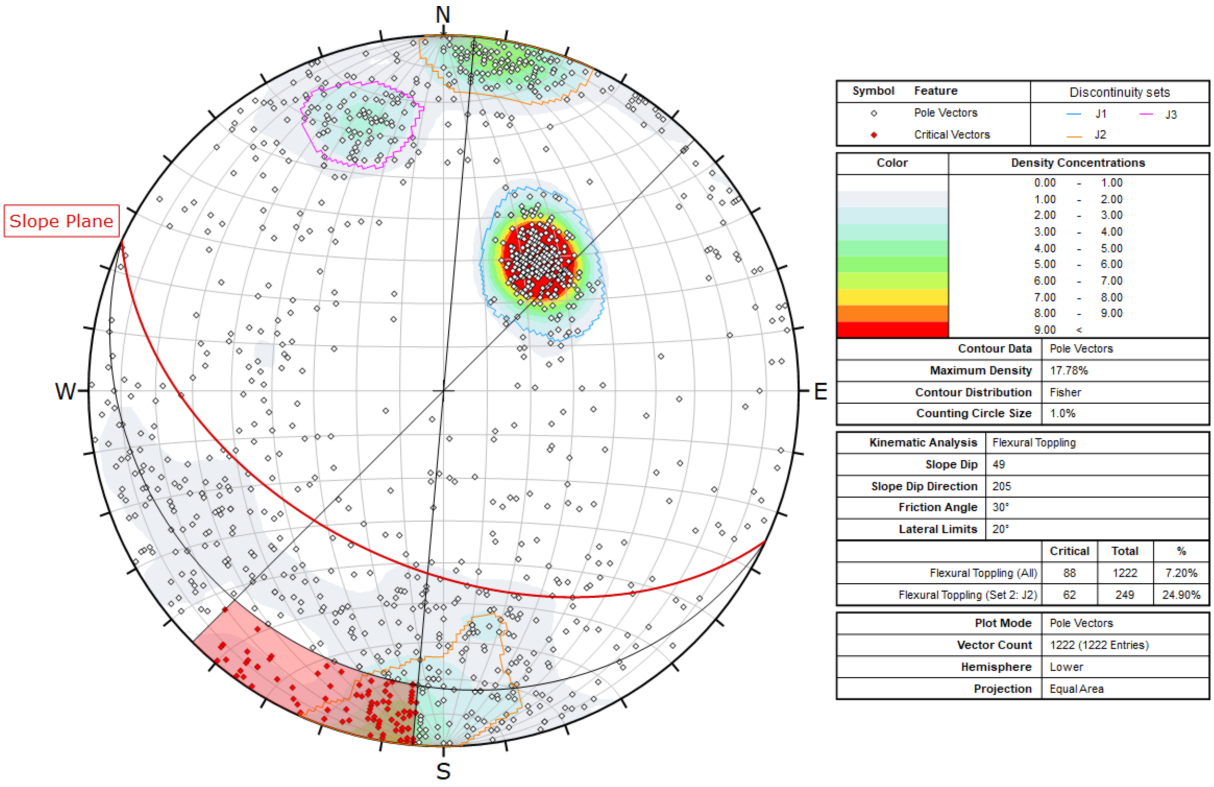

Symbol	Feature	Discontinuity sets
◇	Pole Vectors	J1 · J3
◆	Critical Vectors	J2

Color	Density Concentrations
⬜	0.00 - 1.00
⬜	1.00 - 2.00
🟦	2.00 - 3.00
🟦	3.00 - 4.00
🟩	4.00 - 5.00
🟩	5.00 - 6.00
🟩	6.00 - 7.00
🟨	7.00 - 8.00
🟧	8.00 - 9.00
🟥	9.00 <

Contour Data	Pole Vectors
Maximum Density	17.78%
Contour Distribution	Fisher
Counting Circle Size	1.0%

Kinematic Analysis	Flexural Toppling
Slope Dip	49
Slope Dip Direction	205
Friction Angle	30°
Lateral Limits	20°

	Critical	**Total**	**%**
Flexural Toppling (All)	88	1222	7.20%
Flexural Toppling (Set 2: J2)	62	249	24.90%

Plot Mode	Pole Vectors
Vector Count	1222 (1222 Entries)
Hemisphere	Lower
Projection	Equal Area

Figure 5.32 Kinematic analysis for flexural toppling at Straumklumpen study area. Mapped discontinuities are represented by poles (points) in the stereonet. Poles located within the critical zone (red shaded area) represent the potential slip surface between toppling rock columns.

The kinematic analysis indicates that flexural toppling is possible, with 7.20 % of all measurements plotting within the critical zone (figure 5.32). Many of the critical discontinuities belong to joint set J2, but there are also several random discontinuities.

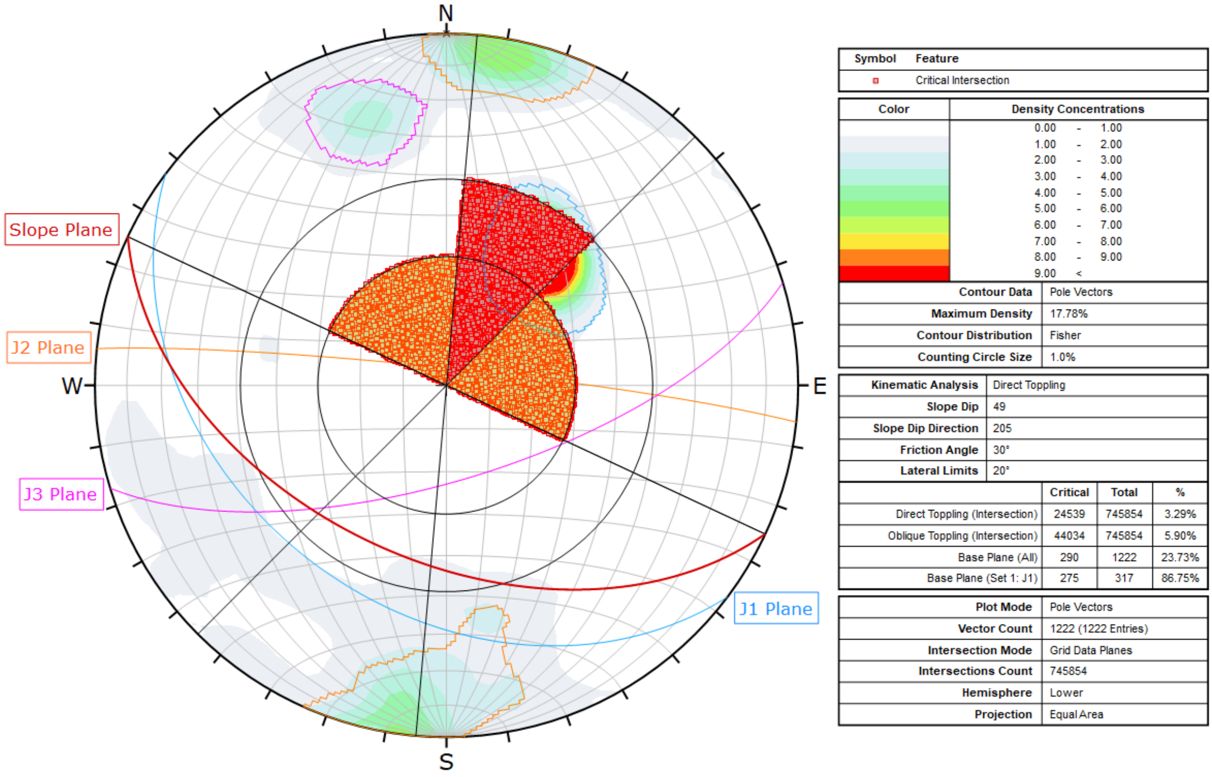

Symbol	Feature
▫	Critical Intersection

Color	Density Concentrations
⬜	0.00 - 1.00
⬜	1.00 - 2.00
🟦	2.00 - 3.00
🟦	3.00 - 4.00
🟩	4.00 - 5.00
🟩	5.00 - 6.00
🟨	6.00 - 7.00
🟨	7.00 - 8.00
🟧	8.00 - 9.00
🟥	9.00 <

Contour Data	Pole Vectors
Maximum Density	17.78%
Contour Distribution	Fisher
Counting Circle Size	1.0%

Kinematic Analysis	Direct Toppling
Slope Dip	49
Slope Dip Direction	205
Friction Angle	30°
Lateral Limits	20°

	Critical	Total	%
Direct Toppling (Intersection)	24539	745854	3.29%
Oblique Toppling (Intersection)	44034	745854	5.90%
Base Plane (All)	290	1222	23.73%
Base Plane (Set 1: J1)	275	317	86.75%

Plot Mode	Pole Vectors
Vector Count	1222 (1222 Entries)
Intersection Mode	Grid Data Planes
Intersections Count	745854
Hemisphere	Lower
Projection	Equal Area

Figure 5.33 Kinematic analysis for direct toppling at Straumklumpen study area. Mapped discontinuities are contoured in the stereonet. Discontinuity intersections are visible as points when they are located within the critical zones (red/yellow shaded areas). Critical poles represent the potential basal surfaces of toppling blocks, while the discontinuities with critical intersections represents the lateral and rear surfaces of those blocks.

The kinematic analysis indicates that direct and oblique toppling are possible failure modes (figure 5.33). Joint set J1 is likely to act as a basal plane, while J2 and J3 could form the lateral and rear release surfaces of toppling blocks. Only 3.29 % of the intersections plot within the primary critical zone (red shaded area) that indicates direct toppling, and 5.90 % plot within the secondary critical zone (yellow shaded area) that indicates oblique toppling.

Summary

In Straumklumpen study area, the kinematic analyses suggest that the most likely failure mechanisms are planar and wedge sliding. This corresponds well with observations. Though many of the wedges appear to be truncated by a slope parallel plane at the base, which is seen also in Valle and Ørnlia study areas. The analyses also suggest that flexural and direct/oblique toppling are possible. But there are no observations supporting this, as blocks tend to form sheets rather than columns.

6 Discussion

6.1 Survey Design

The field surveys of the study areas were designed to satisfy the first objective of the thesis (section 1.3). Namely, to establish a functional survey design for collecting datasets of sufficient coverage and quality to serve as a basis for photogrammetric reconstructions and subsequent digital mapping, by using relatively simple and cost-effective tools, such as drone-based consumer-grade cameras and GNSS receivers. Seeing that the requested datasets have been collected and successfully used as a basis for the intended tasks, it is concluded that the first objective has been achieved. Results supporting this claim, along with reasoning, are presented below.

Fieldwork was conducted at each of the five selected study areas, where both images and GNSS measurements were collected, as described in section 4.1. All the essential parts of the study areas are covered by images with sufficient overlap that in general exceeds 9 images (section 5.1 and appendix B). While the sharpness varies between images, the number of images that had to be discarded due to blurriness did not have a crucial effect on the photogrammetric reconstructions. This illustrates that automatic adjustment of camera settings (ISO and shutter speed), that was applied in this study, can produce image datasets with acceptable quality.

The average survey range (i.e. camera-target distance) during image collection was 40-70 m and corresponded to ground sampling distances (i.e. image resolution) of 1.4-2.2 cm/pixel (section 5.1). This translates to a model resolution of 510-1400 points/m^2 (table 5.4), which is very high considering that the best models provided by Kartverket have a resolution of 2-5 points/m^2 (table 4.3). These high model resolutions enabled digital mapping of discontinuities and their characteristics, including surface roughness (section 5.3). The ground sampling distances are within the range (0.2-10.8 cm/px) of the 26 geotechnical surveys summarized by Zekkos et al. (2018).

Many researchers apply automated flight with a predefined flight plan in their surveys (James et al., 2017; Rodriguez et al., 2020) because it allows for greater control of image network geometry and better reproducibility. However, it adds another step to a method that already consists of several parts and the results of this study show that it is possible to achieve satisfactory datasets using manual flight. Another aspect to using automated flight is that the drone needs to receive the satellite positioning signal and is vulnerable for disturbances like those experienced during the fieldwork at Ørnlia and Straumklumpen study areas (4.1.3). Some advantages of manual flight are fast drone deployment and increased flexibility.

During this study there were some challenges related to GNSS measurements of ground control point (GCP) positions. Complete datasets for all study areas were in the end successfully obtained through a combination of field measurements (4.1.3) and an alternative method utilizing orthophotos and LiDAR DEMs (4.1.5). The model validations revealed that the best georeferenced study area was Ørnlia, where the alternative method of identifying GCPs and extracting their coordinates was applied. This is a bit surprising because the uncertainty of coordinates obtained with the alternative method were estimated to be 35-50 cm, which is considerably larger than the calculated uncertainty of the GNSS recordings for Tunhovd and Valle (3-4 cm). The most obvious and likely explanation for why this model performed so well in the validation is that a large number of GCPs were used in relation to the size of the study area. In addition, the model for Ørnlia was the only one for which the recorded image positions had to be adjusted, through applying a python script (section 4.2.2). It is possible that this correction worked so well that it could explain part of why the model was so accurate. Based on the results of this study, it is concluded that the use of orthophotos and DEMs represents another viable method of obtaining data for georeferencing. This is an important finding because it increases the usability of drone derived SfM photogrammetry.

The GNSS recording problems that were experienced at Lærdal study area were successfully overcome by logging raw data and applying post processing. This type of instrument recording issue is likely a result of the view between the receiver and some of the satellites being blocked by the steep north facing mountainside, since the study area is located on northern latitudes and most satellites have southerly orbits. Whenever surveys are conducted on slopes with similar characteristics as the study area in Lærdal, the same type of recording issue might arise and should be considered in advance.

While drone-based image collection is a method that has many advantages, there are also some limitations that require consideration. Firstly, there are national and local regulations for flight with a Remotely Piloted Aircraft System (RPAS), that restricts the use and, in some areas, also prohibits flight (section 4.1.4). One of the regulations that are most important to consider when planning to survey large rock slopes in Norway, is that the maximum flight altitude is restricted to a distance of 120 m from the ground (Luftfartstilsynet, 2021c). How this distance is defined, has changed since the surveys of this study were conducted. From previously measuring the vertical distance to the ground underneath the drone, the new regulations state that the 120 m can be measured between the drone and any point on the ground (e.g. high up on a steep rock wall). The new definition allows drone-derived SfM photogrammetry to be applied in a wider range of terrain settings than before.

Other limiting factors include high wind speeds (> 10 m/s), low temperatures (< 0ºC), rain, and the flight battery capacity, which is 21-27 min/battery for the DJI Mavic Pro used in this study (DJI, 2017). An observation from the fieldwork is that the equipment includes several batteries and devices (i.e. RPAS flight batteries, RPAS remote controller, iPad, GNSS receiver, GNSS field computer), that combined can take many hours to charge. Surveys of large slopes may require several days in the field to be completed. It is therefore important to have a plan that both ensures flights during the most favorable lighting and weather conditions, and efficient charging of the batteries in between.

A functional survey design can be defined as one that balances the need for producing accurate datasets, against limitations in resources and time consumption. It is time consuming to make detailed surveys of large rock slopes and computationally demanding to process the collected datasets. The results of this study show that slopes may not need to be mapped with the same level of detail throughout when the lithology and joint sets are relatively homogenous. A representative section of such a slope could be surveyed at closer range and used for digital mapping of discontinuities. For the rest of the slope, it would be sufficient to collect fewer images taken at a longer distance, if the dataset is to be used only for identifying and measuring unstable blocks. This is a simple way of reducing the amount of data that needs to be collected and the time spent doing it.

6.2 Agisoft Metashape Workflow

The second objective of this thesis is to establish an efficient workflow for generating and validating georeferenced 3D models of sufficient quality to serve as a basis for digital mapping (section 1.3). Seeing that the requested models have been generated, validated, and successfully used as a basis for the intended tasks, it is concluded that the second objective has been achieved. Results supporting this claim, along with reasoning, are presented below and in section 6.3. This section will discuss the part of objective two that is related to the workflow that was used to perform photogrammetric reconstructions with the Agisoft Metashape software.

Agisoft Metashape is a widely used software for photogrammetric processing, but because it is a commercial product the producers provide very little information about the technique and complex algorithms behind the largely automated processing steps. This makes it impossible to foresee the full effect that different tools and settings will have on a specific dataset, only by reading the user manual or other sources. In this study, the effects of almost every available tool and filter in Metashape were tested for different settings, to find an optimized workflow for those specific projects and to establish the best general workflow for similar projects (section 4.2.2 and Appendix A). The similarity refers both to input dataset properties (such as target scale, camera model, image resolution, and number of images), and output requirements related to accuracy and resolution. While an acceptable model might be generated using default settings and the simple workflow suggested in the manual, it will not exploit the full potential of the input dataset. In this study the model accuracy (considering the error estimates provided by the software) was improved by up to 80 % when applying the tailored workflow, compared to the default. This illustrates that a tailored workflow can allow a dataset of sub-optimal quality to be used efficiently.

Some of the most important lessons learned from establishing the workflow will be expanded upon on here. Firstly, it is crucial to change the default accuracy for image and ground control point (GCP) coordinates, to values that are representative of the actual input datasets. The measurements will otherwise be assigned incorrect importance when weighted against each other in the georeferencing process, which may ultimately result in a less accurate model. This study used the calculated GNSS measurement precisions (section 5.3) as input accuracy for GCPs. For those GCPs that were not recorded with a GNSS receiver, accuracies were estimated based on the quality of the datasets from which the coordinates were extracted (section 4.1.5). When it comes to images collected with a drone, the positions registered by the onboard GNSS can be quite uncertain and the largest errors are generally observed for the altitude. This was also observed for all the collected datasets in this study. Keeping the horizontal accuracy at the 10 m default value and changing the vertical accuracy to 30 m was found to be a good compromise that improved all the reconstructions.

The most manual step in the workflow is marker placement, which involves pointing out the GCPs in every image where they are visible, by clicking on them. In some online tutorials it is stated that GCPs only needs to be indicated in a few images, but the tests in this study show that this adversely effects the model accuracy and that it is worthwhile to indicate GCPs in as many images as possible. Another part of the workflow that was important for optimizing the results, was the use of filters to remove noise and uncertain points from the point clouds. When applying the filters, it is important not to remove too many points. This is because images with few sampled points are not used further in the processing, which might lead to decreased overall accuracy. It was found that changing the settings for the “align photos” step (section 4.2.2), so that more points could be sampled in every image, made it possible to apply a more aggressive filtering of the cloud afterword. This resulted in models with less noise and higher accuracy. The values that represent the optimal key and tie point limits for a project are related to the image size, which was 12.35 MP in this study (section 4.1.4).

A limiting factor for applying this method on large image datasets, is that it is very computationally demanding and requires a powerful workstation with a high-performance graphical processing unit (GPU) and large storage capacity (Anderson et al., 2019). The Metashape software appears stable, in the sense that a heavy workload did not cause the computer to crash, only to use very long time to complete the process. The time consumption varied dramatically between a high-performance computer (hours-days) and a standard computer (days-weeks) when they performed the same processing steps on the same dataset. If the output requirements allow it, a model with lower resolution and quality can be generated to reduce the processing time, by changing the settings to downscale the images (section 4.2.2). Another aspect to consider is that these large projects generate models with large file sizes (e.g. 26 GB for Straumklumpen point cloud), that may be challenging to share or store.

When reconstructing the scene of Ørnlia study area, there was a problem with the photo alignment, because the software failed to recognize that two sets of images were viewing the same scene (section 4.2.2). The images were collected on different days, under different lighting conditions, which can make it more difficult for the software to recognize features. However, in Ørnlia the main issue was large differences in the recorded altitude between the two sets of images. The problem was successfully solved by applying a python script to correct the altitudes. The same type of alignment issue might arise whenever multiple image datasets, collected under different conditions, are combined.

Some concluding remarks is that despite the complexities hidden in the “black box” of the software, Metashape is very user-friendly with an intuitive interface. The automated processing steps makes it possible for non-specialists to generate models, though it is recommended to have at least a basic understanding of what each tool does, and why. The proposed workflow is intended to facilitate the generation of 3D models and allow users with different backgrounds to achieve high-quality results.

6.3 Quality of Photogrammetric Reconstructions

This section adds to the discussion related to the second objective (section 1.3) and will discuss the part that is related to the quality of generated 3D models, and the adopted validation procedure.

The photogrammetric 3D models were validated with regards to georeferencing accuracy and systematic errors, by using Agisoft Metashape and CloudCompare (section 4.3). In Metashape, the check points (CPs) are used as the independent data that represents the 'true' topography that the model is validated against. The georeferencing accuracy is given as the Root Mean Square Error (RMSE) of the CPs and is an integrated part of the Metashape processing chain, making it easy and fast to generate these values. However, it can be both time consuming and challenging to obtain a large enough sample of CPs to have confidence in the error estimates. In this study most of the collected reference points were used as ground control points (GCPs) to georeference the models (which is common practice), leaving only 3-8 points to be used as CPs. The small number of CPs means that there are large uncertainties associated with the estimated values. Contrary, the estimated georeferencing errors obtained with CloudCompare are considered much more reliable, since every point of the model is compared to a reference value (section 4.3.1). When comparing the error estimates of the two methods, the check point RMSEs range from being 80 % smaller (Tunhovd) to being 176 % larger (Ørnlia) than the CloudCompare estimates.

In the Cloud-to-cloud (C2C) comparison, high-accuracy LiDAR (i.e. laser scanning) point clouds were used as reference to represent the 'true' topography. The C2C results revealed that the georeferencing for the smallest study areas, Tunhovd and Ørnlia, performed well with an estimated accuracy of 17-20 cm (table 5.5). The georeferencing for the medium sized study areas, Lærdal and Valle, exhibited larger variations within the models but were considered sufficiently accurate (mean value 37 cm). There appears to be a relationship between model size and achievable georeferencing accuracy. Straumklumpen, which is the largest study area, also exhibits the largest uncertainty (mean value 60 cm). As such, the Straumklumpen model was the only model containing parts that were regarded as to uncertain (> 1 m) for the digital mapping and analyses.

While the C2C validation method is considered to be both comprehensive and robust, there are some aspects or limitations of the LiDAR data that can modify the results. Firstly, the LiDAR data itself has an uncertainty of 3-10 cm which adds uncertainty to the calculated model distances. Also, LiDAR accuracies might locally be lower than the average values of large datasets, especially in areas with steep and complex terrain. Such terrain can be difficult to cover with LiDAR and can produce holes in the model. This was observed to some degree in all the reference models and caused unrealistically high C2C distances in those areas (figure 4.3). The effect was mitigated by setting a maximum distance of 3 m.

Rodriguez et al. (2020) applied a two-method validation that included both the C2C comparison and M3C2, which is another comparison tool available in CloudCompare. The main difference is that M3C2 computes signed distances, i.e. positive values for mass gain and negative values for mass loss, whereas C2C computes absolute distances.

Rockfall activity that might have occurred in the time (2-6 years) between the LiDAR survey and the drone-based image collection will wrongly contribute to lower accuracy estimates in the validation. Changes in vegetation or differences in how such features are edited, could also contribute to lower accuracy estimates. In the Ørnlia model, some of the higher C2C distances coincides with an area of the slope where entrepreneurs were in the process of removing unstable blocks during the fieldwork (figure 6.1). As such, it makes sense that the model differences should be larger here and illustrates the potential of the cloud comparison methods for identifying and quantifying rockfalls. Although, when making volume measurements a method which provides signed distances should be used, e.g. M3C2 in CloudCompare.

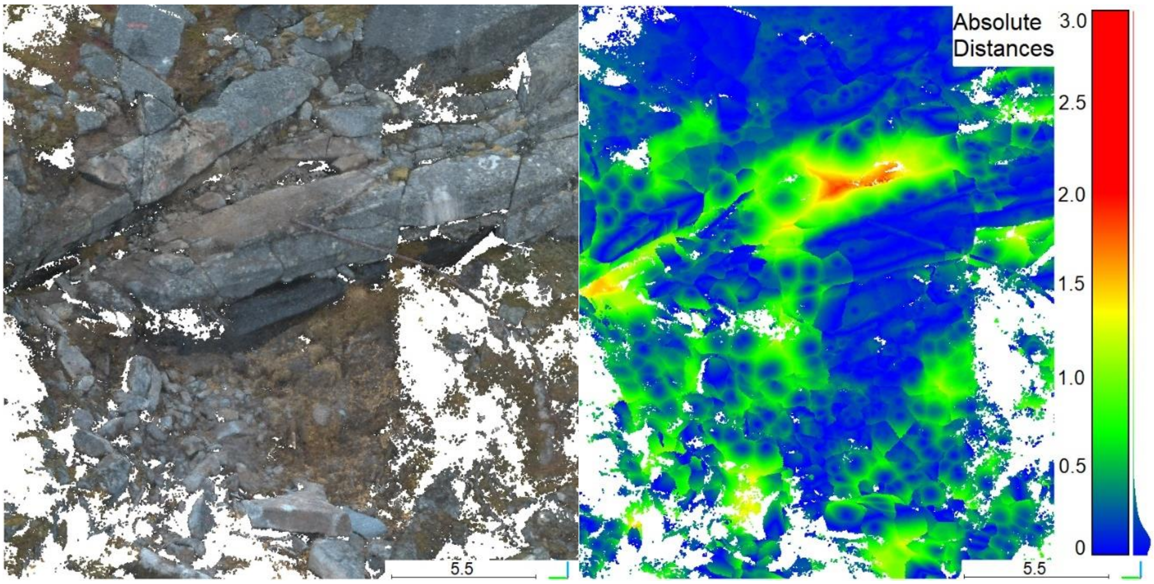

Figure 6.1 Left) Section of the photogrammetric point cloud for Ørnlia study area. Several of the blocks had recently been detached and displaced when the image dataset was collected. Right) Computed C2C distances between the photogrammetric point cloud and a LiDAR point cloud that had been surveyed before the blocks were moved. Distances are colour-coded onto the photogrammetric cloud.

Systematically distributed errors are inherent to use of consumer-grade cameras (section 2.1.1) and were identified in the photogrammetric models during validation (section 5.2). The magnitude and distribution of systematic errors are affected by the geometry of the image network, since vertical (i.e. map view) images captured with a consumer-grade camera along near-parallel flight lines have been shown to introduce radial distortions (James & Robson, 2014; Smith et al., 2016). This study attempted to mitigate this by adapting a survey design that included oblique and convergent imagery (section 4.1.4). It is however difficult to quantify what effect that aspect of the survey design ultimately had on model quality, because the systematic errors in the final models also depend on the camera self-calibration performed during processing (section 2.1.2). Metashape provides diagnostic plots for the camera self-calibration, in which the residual image distortions are visualized as lines (section 4.3.2). All study areas generated similar plots, with distortions appearing systematic in a concentric pattern (appendix C). Though, it is difficult to predict how the distortions in the overlapping images propagates into the model.

The visual representation of computed C2C distances on the point cloud, enables systematic errors in the model to be identified and quantified (figure 5.1). The smallest study areas

(Ørnlia and Tunhovd) do not display systematic errors, but the other study areas do. For Lærdal and Valle, there is a gradual transition from smaller errors in the lower parts of the models, to larger errors at higher elevations. The standard deviation of the C2C distances is ±32 cm for Valle and ±38 cm for Lærdal (table 5.5), which correspond to very small errors in slope angle (< 0.29° over a distance of 150 m). For Straumklumpen study area the observed errors form a more complex pattern, have larger magnitudes, and in some parts of the model the changes occur abruptly. As a result, not all parts of the Straumklumpen model are of sufficient quality to be used as a basis for the digital mapping and analyses.

While the complexity of the SfM method makes it very challenging to quantify individual error sources, the GCP distribution and positioning accuracy are recognized as the most important controlling factors (Smith et al., 2016). Despite having a poorer distribution of GCPs and fewer GCPs than some of the other models, the Tunhovd model obtained higher georeferencing accuracy. This suggests that GCP distribution was not the most critical factor in this study. There do however appear to be a relationship between high georeferencing accuracy and high GCP density (i.e. the number of GCPs in relation to the model area). During the photogrammetric processing, reference points were manually indicated in images by clicking on their locations (section 4.2.2). The RMSE for GCPs (given in pixels) represents the precision of these manual placements. Since all survey areas display relatively low RMSE values (< 1.38 px), the precision of the placements is high and the potential contribution to the identified errors is expected to be minor.

Geometrical accuracy (i.e. accuracy of dip, dip direction, area and volume of local features within the model) was not thoroughly analyzed, but the filters applied in the established Metashape workflow were included to remove much of the noise and outlier points that might otherwise distort the network geometry (section 4.2.2). The C2C comparison can indirectly indicate how well the point network represents the slope geometry. That is, a model with consistently high georeferencing accuracy (such as Tunhovd and Ørnlia) is also expected to have a high geometric accuracy. However, low georeferencing accuracy does not necessarily mean that the geometry is inaccurate since the error could consist of a rigid translation without much internal deformation. By zooming in on the analyzed model with the C2C distances colour-coded on the points, it was possible to make simple visual assessments. Many discontinuity surfaces had uniform colouring and no grading, which indicates that the geometry is accurate. Geometrical accuracy can also be assessed by comparing digitally mapped discontinuity orientations with traditional field measurements, but that was not part of this study.

The resolutions of the generated models are 510-1400 points/m^2 (table 5.4), which proved to be detailed enough to perform roughness analysis on selected discontinuity surfaces when using profile lengths in the range 1.4-10.1 m (section 5.3). Since the obtained resolutions were sufficient for the roughness analyses, they were also more than enough for the other tasks of this study, which all have lower demands.

To summarize this section, a comprehensive validation has been performed to ensure that the models are of sufficient quality with regards to georeferencing accuracy, systematic errors, and resolution. In addition, geometrical accuracy and possible error sources have been discussed. The C2C comparison in CloudCompare is found to be a robust method for validating model accuracy and assessing systematic errors, which can greatly increase the confidence in generated models.

6.4 Analysis Results

The third objective of this thesis is to evaluate different tools, settings, and applications for digital mapping of rock masses, to extract reliable and representative data that could serve as a basis for rockfall hazard assessments (section 1.3). Digital mapping, measurements, and kinematic analyses have been performed to find the values of parameters that are relevant in rockfall hazard assessments (sections 5.3-5.4). Different settings have been tested and their effects assessed. It is concluded that the third objective has been achieved, to a large degree. Results supporting this claim, along with reasoning, are presented below.

The photogrammetric models were used as a basis for digital mapping, performed with the Maptek PointStudio software (section 4.4.1). Discontinuities can be mapped on either a point cloud or a mesh model. Testing revealed that it is faster and less computationally demanding to use a mesh for mapping. However, it is without considering the time that might be saved during photogrammetric processing if the mesh does not have to be generated. When using the point cloud for mapping, it is easier to see which areas of the model that contains little data and therefore yields more uncertain results. Although, being able to view a continuous surface covered by a detailed and photorealistic texture (as for the mesh models), allows for better visual control of the fit between extracted surfaces and discontinuity observations. Ultimately, the mesh models were considered slightly more advantageous and were used for the digital mapping in this study.

Some observations from working with the different tools for mapping discontinuity surfaces in PointStudio, are that the tools and settings that yields the best results vary from model to model, and therefore it is important to tune the settings to fit each specific dataset. The most automated tool, ‘extract’, offers a fast method for extracting large amounts of data (section 4.4.1). Here the settings need to be adjusted so that small discontinuity surfaces are not missed, while avoiding to extract surfaces that either cover only part of observed discontinuities or that extend outside the discontinuities.

In the Tunhovd study area the discontinuities appear very systematic and well-defined, separated by roughly 90º angles (section 5.3.1). These characteristics combined with a relatively high-resolution 3D model, made it easy to map the model with the ‘extract’ tool. Because the exposed discontinuity surfaces had varying sizes, the settings had to be tuned also between discontinuity sets. While the minimum surface area of extracted discontinuities had to be lowered for joint set J2 to include small exposures, the same settings extracted too many erroneous surfaces for the slope parallel J1.

Another observation is that the ‘extract’ tool is biased towards slope parallel discontinuities, with poorer sampling of obliquely oriented sets. Biased sampling when using semi-automated detection of surfaces has also been described by Menegoni et al. (2019). While it is not necessarily an issue for defining discontinuity sets or finding their mean orientations, an unrealistic difference in sample size can affect the reliability of the spacing and persistence estimates. Further, it might affect the kinematic analyses by making some failure modes appear more likely or unlikely. These adverse effects were mitigated either by using a more manual tool (i.e. query or smart query) to pick the slope parallel surfaces instead of the ‘extract’ tool, or by using the manual tools to complement oblique discontinuity sets with surfaces that were not recognized by the ‘extract’ tool.

It is necessary to control the quality of extracted discontinuities by visual inspection, to identify and remove erroneous surfaces (section 4.4.1). The importance of validating extracted surfaces has also been emphasized by Menegoni et al. (2019). The semi-automated mapping tool cannot differentiate between different types of surfaces, and as a result incorrect surfaces were often extracted from displaced blocks or vegetated areas in the models. This was mitigated by cleaning the models from unnecessary parts before starting the extraction. For the Lærdal study area, an excessive number of both correct and incorrect surfaces were identified with the ‘extract’ tool (section 5.3.3). The reason for this is likely due to the character of the rock mass and the discontinuities, which appeared broken-up, irregular, and indistinct. It was found to be faster to only use the more manual tool ‘smart query’, than to sort through and quality check the large number of extracted discontinuities. While manual digital mapping offers a higher degree of control and can be more effective in some cases, it comes at the expense of less objectivity.

The resulting discontinuity sets, and their orientations were validated through qualitative assessments, based on visual inspections in the model, and comparisons with observations from the fieldwork. It is concluded that the observed dominant discontinuity sets and their approximate orientations are well represented in the digitally mapped datasets. The confidence in the results is partly restricted because no quantitative validation was applied, e.g., comparison with compass-clinometer measurements performed on surfaces in the field.

The accuracy of calculated spacing values depends both on the quality of the discontinuity sets used as input and the applied settings (section 4.4.3). In the settings for the spacing analysis, the discontinuity planes were defined as infinite in size. While the analyses might be more comparable and objective by using this setting, it is possible that the results are less accurate compared to estimating a suitable maximum size for each discontinuity set. By comparing the obtained spacing estimates with observations, it seems like the mean spacing might be too small for some of the discontinuity sets containing many surfaces (e.g. J1 in Ørnlia). But the relative size of the spacings appear accurate and together with the persistence estimates they define block shapes that are consistent with observations.

The accuracy of calculated persistence values depends on the quality of the discontinuity sets used as input (section 4.4.3). Because discontinuities are represented by planar surfaces, the persistence might be underestimated for sets containing many undulating or curved discontinuities (e.g. J2 in Valle). Overall, the calculated persistence values appear to agree with the observations.

It is concluded that the obtained model resolutions of 510-1400 points/m^2 (table 5.4) were detailed enough to be used for roughness analysis of discontinuity surfaces. Out of the applied analyses, it is the roughness analysis that requires the highest model resolution to generate realistic results (section 4.4.3). Because of this, both the time consumption and need for computing power can be decreased by using a model with lower resolution for the other tasks of the digital mapping. If the lower resolution model is down-sampled from the original full-resolution model, the larger features of the geometry (i.e. block volume, discontinuity dip/strike and area) should be preserved, while the surface is smoothed.

Many of the tools within the PointStudio software are functional and allow the user to adjust the most important parameters. However, the kinematic analysis lacks some of the functionality and statistics that is provide in the specialized Dips software by Rocscience. This was not an issue in this study since it was straight forward to import discontinuity datasets from PointStudio into Dips and perform the kinematic analyses there instead (section

4.4.2). The failure mechanisms indicated as the most likely by the kinematic analyses, generally correspond well with observations (section 5.4). For the Valle, Ørnlia and Straumklumpen study areas, the kinematic analyses suggest that planar and wedge sliding are the most likely failure modes. In the 3D models for these areas, wedges were observed to be truncated by a slope parallel plane at the base, and the intersecting planes forming the wedges appeared very steep. This was interpreted as evidence that sliding occur mainly along the basal plane, and that the failure mode is more likely planar sliding than wedge sliding.

Tunhovd is the study area where observations and analysis results disagreed the most (section 5.4.1). The analyses suggest that the most likely failure mechanisms are planar and wedge sliding, but observations indicate that toppling is common and could even be the main mechanism. A possible explanation for the discrepancy can be found in the observed bias during extraction of discontinuities. The described approaches for mitigating biased discontinuity sampling were only implemented to smaller degree for Tunhovd. Differences between the discontinuity sets might thus have been exaggerated by the preferential extraction of slope-parallel surfaces, which makes up 65 % of all the mapped discontinuities in Tunhovd (section 5.3.1). In the kinematic analyses the most likely failure modes are the ones that have the largest portion of measurements (i.e. discontinuity poles or intersections) plotted within the critical zones. If the relative sizes of the discontinuity sets are incorrect, this can adversely affect the results.

To summarize this section, different tools for digital mapping of rock masses have been tested and evaluated. Qualitative visual assessments of the mapped and characterized dip, dip direction, spacing, persistence and roughness have been made to validate the results, which appear to be reliable and representative for the study areas, with minor exceptions. The best results were obtained when the settings were tuned to fit each dataset and manual mapping of discontinuities was included as a complement to the semi-automated extraction.

6.5 Applications in Rockfall Hazard Assessment

This section will discuss how the findings in this study relates to previous research and to the aim of the thesis, which is to test if drone-derived SfM photogrammetry and digital mapping are methods that can facilitate, streamline, and improve the determination of relevant parameters for rockfall hazard assessment (section 1.3).

Some of the main advantages associated with drone-derived SfM photogrammetry are its low cost, flexibility, and ease of use (Anderson et al., 2019; Westoby et al., 2012). The method has made it possible for non-specialists to generate detailed topographic data. While this has allowed scientists to themselves collect and process data, the lower level of user expertise has also contributed to less informed processing choices and less rigorous model validation (Anderson et al., 2019; James et al., 2017; Smith et al., 2016). The complexity of the method poses a challenge, and it is difficult to differentiate between the many influencing factors and to quantify their effects (Smith et al., 2016).

This study has tested and established a survey design and photogrammetric workflow that are specifically targeted towards digital mapping of large (> 100 m height) and natural rock slopes. The previous sections discuss which steps and settings are universal, and which needs to be adapted for every project. For those settings that needs to be tuned, a range has been provided (appendices A). During this study some issues were identified and solved or addressed with mitigative measures. The causes of observed and measured variations have been discussed and evaluated. In addition, a comprehensive validation method has been presented (section 6.3).

With these contributions this thesis aspires to help users achieve accurate, precise, and representative results, without needing in-depth knowledge and technical expertise. The thesis also demonstrates what type of parameter settings and uncertainty estimates that are important to report in research. Inadequate reporting of applied workflows and uncertainty estimates has been pointed out as a recurring issue in SfM publications (James et al., 2017; Smith et al., 2016). The alternative method of extracting ground control points (GCPs) from orthophotos and digital elevation models (DEMs) is not novel, but the access to high-resolution datasets with coverage also in remote areas makes this method particularly promising in Norway. In addition, high-resolution LiDAR datasets were used as reference models in the C2C validation (section 4.3). However, in many parts of the world such high-resolution datasets are not available.

As part of a collaboration between MSc theses concerned with rockfalls, it was generated digital surface models (DSMs) of different resolutions (4, 10, 25 and 50 cm/px) for the Lærdal study area. Elise Morken (2021) tested the effects of the different DSM resolutions in dynamic rockfall modelling but found that the simulation times were extensive compared to using available LiDAR models with a resolution of 1 m/pixel. It was concluded that the optimal model resolution for dynamic modelling is 1-2 m/pixel.

Since both laser scanning and photogrammetric methods generate point clouds and meshes, either method can be combined with digital mapping. Laser scanning models often contain holes because of areas that were shadowed during data collection (section 4.3.1). This is not usually an issue for drone-derived SfM photogrammetry (Menegoni et al., 2019). The achievable resolution for SfM photogrammetry is higher than for aerial laser scanning and comparable to terrestrial laser scanning (Smith et al., 2016). SfM photogrammetry has the advantage of very detailed and photorealistic coloured points or textured meshes, which allows visual assessment to be incorporated to a much higher degree in the mapping and analyses. This aspect was very important for validating the extracted discontinuities in this study (section 6.3).

6.6 Limitations of the Study

The sample of study areas is relatively small and three of the areas have similar characteristics regarding slope angle, lithology, and failure mechanism. Because of this, the applicability of the methods to rock slopes with other characteristics is somewhat less confident than for slopes with similar traits as the study areas. There were no traditional measurements collected on rock outcrops and there was no terrestrial LiDAR survey performed during the fieldwork. Because of this there were no quantitative data to compare the digitally mapped discontinuity sets with and the validation was solely based on visual inspections. Consequently, the confidence in the resulting values is partly restricted. Further, the comparison between LiDAR and drone-derived SfM photogrammetry is limited to discussing general aspects of LiDAR or results obtained in previous research.

The image datasets were collected with manual flight, as opposed to automated flight according to a predefined flight plan. When surveying such large slopes, it can be challenging to ensure sufficient image coverage and optimal image network geometry. Adverse effects on these parameters can cause a lower accuracy in the resulting model. Because automated flight was not tested, the differences between the approached cannot be evaluated. Some smaller parts of the study areas Valle and Straumklumpen are missing image coverage as a consequence of using manual flight, but the areas are too small to affect the application of the models.

A limitation of the C2C comparison used in the validation is that it only generates absolute values. Use of a method that generates signed values (e.g. M3C2 in CloudCompare) could have enabled a more accurate assessment of error magnitudes and distributions. Nonetheless, the conclusion that C2C is a robust and comprehensive method for validating models used for digital mapping remains. Another limitation of the study is the that the obtained parameters were not used to assess the rockfall hazard and therefore the performance in hazard assessment cannot be directly evaluated.

7 Conclusions

This study aimed to test if drone-derived SfM photogrammetry and digital mapping could be applied to facilitate, streamline, and improve the determination of parameters that are relevant for rockfall hazard assessment. By applying these methods to five selected study areas and testing out different alternatives for data collection, a functional survey design was established that balances the need for producing accurate datasets against limitations in resources and time consumption. Issues that arose during data collection allowed insights to be gained regarding limitations of the GNSS equipment. The alternative solution that was implemented utilizes available orthophotos and digital elevation models (DEMs) for extracting ground control points (GCPs). This method of obtaining GCPs was found to be a viable complement to GNSS field surveys, thereby also increasing the usability of drone-derived SfM photogrammetry. An average survey range (i.e. camera-target distance) of 40-70 m corresponds to ground sampling distances (i.e. image resolution) of 1.4-2.2 cm/pixel, which proved to be sufficient for generating 3D models that meets the resolution requirements of the digital mapping tools.

This study performed thorough testing of different tools and filters in the Agisoft Metashape software to evaluate their effects and find an optimized workflow for photogrammetric reconstruction of large (> 100 m height) and natural rock slopes. The proposed workflow is intended to help users achieve accurate, precise, and representative results, without needing in-depth knowledge and technical expertise. Model accuracy was improved by up to 80 % when applying a workflow that was tailored to the specific dataset, compared to using default settings and the simple workflow suggested in the software manual. A comprehensive validation was performed to ensure sufficient model quality. This thesis found the C2C comparison in CloudCompare to be a robust method for validating model accuracy and assessing systematic errors, which can greatly increase the confidence in generated models. Validation confirmed that the generated models were of sufficient quality, with the exception of some areas in the model representing the largest study area. The thesis found a relationship between high georeferencing accuracy and high GCP density (i.e. the number of GCPs in relation to the model area).

Different tools for digital mapping of rock masses were tested on the validated models and evaluated. It was observed that semi-automated extraction of discontinuity surfaces is biased towards slope parallel orientations, with poorer sampling of obliquely oriented surfaces. Biased sampling when using semi-automated detection of surfaces has also been described by Menegoni et al. (2019). The mix of semi-automated and manual mapping that was applied to mitigate the adverse effects of the biased sampling appear to be effective. This study applied qualitative visual assessments of mapped and characterized discontinuities to validate the results, which appear to be reliable and representative for the study areas, with minor exceptions. This study found that the best results were obtained when the settings were tuned to fit each dataset.

Kinematic analyses were performed for the study areas by using the digitally mapped datasets and the failure mode indicated by the result generally corresponded with observations. For the one study areas there were a discrepancy between the failure mode suggested by the kinematic analysis and the observed failure mode. Because the suggested mitigation approach had only been implemented to a smaller degree for this study area, it was found that the discrepancy might be caused by the biased sampling associated with the semi-automated mapping tool.

This thesis has established a general workflow targeted towards large, natural rock slopes and which includes ranges for the settings that should be tuned to fit the specific dataset. The workflow has been shown to be functional, efficient, and capable of generating reliable data that accurately represents the study areas. As such, the suggested workflow can be applied by geoscientists to determine the relevant parameters for rockfall hazard assessments. Suggestions for future research are to test different options for image collection with automated flight, apply the workflow to other types of rock slopes, and to use the determined parameter values in hazard assessment.

References

Abellan, A., Derron, M. H., & Jaboyedoff, M. (2016). “Use of 3D point clouds in geohazards” special issue: current challenges and future trends. *Remote Sensing*, 8(2), 130. https://doi.org/10.3390/rs8020130

Agisoft. (2021a). *Agisoft Metashape User Manual: Professional Edition, Version 1.7*. https://www.agisoft.com/pdf/metashape-pro_1_7_en.pdf

Agisoft. (2021b). *Agisoft Metashape Professional* (version 1.7.1) [Computer software]. https://www.agisoft.com/downloads/installer/

Agisoft. (2021c). *Agisoft forum*. https://www.agisoft.com/forum/index.php

Allen, S. K., Gruber, S., & Owens, I. F. (2009). Exploring steep bedrock permafrost and its relationship with recent slope failures in the Southern Alps of New Zealand. *Permafrost and Periglacial Processes*, 20(4), 345-356. DOI: 10.1002/ppp.658

ALTUS Positioning Systems. (2015). *ALTUS APS-3 User Manual* (Revision 3.0.0). https://www.manualslib.com/manual/1415240/Altus-Aps-3.html

Anderson, K., Westoby, M. J., & James, M. R. (2019). Low-budget topographic surveying comes of age: Structure from motion photogrammetry in geography and the geosciences. *Progress in Physical Geography: Earth and Environment*, 43(2), 163–173. https://doi.org/10.1177/0309133319837454

Barton, N. (1982). Modelling rock joint behavior from in situ block tests: implications for nuclear waste repository design (Vol. 308). Office of Nuclear Waste Isolation. Columbus, OH, ONWI-308. 96pp.

Barton, N. & Bandis, S. (1990). Review of predictive capabilities of JRC-JCS model in engineering practice. International Symposium on Rock Joints. Loen, Norway. pp. 603–610.

Barton, N., & Choubey, V. (1977). The shear strength of rock joints in theory and practice. Rock mechanics, 10(1), 1-54. https://doi.org/10.1007/BF01261801

Braathen, A., Blikra, L. H., Berg, S. S., & Karlsen, F. (2004). Rock-slope failures in Norway; type, geometry, deformation mechanisms and stability. *Norwegian Journal of Geology/Norsk Geologisk Forening*, 84(1). https://foreninger.uio.no/ngf/ngt/pdfs/NJG_84_67-88.pdf

CloudCompare. (2021a). *CloudCompare* (v2.11.3 – Anoia). [Computer software]. http://www.cloudcompare.org/

CloudCompare. (2021b). *Cloud-to-Cloud Distance*. https://www.cloudcompare.org/doc/wiki/index.php?title=Cloud-to-Cloud_Distance

Collins, B. D., & Stock, G. M. (2016). Rockfall triggering by cyclic thermal stressing of exfoliation fractures. *Nature Geoscience*, 9(5), 395-400. DOI: 10.1038/NGEO2686

Cruden, D. M. & Varnes, D. J. (1996). Landslide types and processes. *Landslides: investigation and mitigation, Transportation Research Board special report*, 247: 36-75. https://onlinepubs.trb.org/Onlinepubs/sr/sr247/sr247-003.pdf

Devoli, G., Eikenæs, O., Taurisano, A., Hermanns, R., Fischer, L., Oppikofer, T. & Bunkholt, H. (2011). *Plan for skredfarekartlegging: Delrapport steinsprang, steinskred og fjellskred*. NVE, 15/2011. http://publikasjoner.nve.no/rapport/2011/rapport2011_15.pdf

Dietze, M., Turowski, J. M., Cook, K. L., & Hovius, N. (2017). Spatiotemporal patterns, triggers and anatomies of seismically detected rockfalls. *Earth Surface Dynamics*, 5(4), 757-779. https://doi.org/10.5194/esurf-5-757-2017

DJI. (2017, December 19). *Mavic Pro User Manual V2.0*. https://dl.djicdn.com/downloads/mavic/Mavic_Pro_User_Manual_v2.0_en.pdf

DJI. (2020). *DJI GO 4* (version 4.0) [Mobile app]. App Store. https://apps.apple.com/us/app/dji-go-4/id1170452592

Fischer, L., Purves, R. S., Huggel, C., Noetzli, J., & Haeberli, W. (2012). On the influence of topographic, geological and cryospheric factors on rock avalanches and rockfalls in high-mountain areas. *Natural Hazards and Earth System Sciences*, 12(1), 241-254. doi:10.5194/nhess-12-241-2012

Dorren, L. K. A. (2003). A review of rockfall mechanics and modelling approaches. *Progress in Physical Geography*: *Earth and Environment*. 27(1), 69-87. https://doi.org/10.1191/0309133303pp359ra

Finans Norge. (September 30, 2021). Naturskadestatistikk (NASK). https://www.finansnorge.no/statistikk/skadeforsikring/naturskadestatistikk-nask/

Garmin. (2007). *GPSmap 60CSx Owner's Manual*. Garmin International Inc. https://static.garmincdn.com/pumac/GPSMAP60CSx_OwnersManual.pdf

Geovekst. (2018). *Sørfold 2018* [Dataset]. Norgeibilder. https://www.norgeibilder.no/

Geovekst. (2019). *Agder 2019* [Dataset]. Norgeibilder. https://www.norgeibilder.no/

Gomez, C., & Purdie, H. (2016). UAV-based photogrammetry and geocomputing for hazards and disaster risk monitoring–a review. *Geoenvironmental Disasters*, 3(1), 1-11. https://doi.org/10.1186/s40677-016-0060-y

Goodman, R. E. (1989). *Introduction to rock mechanics* (Vol. 2). New York: Wiley.

Goodman, R. E., & Bray, J. (1976). Toppling of rock slopes. *In Proc. Speciality Conference on Rock Engineering for Foundation and Slopes*, Boulder, Colorado. ASCE.

Greenwood, W. (2018). *UAV-enabled surface and subsurface characterization for post-earthquake geotechnical reconnaissance* [Doctoral dissertation, University of Michigan]. https://deepblue.lib.umich.edu/handle/2027.42/145793

Guerin, A., Stock, G. M., Radue, M. J., Jaboyedoff, M., Collins, B. D., Matasci, B., ... & Derron, M. H. (2020). Quantifying 40 years of rockfall activity in Yosemite Valley with historical Structure-from-Motion photogrammetry and terrestrial laser scanning. *Geomorphology*, 356, 107069. https://doi.org/10.1016/j.geomorph.2020.107069

Highland, L. M., & Bobrowsky, P. (2008). *The landslide handbook - a guide to understanding landslides.* Reston, Virginia. US Geological Survey Circular 1325, 129 p. https://pubs.usgs.gov/circ/1325/

Hilger, P. (2019). *Rock-slope failures in Norway-temporal development and climatic conditioning* (Doctoral dissertation). Oslo: University of Oslo. http://urn.nb.no/URN:NBN:no-73926

Hoek, E., & Bray, J. D. (1981). *Rock slope engineering*. CRC Press.

Hoek, E. (2007). *Practical rock engineering*. Rocscience. https://www.rocscience.com/learning/hoeks-corner/

Hoek, E. (2009, November 9-11). *Fundamentals in slope design*. Keynote address at Slope Stability 2009, Santiago, Chile.

Hudson, J. A., & Harrison, J. P. (2000). *Engineering rock mechanics: an introduction to the principles.* Elsevier.

Hungr, O., Leroueil, S., & Picarelli, L. (2014). The Varnes classification of landslide types, an update. *Landslides*, 11(2), 167-194. DOI 10.1007/s10346-013-0436-y

Høst, J. (2006). *Store fjellskred i Norge*. Utredning for Landbruks- og matdepartementet på vegne av 6 departementer. NGU-rapport, Norges Geologiske undersøkelse. Trondheim, Norge. pp. 87. https://www.ngu.no/upload/Publikasjoner/Rapporter/2006/Store-fjellskred-i-Norge%282%29.pdf

ISPRS. (2021, May 30). *Statutes*. ISPRS. https://www.isprs.org/documents/statutes19.aspx

Jaboyedoff, M., Oppikofer, T., Abellán, A., Derron, M. H., Loye, A., Metzger, R., & Pedrazzini, A. (2012). *Use of LIDAR in landslide investigations: a review*. Natural hazards, 61(1), 5-28. DOI 10.1007/s11069-010-9634-2

James, M. R., & Robson, S. (2012). Straightforward reconstruction of 3D surfaces and topography with a camera: Accuracy and geoscience application. *Journal of Geophysical Research: Earth Surface*, 117(F3). https://doi.org/10.1029/2011JF002289

James, M. R., & Robson, S. (2014). Mitigating systematic error in topographic models derived from UAV and ground-based image networks. *Earth Surface Processes and Landforms*, 39(10), 1413-1420. https://doi.org/10.1002/esp.3609

James, M. R., Robson, S., d'Oleire-Oltmanns, S., & Niethammer, U. (2017). Optimising UAV topographic surveys processed with structure-from-motion: Ground control quality, quantity and bundle adjustment. *Geomorphology*, 280, 51-66. https://doi.org/10.1016/j.geomorph.2016.11.021

JCGM. (2012). *JCGM 200:2012 International vocabulary of metrology – Basic and general concepts and associated terms (VIM).* Bureau International des Poids et Mesures. https://www.bipm.org/en/publications/guides/

Kartverket. (2014). *Sogndal_Aurland_Lærdal 2pkt 2014* [Dataset]. Høydedata. https://hoydedata.no/LaserInnsyn/

Kartverket. (2015). *Geodatakvalitet, versjon 1.0 – 2015*.
Standarder geografisk informasjon.
https://www.kartverket.no/globalassets/geodataarbeid/standardisering/standarder/standarder-geografisk-informasjon/geodatakvalitet-1.0-standarder-geografisk-informasjon.pdf

Kartverket. (2017a). *NDH Fauske 2 pkt 2017* [Dataset]. Høydedata. https://hoydedata.no/LaserInnsyn/

Kartverket. (2017b). *NDH Valle 5 pkt 2017* [Dataset]. Høydedata. https://hoydedata.no/LaserInnsyn/

Kartverket. (2018). *NDH Nore og Uvdal 5pkt 2018* [Dataset]. Høydedata. https://hoydedata.no/LaserInnsyn/

Kartverket. (2019, January 1). *Produktspesifikasjon FKB-Laser* (v3.0). http://sosi.geonorge.no/Produktspesifikasjoner/Produktspesifikasjon_FKB-Laser_3.0.pdf

Kartverket. (2020, September 24). *Guide to CPOS*. Retrieved March 4, 2021 from https://www.kartverket.no/en/on-land/posisjon/guide-to-cpos

Kjerstad, N. (2020, June 18). DOP – satellittgeometri. *Store norske leksikon.* Retrieved March 15, 2021 from https://snl.no/DOP_-_satellittgeometri

Kartverket. (2021). *Topografisk norgeskart 4* [Web Map Server]. Geonorge. https://openwms.statkart.no/skwms1/wms.topo4?service=wms&request=getcapabilities

Kraus, K. (2007). *Photogrammetry: geometry from images and laser scans*. de Gruyter. https://doi.org/10.1515/9783110892871.47

Langley, R. B. (1999). Dilution of Precision. *GPS World,* 10(5), 52-59. http://131.202.94.44/papers.pdf/gpsworld.may99.pdf

Li, C., Zhang, N., & Ruiz, J. (2019). Measurement of the basic friction angle of planar rock discontinuities with three rock cores. *Bulletin of Engineering Geology and the Environment*, 78(2), 847-856. DOI 10.1007/s10064-017-1045-0

Linder, W. (2016). *Digital Photogrammetry - A Practical Course*. Springer. DOI 10.1007/978-3-662-50463-5

Luftfartstilsynet. (2020, April 10). *Secure distances and maximum height.* https://luftfartstilsynet.no/en/drones/commercial-use-of-drones/about-dronesrpas/secure-distances/

Luftfartstilsynet. (2021a, March 31). *Definitions for unmanned air traffic*. https://luftfartstilsynet.no/en/drones/commercial-use-of-drones/about-dronesrpas/definitions-for-unmanned-air-traffic/

Luftfartstilsynet. (2021b, March 7). *About CAA Norway*. https://luftfartstilsynet.no/en/about-us/about-caa-norway/

Luftfartstilsynet. (2021c, March 7). *Open category*. https://luftfartstilsynet.no/en/drones/new-eu-regulations/open-category/

Luhmann, T., Robson, S., Kyle, S., & Boehm, J. (2019). *Close-Range Photogrammetry and 3D Imaging* (3rd edition). Walter de Gruyter GmbH & Co KG.

Magnin, F, Etzelmüller, B, Westermann, S, Isaksen, K, Hilger, P, og Hermanns, R. L. (2019). Permafrost distribution in steep rock slopes in Norway: measurements, statistical modelling and implications for geomorphological processes. *Earth Surf. Dynam*., 7 Götting: Copernicus Publications. https://doi.org/10.5194/esurf-7-1019-2019

Maptek. (2021a). *Maptek PointStudio* (version 2021) [Computer software].

Maptek. (2021b). *Maptek PointStudio*. Retrieved September 30, 2021 from https://www.maptek.com/products/pointstudio/index.html

Marzolff, I., Ries, J., Aber, S. E. W., & Aber, J. S. (2019). *Small-format aerial photography: principles, techniques and geoscience applications*. https://doi.org/10.1016/C2016-0-03506-4

Menegoni, N., Giordan, D., Perotti, C., & Tannant, D. D. (2019). Detection and geometric characterization of rock mass discontinuities using a 3D high-resolution digital outcrop model generated from RPAS imagery–Ormea rock slope, Italy. *Engineering geology*, 252, 145-163. https://doi.org/10.1016/j.enggeo.2019.02.028

Menegoni, N., Giordan, D., & Perotti, C. (2020). Reliability and uncertainties of the analysis of an unstable rock slope performed on RPAS digital outcrop models: The case of the gallivaggio landslide (Western Alps, Italy). *Remote Sensing*, 12(10), 1635. https://doi.org/10.3390/rs12101635

Morken, Elise. (2021). *Performance of Three Rockfall Models Tested at Historic Rockfall Sites in Western Norway*. [Master's thesis, University of Oslo]. DUO. https://www.duo.uio.no/

Naturmangfoldloven. (2020). *Lov om forvaltning av naturens mangfold* (LOV-2020-06-19-88). https://lovdata.no/dokument/NL/lov/2009-06-19-100/KAPITTEL_3#%C2%A715

NGI. (2017). *Steinsprang I Valle, Setesdal*. Dokumentnr. 20170666-01-R.

NGU. (2021). *Bergrunn - Nasjonal berggrunnsdatabase.* http://geo.ngu.no/kart/berggrunn_mobil/

Norwegian Centre for Space Weather (NOSWE). (2021, February 1). *Quaterly report on past space weather, Q4 2020.* UIT. Retrieved March 4, 2021 from https://site.uit.no/spaceweather/files/2021/02/Quarterly-report-on-past-space-weather-2020-Q4.pdf

NVE. (2020). *Veileder for utredning av sikkerhet mot skred i bratt terreng*. Retrieved August 21, 2021 from https://www.nve.no/veileder-skredfareutredning-bratt-terreng.

NVE. (October 20, 2021). *NVE temakart Skredhendingar*. https://temakart.nve.no/link/?link=skredhendelser

Obanawa, H., & Hayakawa, Y. S. (2018). Variations in volumetric erosion rates of bedrock cliffs on a small inaccessible coastal island determined using measurements by an unmanned aerial vehicle with structure-from-motion and terrestrial laser scanning. *Progress in Earth and Planetary Science*, 5(1), 1-10. https://progearthplanetsci.springeropen.com/articles/10.1186/s40645-018-0191-8

Omløpsfoto. (2015). *Nordland Nord 2015* [Dataset]. Norgeibilder. https://www.norgeibilder.no/

Poliarnyi, N. (2021, April 20). *add_altitude_to_reference.py* (Release 1.7) [Computer code]. https://github.com/agisoft-llc/metashape-scripts/blob/master/src/add_altitude_to_reference.py

Ravanel, L., Magnin, F., & Deline, P. (2017). Impacts of the 2003 and 2015 summer heatwaves on permafrost-affected rock-walls in the Mont Blanc massif. *Science of the Total Environment*, 609, 132-143. https://doi.org/10.1016/j.scitotenv.2017.07.055

Rocscience. (2021). *Dips* (version 8.005) [computer software]. https://www.rocscience.com/software/dips

Rodriguez, J., Macciotta, R., Hendry, M. T., Roustaei, M., Gräpel, C., & Skirrow, R. (2020). UAVs for monitoring, investigation, and mitigation design of a rock slope with multiple failure mechanisms—A case study. *Landslides*, 17, 2027-2040. DOI 10.1007/s10346-020-01416-4

Rød, J. K. (2020, March 23). Høyde. *Store norske leksikon*. Retrieved March 15, 2021 from https://snl.no/h%C3%B8yde

Smith, M. W., Carrivick, J. L., & Quincey, D. J. (2016). Structure from motion photogrammetry in physical geography. *Progress in Physical Geography*, 40(2), 247-275. https://doi.org/10.1177%2F0309133315615805

Space Weather Prediction Centre (SWPC). (2021). Space weather and GPS systems. NOAA. Retrieved March 5, 2021 from https://www.swpc.noaa.gov/impacts/space-weather-and-gps-systems

Stead, D., Donati, D., & Brideau, M-A. (2021). *Rock Slides and Topples*. Reference Module in Earth Systems and Environmental Sciences. DOI: 10.1016/B978-0-12-818234-5.00060-2

Stead, D., & Wolter, A. (2015). A critical review of rock slope failure mechanisms: the importance of structural geology. *Journal of Structural Geology*, 74, 1-23. https://doi.org/10.1016/j.jsg.2015.02.002

Varnes, D. J. (1978). Slope movement types and processes. *Special report*, 176, 11-33. http://onlinepubs.trb.org/Onlinepubs/sr/sr176/176-002.pdf

Vasuki, Y., Holden, E. J., Kovesi, P., & Micklethwaite, S. (2014). Semi-automatic mapping of geological Structures using UAV-based photogrammetric data: An image analysis approach. *Computers & Geosciences*, 69, 22-32. https://doi.org/10.1016/j.cageo.2014.04.012

Volkwein, A., Schellenberg, K., Labiouse, V., Agliardi, F., Berger, F., Bourrier, F., Dorren, L. K. A., Gerber, W., & Jaboyedoff, M. (2011). Rockfall characterisation and structural protection–a review. *Natural Hazards and Earth System Sciences*, 11(9), 2617-2651. doi:10.5194/nhess-11-2617-2011

Warrick, J. A., Ritchie, A. C., Adelman, G., Adelman, K., & Limber, P. W. (2017). New techniques to measure cliff change from historical oblique aerial photographs and structure-from-motion photogrammetry. *Journal of Coastal Research*, 33(1), 39-55. https://doi.org/10.2112/JCOASTRES-D-16-00095.1

Westoby, M.J, Brasington, J, Glasser, N.F, Hambrey, M.J, & Reynolds, J.M. (2012). 'Structure-from-Motion' photogrammetry: A low-cost, effective tool for geoscience applications. *Geomorphology* (Amsterdam, Netherlands), 179, 300–314. https://doi.org/10.1016/j.geomorph.2012.08.021

Wyllie, D. C., & Mah, C. (2004). *Rock slope engineering: Civil and mining* (4th ed.). CRC Press.

Wyllie, D. C. (2014). *Rock fall engineering* (1st ed.). CRC Press. https://doi.org/10.1201/b17470

Zekkos, D., Greenwood, W., Lynch, J., Manousakis, J., Athanasopoulos-Zekkos, A., Clark, M., & Saroglou, C. (2018). Lessons learned from the application of UAV-enabled structure-from-motion photogrammetry in geotechnical engineering. *International Journal of Geoengineering Case Histories*, 4(4), 254-274. doi:10.4417/IJGCH-04-04-03

Appendices

Appendix A:
Workflow in Agisoft Metashape

1. **Create a Project**
2. **Load Photos**
    - Should have unique names, no duplicates.
    - File format: dng
3. Set Coordinate System
    - Change coordinate system for the project/output (reference pane - reference settings)
    - Convert coordinate system for the photos, which are called “cameras” in Metashape (reference pane - convert button on toolbar)
    - Coordinate system: ETRS89/UTM zone 32 + NN2000
4. Change positioning accuracy of camera
    - In “Reference settings” the default value is set to 10 m.
    - GNSS onboard RPAs commonly has better accuracy north/east and lower altitude accuracy. The camera accuracy was changed to better reflect this.
    - Settings:
        - Camera accuracy: 10/30
5. **Estimate Image Quality** (Photos pane – right click for context menu)
    - Disable images with quality < 0.5
6. **Align Photos**
    - Settings:
        - Accuracy: High
        - Generic preselection: Yes
        - Reference preselection: Yes, set as “Source”
        - Key point limit: 70 000
        - Tie point limit: 0
        - Adaptive camera model fitting: Yes

    - Realign or disable images that were not aligned.

7. Edit Sparse Cloud
    - Remove points with high reprojection error (Model drop-down menu - Gradual selection)
        - Settings:
            - Criterion: Reprojection error
            - Size: 0.4 - 0.5 (Be careful not to select too many points)
        - Delete selection after finalizing it.
    - Remove points with high reconstruction uncertainty (Model drop-down menu - Gradual selection)
        - Settings:

        - Criterion: Reconstruction uncertainty
        - Size: 10 - 25 (Be careful not to delete too many points)
    - Delete selection after finalizing it.
- Remove points with low projection accuracy (Model drop-down menu - Gradual selection)
    - Settings:
        - Criterion: Projection accuracy
        - Size: 10 (Be careful not to delete too many points)
    - Delete selection after finalizing it.
- Manually edit sparse cloud and remove unwanted points using the selection tool and delete button

8. **Import GCP-Coordinates**
    - File format: txt
    - Important to include accuracies, since they can differ dramatically from the default value of 0.005 m that is otherwise used.
    - Settings:
        - Coordinate system: ETRS89/UTM zone 32 + NN2000
        - Delimiter: space
        - Start import at row 2
        - Columns: Label 1, Easting 3, Northing 2, Altitude 4.
        - Accuracy: Easting 6, Northing 5, Altitude 7
        - No rotation
        - Pop-up window: Create markers for all
9. **Place Markers**
    - Move the automatically placed markers in the photos or right click, select "place marker" and scroll down for the right one.
    - After having placed a marker in a couple photos, it's possible to right click on the marker and select "Filter photos by marker".
    - It is also possible to turn on the cameras in the model window and use the select tool to show the cameras surrounding a marker.
    - Place markers in all photos where the cross markers are visible.
    - Click update in the reference pane.
    - Leave boxes checked for markers you want to use as "control points" (used to reference the model) and uncheck boxes for markers that should be used as "check points" (used for validation).
10. Adjust the Volume Bounding Box
    - The entire cloud/model should fit within the box.
    - Use the "Resize Region"," Move Region" and "Rotate Region" toolbar buttons.
11. **Optimize Camera Alignment** (magic wand button in reference pane)
    - Make sure both camera and control point boxes are checked. (For very large datasets you might try optimizing cameras and control points separately, with cameras first.)
    - Choose all parameters except k4 under general.
    - Adaptive camera model fitting: No
    - Estimate tie point covariance: Yes

12. Iterations to improve accuracy
    - If needed, repeat steps “remove points with high reprojection error” and “optimize camera alignment” 1 - 2 times to get lower georeferencing errors.

13. Build Dense Cloud
    - Settings:
        - Quality: High
        - Depth filtering: Mild
        - Calculate point colours: Yes
        - Calculate point confidence: Yes

14. Edit Dense Cloud
    - Filter by confidence (Tools drop-down menu – Dense Cloud)
        - Turn on dense cloud confidence in the model view.
        - Settings:
            - Min: ca 5
            - Max: 255 (default)
        - When satisfied with the selection, choose invert selection in the Edit drop-down menu. Press delete.
    - Manually edit dense point cloud and remove unwanted points using the selection tool and delete button.

15. Build Mesh
    - Settings:
        - Source data: Depth maps
        - Surface type: Arbitrary (3D)
        - Quality: High
        - Face count: High
        - Interpolation: Enabled (default)
        - Depth filtering: Mild
        - Calculate vertex colors: Yes
        - Reuse depth maps: Yes

16. Edit Mesh
    - Remove isolated mesh fragments (Model drop-down menu - Gradual Selection)
        - Settings:
            - Criterion: Connected component size
            - Size: 5-20 % (size of selected fragments, 100 % being the largest fragment)
        - Delete selection after finalizing it.
    - Manually edit mesh and remove unwanted faces using the selection tool and delete button – if needed.
    - Decimate model – if needed.
        - Especially useful for very large datasets.

17. Turn on sparse cloud in the model view

- Less demanding to display sparse cloud than mesh. Helpful when running demanding processes, such as build texture and build tiled model.

18. Build Texture

- Settings:
    - Texture type: Diffuse map
    - Source data: Images
    - Mapping mode: Generic
    - Blending mode: Mosaic (default)
    - Texture size/count: 16 384 * 1
    - Enable hole filling: Yes
    - Enable ghosting filter: Yes

19. Build Tiled Model

- Settings:
    - Source data: Mesh
    - Pixel size: x (in meters, automatically generated value but possible to change)
    - Tile size: 256 (in pixels, default)
    - Face count: High
    - Transfer model texture: Yes (if one has previously been generated)
    - Enable ghosting filter: Yes (if no previous texture is available)

20. Build DEM

- Settings:
    - Projection type: Geographic
    - ETRS89/UTM zone 32N +NN2000
    - Source data: Dense cloud
    - Interpolation: Enabled (default)
    - Resolution: x (in meters, automatically generated value, not possible to change)
    - Total size: x (in pixels)

21. Transform DEM (Tools drop-down menu - DEM)

- Used to create DEMs with lower resolutions.
- Type in the desired resolution value.

22. Build Orthomosaic

- Settings:
    - Projection type: Geographic
    - ETRS89/UTM zone 32N + NN2000
    - Surface DEM
    - Blending mode: Mosaic (default)
    - Enable hole filling: Yes
    - Pixel size: x (in meters, automatically generated value, possible to change)

23. Export (File drop-down menu - Export)

- Dense Cloud
    - Settings:
        - File format: las or laz
        - Coordinate system: ETRS89/UTM zone 32N

        - Save point colors: Yes
        - Save point confidence: Yes
        - Save point normales: Yes
        - Save point classes: Yes (if some were created)
        - Remember to uncheck “clip to boundary shapes”
- Mesh & Texture
    - Settings:
        - File format: obj
        - Coordinate system: ETRS89/UTM zone 32N
        - Vertex colors: Yes
        - Vertex normals: Yes
        - Export texture: JPEG (for import to PointStudio)
        - Precision: x (Default value)
        - Use UDIM texture layout: Yes
        - Save alpha channel: Yes
        - Remember to uncheck “clip to boundary shapes”

24. Generate Report (File drop-down menu - Export)

- Useful for documenting the project.
- Produces plots and parameter values which may be useful in evaluating the quality of the reconstructions.

Appendix B:

Camera Locations and Image Overlaps

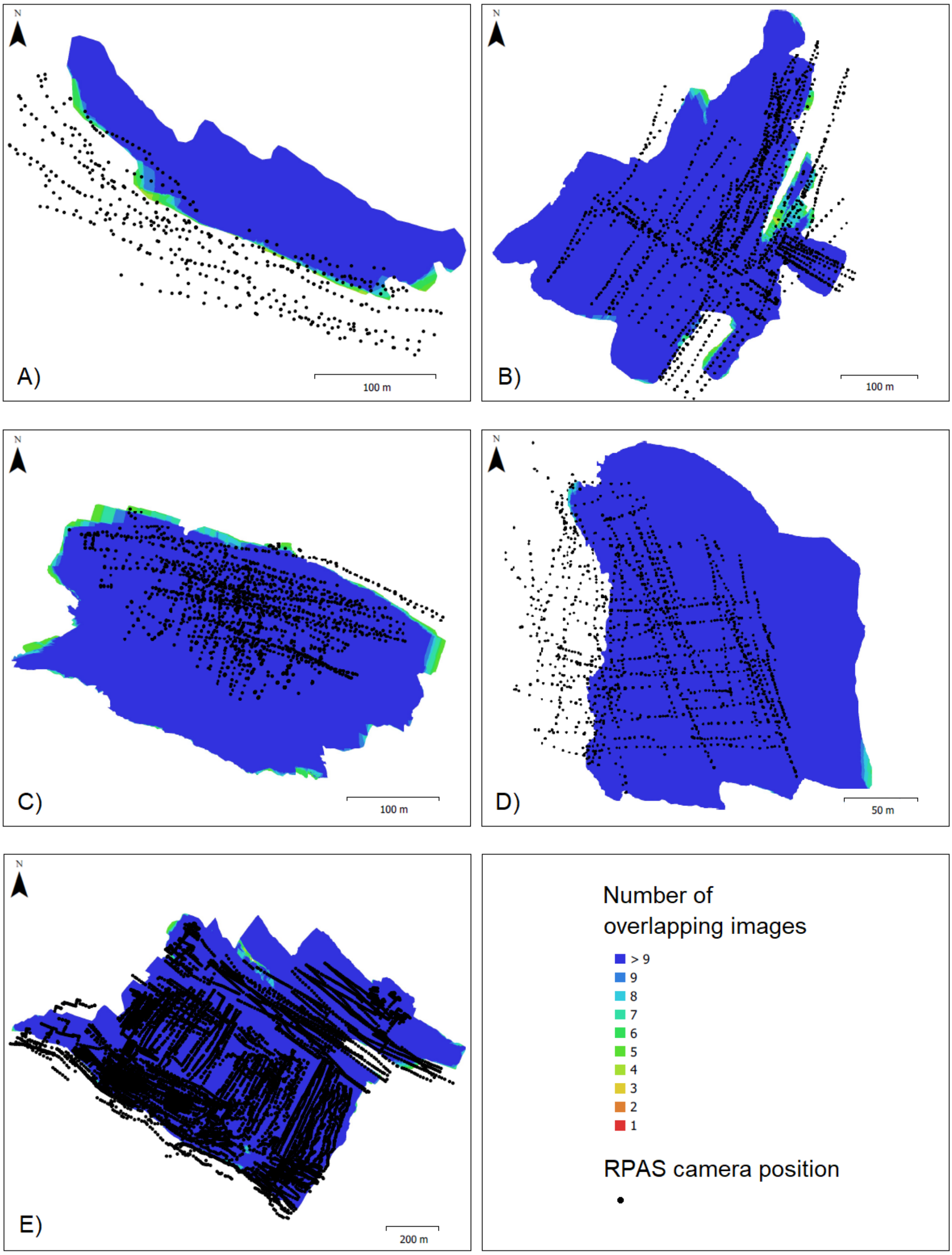

Figure I: RPAS camera positions and image overlaps from the surveys at each study area for A) Tunhovd, B) Valle, C) Lærdal, D) Ørnlia and E) Straumklumpen. In general the number of overlapping images exceeded 9.

Appendix C:

Camera Calibration

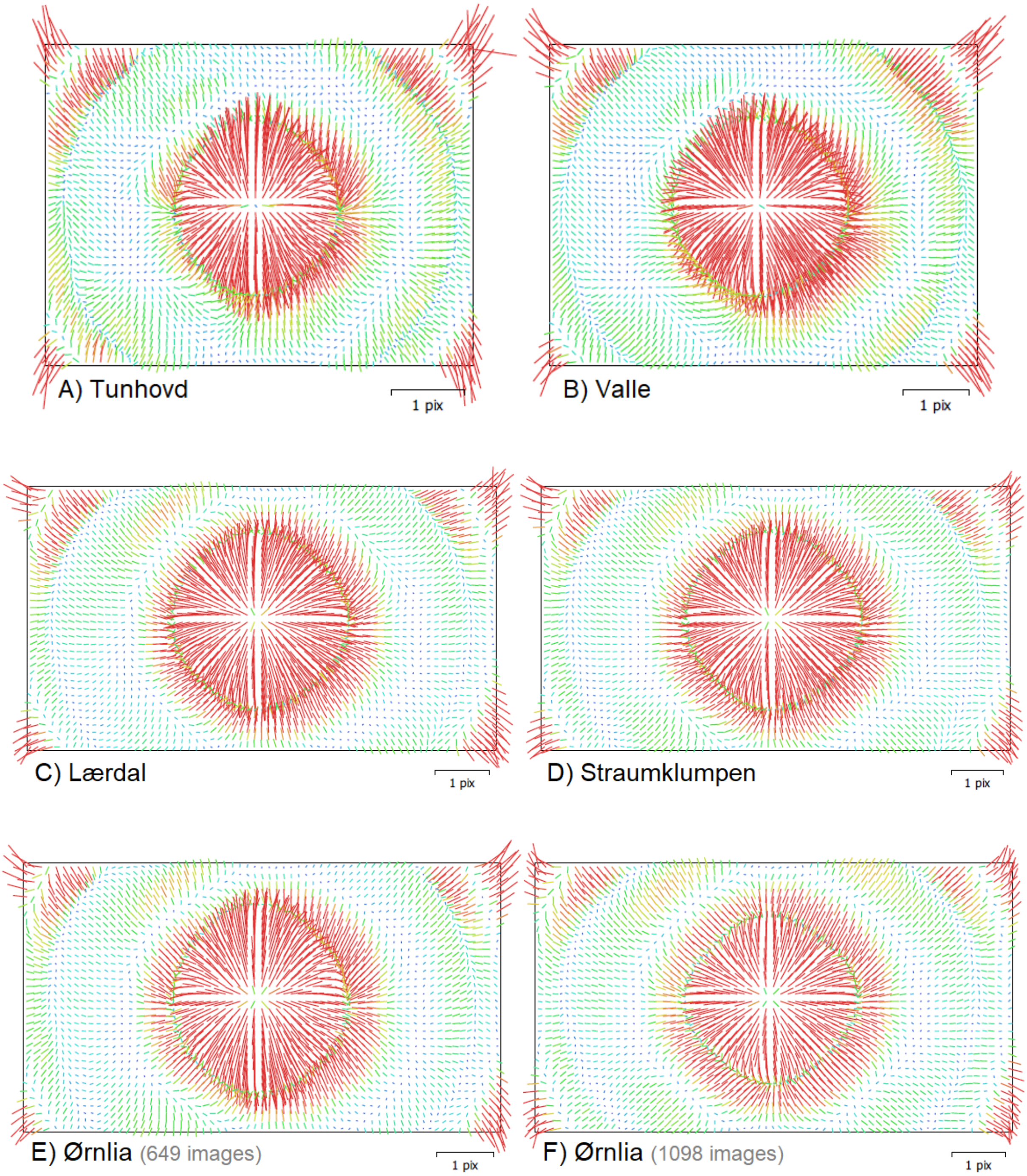

Figure II: Residual image distortion after camera self-calibration in Agisoft Metashape, for study areas A) Tunhovd, B) Valle, C) Lærdal, D) Straumklumpen, E) and F) Ørnlia. The residual image distortion is visualised as lines, which show the direction of the distortion. The distortion lines have been greatly enlarged compared to the image frame, for better visualization. The lines are colour-coded according distortion magnitude, with red representing the largest distortions. One pixel corresponds to 1.35-2.21 cm (on average) on the ground.

Appendix D:

GCP Locations and Error Estimates

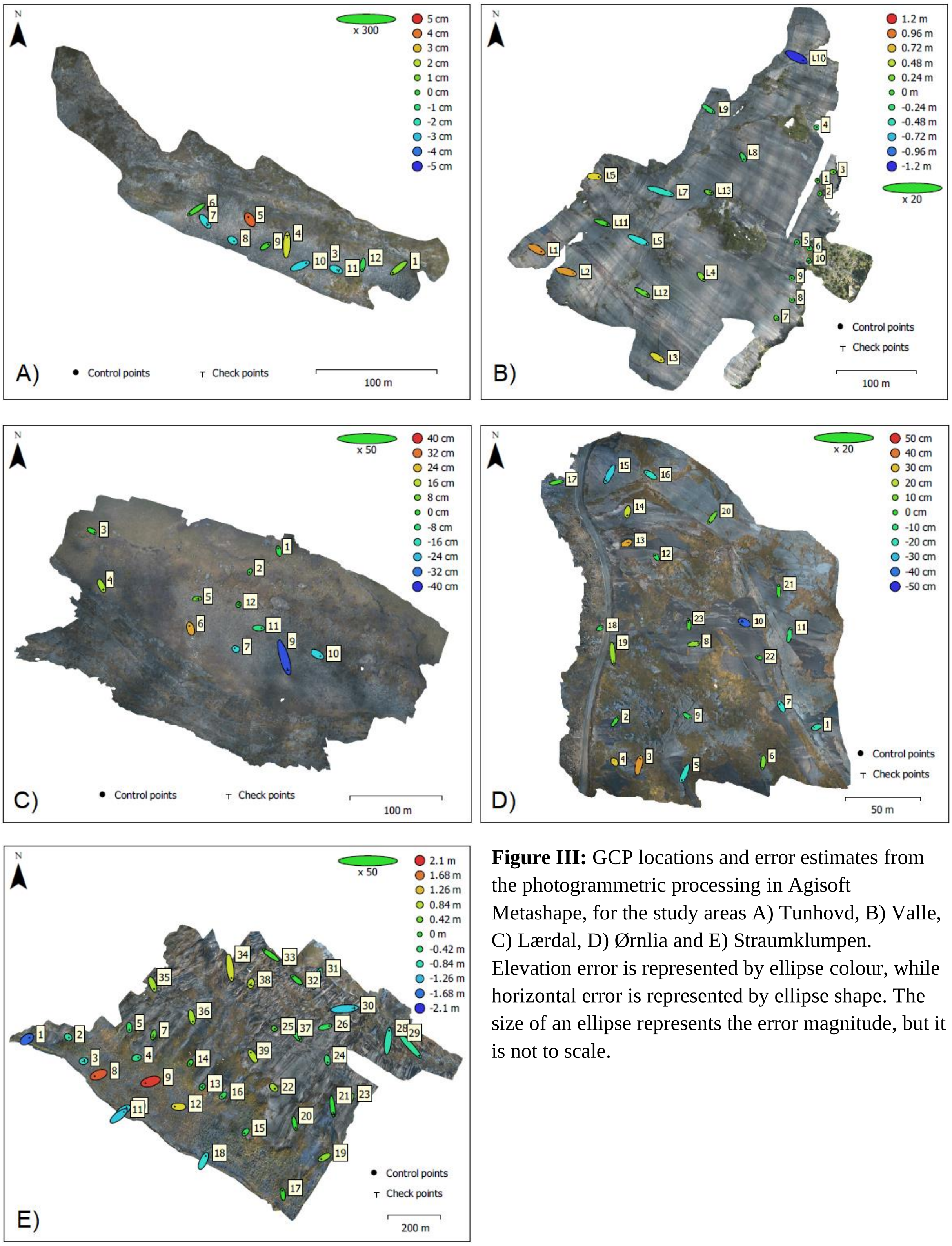

Figure III: GCP locations and error estimates from the photogrammetric processing in Agisoft Metashape, for the study areas A) Tunhovd, B) Valle, C) Lærdal, D) Ørnlia and E) Straumklumpen. Elevation error is represented by ellipse colour, while horizontal error is represented by ellipse shape. The size of an ellipse represents the error magnitude, but it is not to scale.